



Engineering Journal IJOER

Volume-11, Issue-9, September 2025

DOWNLOAD NOW

Preface

We would like to present, with great pleasure, the inaugural volume-11, Issue-9, September 2025, of a scholarly journal, *International Journal of Engineering Research & Science*. This journal is part of the AD Publications series *in the field of Engineering, Mathematics, Physics, Chemistry and science Research Development*, and is devoted to the gamut of Engineering and Science issues, from theoretical aspects to application-dependent studies and the validation of emerging technologies.

This journal was envisioned and founded to represent the growing needs of Engineering and Science as an emerging and increasingly vital field, now widely recognized as an integral part of scientific and technical investigations. Its mission is to become a voice of the Engineering and Science community, addressing researchers and practitioners in below areas:

Chemical Engineering	
Biomolecular Engineering	Materials Engineering
Molecular Engineering	Process Engineering
Corrosion Engineering	
Civil Engineering	
Environmental Engineering	Geotechnical Engineering
Structural Engineering	Mining Engineering
Transport Engineering	Water resources Engineering
Electrical Engineering	
Power System Engineering	Optical Engineering
Mechanical Engineering	
Acoustical Engineering	Manufacturing Engineering
Optomechanical Engineering	Thermal Engineering
Power plant Engineering	Energy Engineering
Sports Engineering	Vehicle Engineering
Software Engineering	
Computer-aided Engineering	Cryptographic Engineering
Teletraffic Engineering	Web Engineering
System Engineering	
Mathematics	
Arithmetic	Algebra
Number theory	Field theory and polynomials
Analysis	Combinatorics
Geometry and topology	Topology
Probability and Statistics	Computational Science
Physical Science	Operational Research
Physics	
Nuclear and particle physics	Atomic, molecular, and optical physics
Condensed matter physics	Astrophysics
Applied Physics	Modern physics
Philosophy	Core theories

Chemistry	
Analytical chemistry	Biochemistry
Inorganic chemistry	Materials chemistry
Neurochemistry	Nuclear chemistry
Organic chemistry	Physical chemistry
Other Engineering Areas	
Aerospace Engineering	Agricultural Engineering
Applied Engineering	Biomedical Engineering
Biological Engineering	Building services Engineering
Energy Engineering	Railway Engineering
Industrial Engineering	Mechatronics Engineering
Management Engineering	Military Engineering
Petroleum Engineering	Nuclear Engineering
Textile Engineering	Nano Engineering
Algorithm and Computational Complexity	Artificial Intelligence
Electronics & Communication Engineering	Image Processing
Information Retrieval	Low Power VLSI Design
Neural Networks	Plastic Engineering

Each article in this issue provides an example of a concrete industrial application or a case study of the presented methodology to amplify the impact of the contribution. We are very thankful to everybody within that community who supported the idea of creating a new Research with IJOER. We are certain that this issue will be followed by many others, reporting new developments in the Engineering and Science field. This issue would not have been possible without the great support of the Reviewer, Editorial Board members and also with our Advisory Board Members, and we would like to express our sincere thanks to all of them. We would also like to express our gratitude to the editorial staff of AD Publications, who supported us at every stage of the project. It is our hope that this fine collection of articles will be a valuable resource for *IJOER* readers and will stimulate further research into the vibrant area of Engineering and Science Research.



Mukesh Arora
(Chief Editor)

Board Members

Mr. Mukesh Arora (Editor-in-Chief)

BE (Electronics & Communication), M.Tech (Digital Communication), currently serving as Assistant Professor in the Department of ECE.

Prof. Dr. Fabricio Moraes de Almeida

Professor of Doctoral and Master of Regional Development and Environment - Federal University of Rondonia.

Dr. Parveen Sharma

Dr Parveen Sharma is working as an Assistant Professor in the School of Mechanical Engineering at Lovely Professional University, Phagwara, Punjab.

Prof. S. Balamurugan

Department of Information Technology, Kalaignar Karunanidhi Institute of Technology, Coimbatore, Tamilnadu, India.

Dr. Omar Abed Elkareem Abu Arqub

Department of Mathematics, Faculty of Science, Al Balqa Applied University, Salt Campus, Salt, Jordan, He received PhD and Msc. in Applied Mathematics, The University of Jordan, Jordan.

Dr. AKPOJARO Jackson

Associate Professor/HOD, Department of Mathematical and Physical Sciences, Samuel Adegboyega University, Ogwa, Edo State.

Dr. Ajoy Chakraborty

Ph.D.(IIT Kharagpur) working as Professor in the department of Electronics & Electrical Communication Engineering in IIT Kharagpur since 1977.

Dr. Ukar W. Soelistijo

Ph D, Mineral and Energy Resource Economics, West Virginia State University, USA, 1984, retired from the post of Senior Researcher, Mineral and Coal Technology R&D Center, Agency for Energy and Mineral Research, Ministry of Energy and Mineral Resources, Indonesia.

Dr. Samy Khalaf Allah Ibrahim

PhD of Irrigation &Hydraulics Engineering, 01/2012 under the title of: "Groundwater Management under Different Development Plans in Farafra Oasis, Western Desert, Egypt".

Dr. Ahmet ÇİFCİ

Ph.D. in Electrical Engineering, Currently Serving as Head of Department, Burdur Mehmet Akif Ersoy University, Faculty of Engineering and Architecture, Department of Electrical Engineering.

Dr. M. Varatha Vijayan

Annauniversity Rank Holder, Commissioned Officer Indian Navy, Ncc Navy Officer (Ex-Serviceman Navy), Best Researcher Awardee, Best Publication Awardee, Tamilnadu Best Innovation & Social Service Awardee From Lions Club.

Dr. Mohamed Abdel Fatah Ashabrawy Moustafa

PhD. in Computer Science - Faculty of Science - Suez Canal University University, 2010, Egypt.

Assistant Professor Computer Science, Prince Sattam bin AbdulAziz University ALkharj, KSA.

Prof.S.Balamurugan

Dr S. Balamurugan is the Head of Research and Development, Quants IS & CS, India. He has authored/co-authored 35 books, 200+ publications in various international journals and conferences and 6 patents to his credit. He was awarded with Three Post-Doctoral Degrees - Doctor of Science (D.Sc.) degree and Two Doctor of Letters (D.Litt) degrees for his significant contribution to research and development in Engineering.

Dr. Mahdi Hosseini

Dr. Mahdi did his Pre-University (12th) in Mathematical Science. Later he received his Bachelor of Engineering with Distinction in Civil Engineering and later he Received both M.Tech. and Ph.D. Degree in Structural Engineering with Grade "A" First Class with Distinction.

Dr. Anil Lamba

Practice Head – Cyber Security, EXL Services Inc., New Jersey USA.

Dr. Anil Lamba is a researcher, an innovator, and an influencer with proven success in spearheading Strategic Information Security Initiatives and Large-scale IT Infrastructure projects across industry verticals. He has helped bring about a profound shift in cybersecurity defense. Throughout his career, he has parlayed his extensive background in security and a deep knowledge to help organizations build and implement strategic cybersecurity solutions. His published researches and conference papers has led to many thought provoking examples for augmenting better security.

Dr. Ali İhsan KAYA

Currently working as Associate Professor in Mehmet Akif Ersoy University, Turkey.

Research Area: Civil Engineering - Building Material - Insulation Materials Applications, Chemistry - Physical Chemistry – Composites.

Dr. Parsa Heydarpour

Ph.D. in Structural Engineering from George Washington University (Jan 2018), GPA=4.00.

Dr. Heba Mahmoud Mohamed Afify

Ph.D degree of philosophy in Biomedical Engineering, Cairo University, Egypt worked as Assistant Professor at MTI University.

Dr. Kalpesh Sunil Kamble (Ph.D., P.Eng., M.Tech, B.E. (Mechanical))

A distinguished academic with a Ph.D. in Mechanical Engineering and 13 Years of extensive teaching and research experience. He is currently a Assistant professor at the SSPM's COE, Kankavli and contributes to several undergraduate and masters programs across Maharashtra, India.

Dr. Aurora Angela Pisano

Ph.D. in Civil Engineering, Currently Serving as Associate Professor of Solid and Structural Mechanics (scientific discipline area nationally denoted as ICAR/08—"Scienza delle Costruzioni"), University Mediterranea of Reggio Calabria, Italy.

Dr. Faizullah Mahar

Associate Professor in Department of Electrical Engineering, Balochistan University Engineering & Technology Khuzdar. He is PhD (Electronic Engineering) from IQRA University, Defense View, Karachi, Pakistan.

Prof. Viviane Barrozo da Silva

Graduated in Physics from the Federal University of Paraná (1997), graduated in Electrical Engineering from the Federal University of Rio Grande do Sul - UFRGS (2008), and master's degree in Physics from the Federal University of Rio Grande do Sul (2001).

Dr. S. Kannadhasan

Ph.D (Smart Antennas), M.E (Communication Systems), M.B.A (Human Resources).

Dr. Christo Ananth

Ph.D. Co-operative Networks, M.E. Applied Electronics, B.E Electronics & Communication Engineering Working as Associate Professor, Lecturer and Faculty Advisor/ Department of Electronics & Communication Engineering in Francis Xavier Engineering College, Tirunelveli.

Dr. S.R.Boselin Prabhu

Ph.D, Wireless Sensor Networks, M.E. Network Engineering, Excellent Professional Achievement Award Winner from Society of Professional Engineers Biography Included in Marquis Who's Who in the World (Academic Year 2015 and 2016). Currently Serving as Assistant Professor in the department of ECE in SVS College of Engineering, Coimbatore.

Dr. Balasubramanyam, N

Dr.Balasubramanyam, N working as Faculty in the Department of Mechanical Engineering at S.V.University College of Engineering Tirupati, Andhra Pradesh.

Dr. PAUL P MATHAI

Dr. Paul P Mathai received his Bachelor's degree in Computer Science and Engineering from University of Madras, India. Then he obtained his Master's degree in Computer and Information Technology from Manonmanium Sundaranar University, India. In 2018, he received his Doctor of Philosophy in Computer Science and Engineering from Noorul Islam Centre for Higher Education, Kanyakumari, India.

Dr. M. Ramesh Kumar

Ph.D (Computer Science and Engineering), M.E (Computer Science and Engineering).

Currently working as Associate Professor in VSB College of Engineering Technical Campus, Coimbatore.

Dr. Maheshwar Shrestha

Postdoctoral Research Fellow in DEPT. OF ELE ENGG & COMP SCI, SDSU, Brookings, SD Ph.D, M.Sc. in Electrical Engineering from SOUTH DAKOTA STATE UNIVERSITY, Brookings, SD.

Dr. D. Amaranatha Reddy

Ph.D. (Postdoctoral Fellow, Pusan National University, South Korea), M.Sc., B.Sc. : Physics.

Dr. Dibya Prakash Rai

Post Doctoral Fellow (PDF), M.Sc., B.Sc., Working as Assistant Professor in Department of Physics in Pachhungga University College, Mizoram, India.

Dr. Pankaj Kumar Pal

Ph.D R/S, ECE Deptt., IIT-Roorkee.

Dr. P. Thangam

PhD in Information & Communication Engineering, ME (CSE), BE (Computer Hardware & Software), currently serving as Associate Professor in the Department of Computer Science and Engineering of Coimbatore Institute of Engineering and Technology.

Dr. Pradeep K. Sharma

PhD., M.Phil, M.Sc, B.Sc, in Physics, MBA in System Management, Presently working as Provost and Associate Professor & Head of Department for Physics in University of Engineering & Management, Jaipur.

Dr. R. Devi Priya

Ph.D (CSE), Anna University Chennai in 2013, M.E, B.E (CSE) from Kongu Engineering College, currently working in the Department of Computer Science and Engineering in Kongu Engineering College, Tamil Nadu, India.

Dr. Sandeep

Post-doctoral fellow, Principal Investigator, Young Scientist Scheme Project (DST-SERB), Department of Physics, Mizoram University, Aizawl Mizoram, India- 796001.

Dr. Roberto Volpe

Faculty of Engineering and Architecture, Università degli Studi di Enna "Kore", Cittadella Universitaria, 94100 – Enna (IT).

Dr. S. Kannadhasan

Ph.D (Smart Antennas), M.E (Communication Systems), M.B.A (Human Resources).

Research Area: Engineering Physics, Electromagnetic Field Theory, Electronic Material and Processes, Wireless Communications.

Mr. Bhavinbhai G. Lakhani

An expert in Environmental Technology and Sustainability, with an M.S. from NYIT. Their specialization includes Construction Project Management and Green Building. Currently a Project Controls Specialist Lead at DACK Consulting Solutions, they manage project schedules, resolve delays, and handle claim negotiations. Prior roles as Senior Project Manager at FCS Group and Senior Project Engineer at KUNJ Construction Corp highlight their extensive experience in project estimation, resource management, and on-site supervision.

Mr. Omar Muhammed Neda

Department of Electrical Power Engineering, Sunni Diwan Endowment, Iraq.

Mr. Amit Kumar

Amit Kumar is associated as a Researcher with the Department of Computer Science, College of Information Science and Technology, Nanjing Forestry University, Nanjing, China since 2009. He is working as a State Representative (HP), Spoken Tutorial Project, IIT Bombay promoting and integrating ICT in Literacy through Free and Open Source Software under National Mission on Education through ICT (NMEICT) of MHRD, Govt. of India; in the state of Himachal Pradesh, India.

Mr. Tanvir Singh

Tanvir Singh is acting as Outreach Officer (Punjab and J&K) for MHRD Govt. of India Project: Spoken Tutorial - IIT Bombay fostering IT Literacy through Open Source Technology under National Mission on Education through ICT (NMEICT). He is also acting as Research Associate since 2010 with Nanjing Forestry University, Nanjing, Jiangsu, China in the field of Social and Environmental Sustainability.

Mr. Abilash

MTech in VLSI, BTech in Electronics & Telecommunication engineering through A.M.I.E.T.E from Central Electronics Engineering Research Institute (C.E.E.R.I) Pilani, Industrial Electronics from ATI-EPI Hyderabad, IEEE course in Mechatronics, CSHAM from Birla Institute Of Professional Studies.

Mr. Varun Shukla

M.Tech in ECE from RGPV (Awarded with silver Medal By President of India), Assistant Professor, Dept. of ECE, PSIT, Kanpur.

Mr. Shrikant Harle

Presently working as a Assistant Professor in Civil Engineering field of Prof. Ram Meghe College of Engineering and Management, Amravati. He was Senior Design Engineer (Larsen & Toubro Limited, India).

Mr. Zairi Ismael Rizman

Senior Lecturer, Faculty of Electrical Engineering, Universiti Teknologi MARA (UiTM) (Terengganu) Malaysia Master (Science) in Microelectronics (2005), Universiti Kebangsaan Malaysia (UKM), Malaysia. Bachelor (Hons.) and Diploma in Electrical Engineering (Communication) (2002), UiTM Shah Alam, Malaysia.













Mr. Ronak

Qualification: M.Tech. in Mechanical Engineering (CAD/CAM), B.E.

Presently working as a Assistant Professor in Mechanical Engineering in ITM Vocational University, Vadodara. Mr. Ronak also worked as Design Engineer at Finstern Engineering Private Limited, Makarpura, Vadodara.

Table of Contents

Volume-11, Issue-9, September 2025

S. No	Title	Page No.
1	<p>Analysis of the Storage Capacity of An Uncooled MH Tank</p> <p>Authors: Romana Dobáková; Lukáš Tóth; Natália Jasminská; Peter Milenovský</p> <p> DOI: https://dx.doi.org/10.5281/zenodo.17227191</p> <p> DIN Digital Identification Number: IJOER-SEP-2025-1</p>	01-06
2	<p>Hamilton's Principle and Energy Profitability</p> <p>Authors: Korotkevich S.V</p> <p> DOI: https://dx.doi.org/10.5281/zenodo.17227209</p> <p> DIN Digital Identification Number: IJOER-SEP-2025-3</p>	07-18
3	<p>Pan-genome Sequence Alignment Algorithm Research</p> <p>Authors: LuFang Yu</p> <p> DOI: https://dx.doi.org/10.5281/zenodo.17227241</p> <p> DIN Digital Identification Number: IJOER-SEP-2025-4</p>	19-32
4	<p>Analysis of Global Trade Competition Pattern of New Energy Vehicles and Fuel Vehicles based on Multi-Layer Network</p> <p>Authors: QiYu Hu</p> <p> DOI: https://dx.doi.org/10.5281/zenodo.17227251</p> <p> DIN Digital Identification Number: IJOER-SEP-2025-6</p>	33-46
5	<p>Solar versus Electrolysis Methods for Green Hydrogen Production: A Meta-Analysis of Efficiency, Yield, and Cost Performance</p> <p>Authors: Arjun Aditya Shah</p> <p> DOI: https://dx.doi.org/10.5281/zenodo.17227267</p> <p> DIN Digital Identification Number: IJOER-SEP-2025-7</p>	47-66
6	<p>Analysis of Pressure Losses of Selected Filtration Materials</p> <p>Authors: Romana Dobáková; Tomáš Brestovič; Natália Jasminská</p> <p> DOI: https://dx.doi.org/10.5281/zenodo.17227285</p> <p> DIN Digital Identification Number: IJOER-SEP-2025-8</p>	67-72

Analysis of the Storage Capacity of An Uncooled MH Tank

Romana Dobáková^{1*}; Lukáš Tóth²; Natália Jasminská³; Peter Milenovský⁴

Department of Energy Engineering, Faculty of Mechanical Engineering, Technical University of Košice, Slovakia

*Corresponding Author

Received: 01 September 2025/ Revised: 08 September 2025/ Accepted: 13 September 2025/ Published: 30-09-2025

Copyright © 2025 International Journal of Engineering Research and Science

This is an Open-Access article distributed under the terms of the Creative Commons Attribution Non-Commercial License (<https://creativecommons.org/licenses/by-nc/4.0>) which permits unrestricted Non-commercial use, distribution, and reproduction in any medium, provided the original work is properly cited.

Abstract— *The need for cooling of metal hydride (MH) tanks during the hydrogen absorption process is a well-known fact, especially when it is necessary to achieve full absorption of the alloy with hydrogen within a short time frame. However, effective cooling of the tank is not always possible. The absence of cooling significantly extends the absorption time or reduces the absorption capacity of the alloy, which is crucial for the competitive operation of a metal hydride tank. This article focuses on the effect of the absence of an external cooling system on the change in the absorption capacity of the MH alloy within a defined filling time frame.*

Keywords— *Metal Hydride, Hydrogen, Absorption, MH alloy.*

I. INTRODUCTION

Hydrogen is considered one of the most promising energy carriers, as it is renewable and has the potential to significantly contribute to decarbonization and the reduction of greenhouse gas emissions not only in transportation but also in the energy sector and industry. However, efficient and safe storage of hydrogen presents a major challenge for the further development of hydrogen energy.

One of the main obstacles in hydrogen storage, whether for short-term or long-term use, is its very low energy density, small molecular size, and wide explosive concentration range when mixed with air. These negative factors significantly complicate its safe storage and distribution within the hydrogen infrastructure. This is evident not only in its use at refuelling stations for hydrogen-powered vehicles but also in heating systems, where previously unforeseen complications can arise.

Solving the issue of effective and safe hydrogen storage is a key prerequisite for its broad application in both industrial and mobile uses. If hydrogen is to become a competitive energy carrier in the near future, its storage method must meet multiple criteria particularly low cost, long service life, ease of installation, and other technical, safety, and economic requirements.

The most common hydrogen storage solutions include systems based on compression, absorption, adsorption, and liquid carriers, whether it be liquefied hydrogen or liquid organic hydrogen carriers (LOHC). Each of these methods has its own advantages and disadvantages in terms of mass and volumetric density, cost, filling and release speed, as well as durability and safety.

Therefore, the selection of a suitable storage method always depends on the specific application whether it is mobile or stationary, short-term or long-term.

II. METAL HYDRIDE ALLOYS

Storing hydrogen in metal hydride alloys represents one of the innovations in the development of alternative technologies for both short-term and long-term hydrogen storage. In this method, hydrogen chemically bonds with metals or metal alloys, forming so-called metal hydrides. These materials are capable of reversibly absorbing and releasing molecular hydrogen under specific pressure and temperature conditions, allowing for repeated cycles without significant degradation of the material.

When in contact, gaseous molecular hydrogen reacts with the metal alloy, dissociates into atomic hydrogen, and subsequently diffuses into the intermetallic structure of the alloy, forming a metal hydride (MH) according to the general reaction:



Where M is a metallic solid solution or intermetallic compound, H – hydrogen, x – molar fraction of hydrogen (1), MH_x – corresponding metal hydride, Q – reaction heat ($J \cdot mol^{-1}$).

The process of hydrogen absorption into metal hydride alloys is accompanied by an exothermic reaction, during which a significant amount of thermal energy is released. Due to the thermal load, it is essential to ensure an effective cooling system for the MH tank, as increased temperature negatively affects the absorption kinetics, leading to a slower absorption process.

The absorption and desorption processes occur at relatively low pressures and temperatures, making this method suitable for both industrial and mobile applications, as it does not require powerful compressors, pressure boosters, or cryogenic cooling systems.

MH tanks allow compact storage of hydrogen in the solid phase with high volumetric density, which significantly increases the overall safety of the system. Since most of the hydrogen in the tank is bound within the structure of the metallic material, the risk of hydrogen diffusion through connecting elements is minimized due to the lower pressure exerted by hydrogen on these joints.

The main disadvantages of metal hydride hydrogen storage include low gravimetric capacity, as most commonly used alloys can store only 1–2 wt.% of hydrogen, which is a significant limitation, especially for mobile applications. Another drawback is the higher weight of the entire system, which negatively affects its usability in transportation vehicles.

An additional challenge is thermal management, since the exothermic absorption of hydrogen requires effective cooling, while desorption demands heat input. Moreover, the cost and availability of certain key elements such as lanthanum, vanadium, or titanium significantly increase the production costs of these materials.

III. STORAGE CAPACITY OF AN UNCOOLED MH TANK AS A FUNCTION OF ABSORPTION PRESSURE

For the purpose of the experiment on the storage capacity of a MH alloy as a function of temperature, the Hydralloy C5 alloy was used. It is a metallic alloy with the chemical composition $Ti_{0.95}Zr_{0.05}Mn_{1.46}V_{0.45}Fe_{0.09}$. These materials are capable of absorbing hydrogen from the gas phase at low temperatures and pressures, forming reversible metal hydrides, which makes them suitable for hydrogen storage.

During the absorption process, the metal hydride alloy releases heat, which must be effectively removed from the system to maintain the desired kinetics of the entire process.

The amount of heat Q_{stored} , released during full saturation of the metal hydride alloy with hydrogen can be calculated using the following equation:

$$Q_{\text{stored}} = \frac{m_{\text{MH}} \cdot \alpha_{\text{MH}}}{\rho_{H_2} \cdot 100} \cdot Q_{\text{MH}} \quad (2)$$

where m_{MH} weight of MH alloy in tank (kg), α_{MH} – gravimetric storage percentage (%), ρ_{H_2} – density of hydrogen under standard conditions ($kg \cdot m^{-3}$), Q_{MH} – amount of heat released during absorption of 1 m^3 of hydrogen (J).

The thermal power that must subsequently be removed from the tank is determined by the following relation:

$$P_{\text{stored}} = \frac{Q_{\text{stored}}}{\tau} \quad (3)$$

where τ is time of filling of the tank (s).

The storage capacity of the MH alloy is also influenced by the absorption pressure. As can be seen in Fig. 1, the alloy exhibits the highest storage capacity at a pressure of 67 bar (6.7 MPa). It is also evident that beyond a certain pressure value, further increases in pressure do not lead to a significant increase in the alloy's capacity. This is because the alloy's structure is unable to absorb additional amounts of hydrogen despite the increasing pressure. The subsequent increase in the volume of stored hydrogen in the MH tank then proceeds similarly to that in standard high-pressure tanks.

For the purpose of experimentally determining the gravimetric storage capacity of the uncooled MH alloy, a shortened MNTZV-60 type tank equipped with an integrated internal thermometer was used. This is a low-pressure metal hydride hydrogen tank suitable for both mobile and stationary applications (Fig. 2). The tank was connected to a compressed hydrogen supply line, where a flow meter with a maximum flow capacity of $20 \text{ l} \cdot \text{min}^{-1}$ and a pressure gauge with a range up to 40 bar (4 MPa) were installed on the inlet pipe.

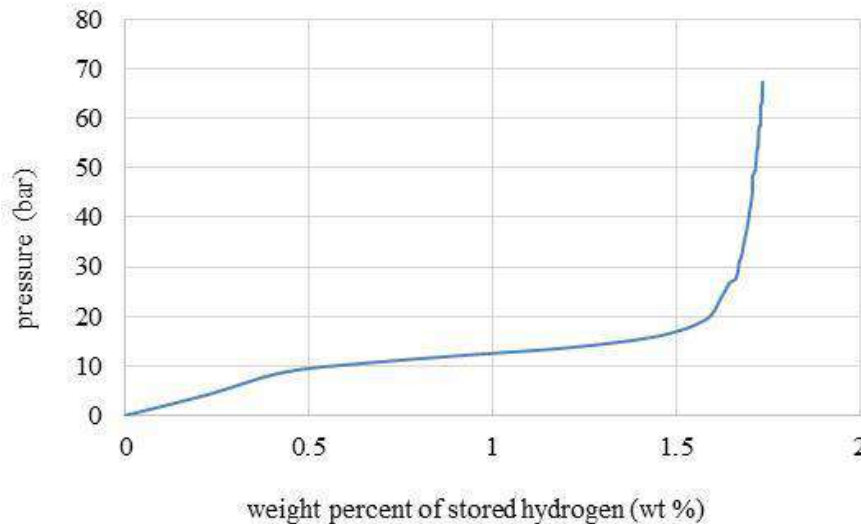


FIGURE 1: Change in storage capacity with increasing pressure at 20 °C (ideal storage capacity)

Before the measurement, the tank was activated in accordance with the manufacturer's methodology. Subsequently, a four-hour vacuuming of the system was performed to a relative pressure of -1 bar to ensure optimal conditions for hydrogen absorption. After vacuuming, the maximum hydrogen flow at the desired pressure was set to $20 \text{ l} \cdot \text{min}^{-1}$ using a needle valve and bypass. Once the flow stabilized, the bypass was closed and the tank valve was opened, allowing hydrogen to flow directly into the tank. The experiment was conducted at room temperature of 23 °C. The total filling time was set to 30 minutes, which can be considered a technologically acceptable filling time for this type of tank.

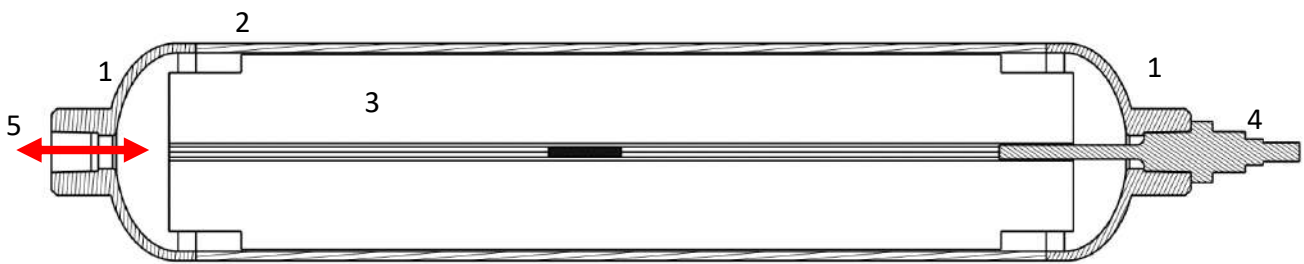


FIGURE 2: MNTZV-60 type tank equipped with an integrated internal thermometer

1 – tank cover, 2 – cylindrical part of tank, 3 – aluminium heat transfer intensifier, 4 – thermometer, 5 – inlet and outlet of hydrogen

During the experiment, the tank was filled at three different pressures: 10, 20, and 30 bar. For each of these values, the gravimetric storage capacity of the tested MH alloy (w_{MH}) under real (uncooled) conditions was determined as the ratio between the mass of absorbed hydrogen and the mass of the alloy:

$$w_{\text{MH}} = \frac{m_{\text{H}_2}}{m_{\text{MH}}} \cdot 100 \quad (\text{wt.}\%) \quad (4)$$

where m_{H_2} is weight of stored hydrogen (kg), m_{MH} – weight of MH alloy (1.567 kg).

The mass of stored hydrogen is determined by the relation:

$$m_{H_2} = \rho_{H_2} \cdot V_{\text{stored } H_2} \text{ (kg)} \quad (5)$$

where $V_{\text{stored } H_2}$ is the volume of hydrogen stored in the metal hydride alloy (m^3), ρ_{H_2} – hydrogen density ($\text{kg}\cdot\text{m}^{-3}$).

Table 1 shows the gravimetric storage capacities of the MH alloy at the three tested pressures. As can be seen from the table, the storage capacity of the MH alloy increases with increasing pressure, which is caused by the improved absorption properties of the material at higher hydrogen pressures. The increase in storage capacity of the uncooled MH alloy with rising pressure follows the same trend as in the case of the cooled MH alloy.

TABLE 1
STORAGE CAPACITY OF THE MH ALLOY AT THE INVESTIGATED PRESSURES

Pressure (bar)	$t_{MH,max}$ (°C)	$V_{\text{stored } H_2}$ (m^3)	ρ_{H_2} ($\text{kg}\cdot\text{m}^{-3}$)	m_{H_2} (kg)	w_{H_2} (wt.%)
10	40	0.0396	0.08988	0.003559	0.2271
20	50	0.0633	0.08988	0.005689	0.3631
30	60	0.0956	0.08988	0.008593	0.5483

In comparison with the storage capacity at 20 °C (see Fig. 1), it can be observed that the storage capacity decreases as the temperature inside the tank increases. This reduction in storage capacity is a consequence of the exothermic nature of the reaction between hydrogen and the alloy. As the alloy's temperature rises, the reaction slows down, leading to a decrease in the amount of hydrogen that can be stored within a given time.

Figure 3 illustrates the dependence of the alloy's temperature change during hydrogen absorption at three different pressures as a function of the filling time of the MH alloy.

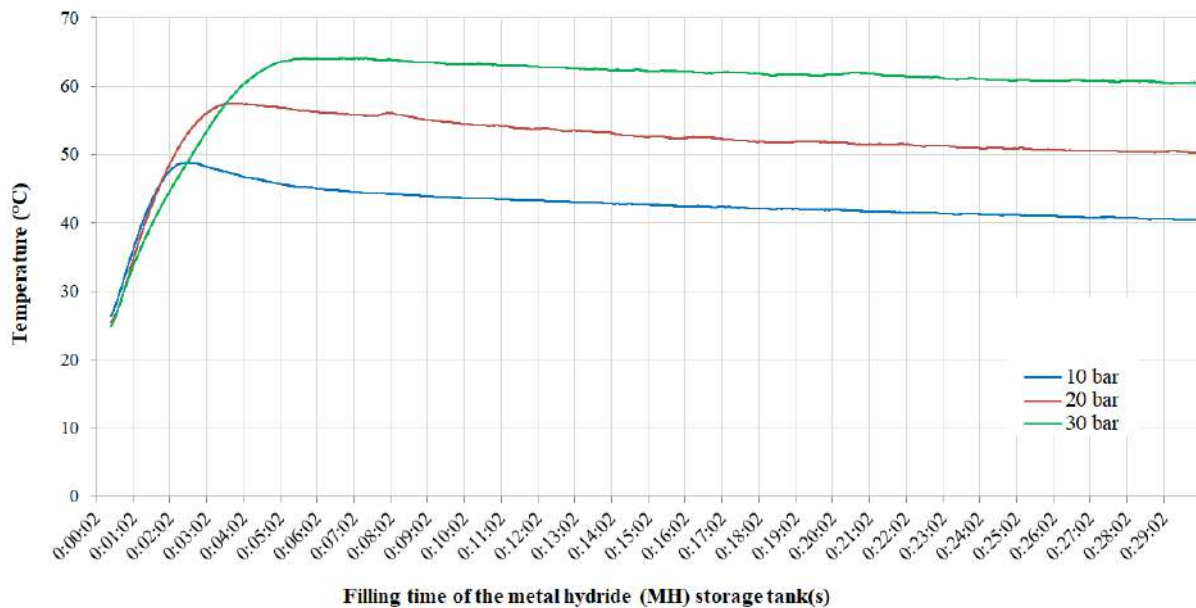


FIGURE 3: Change in alloy temperature during hydrogen absorption at three different pressures as a function of MH alloy filling time

The graph shows that higher hydrogen pressure allows the absorption process to proceed even at an increased temperature of the MH alloy. As a result, the fast absorption phase can last longer, leading to the binding of a greater amount of hydrogen before the alloy reaches a temperature at which the absorption kinetics significantly slow down.

Figure 4 presents a comparison of the hydrogen flow into the MH alloy and the total amount of hydrogen stored in the MH alloy as a function of filling time at three different hydrogen pressure levels.

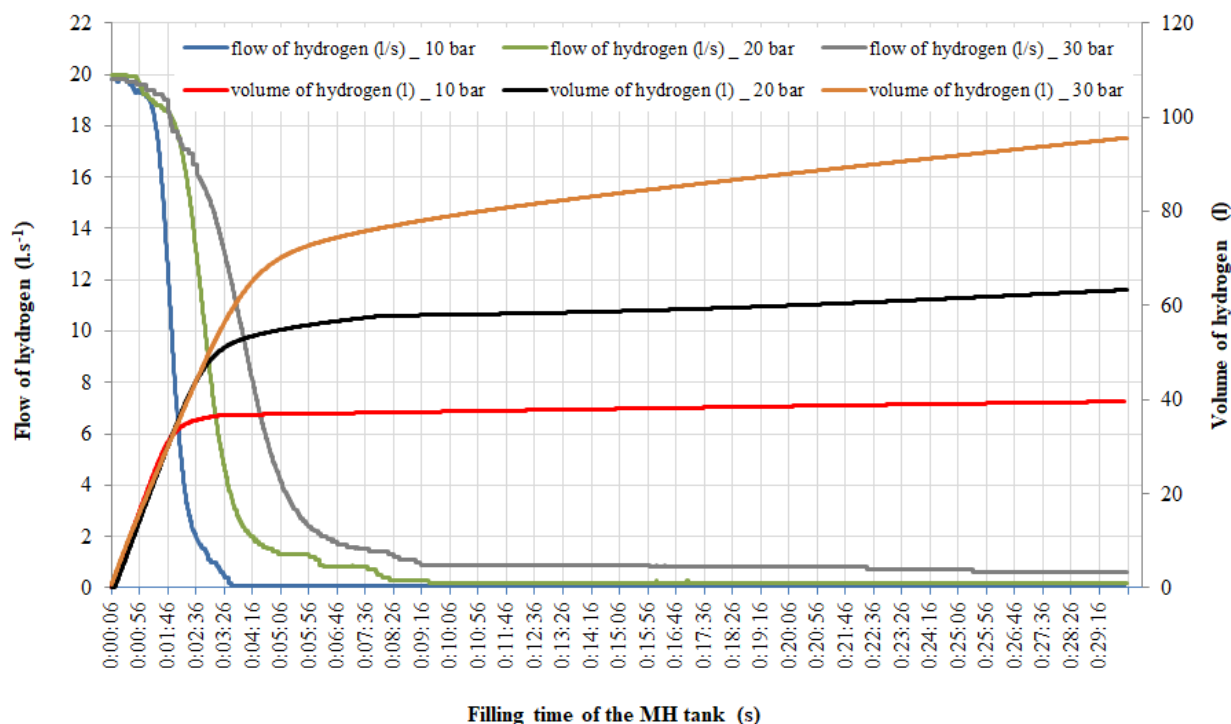


FIGURE 4: Hydrogen flow into the MH alloy and the total amount of hydrogen stored in the MH alloy as a function of filling time at three different hydrogen pressure levels

The hydrogen flow into the MH alloy exhibits a nonlinear behaviour. Higher hydrogen pressure prolongs the phase of intensive hydrogen absorption into the alloy before the onset of its slowdown, enabling more efficient use of the alloy's absorption capacity within a shorter time. As the pressure increases, the total amount of hydrogen that can be absorbed into the alloy during the same time interval also rises. Although higher pressure accelerates the initial absorption process, it simultaneously causes more intense heat release, leading to overheating of the MH alloy and subsequent slowing down of the absorption reaction kinetics.

IV. CONCLUSION

Even when using internal elements to improve heat transfer (intensifiers), an external cooling system remains essential to maintain optimal hydrogen absorption conditions in MH tanks if the filling process is time-limited. Otherwise, heat accumulates, leading to an increase in alloy temperature and a consequent decrease in absorption capacity.

Experimental results show that at a pressure of 10 bar, the stored hydrogen capacity at 40 °C is approximately 65.06% lower than at 20 °C; at 20 bar, it is 77.31% lower; and at 30 bar, the difference between the ideal storage capacity and the capacity of the uncooled MH tank with limited filling time is 66.77%.

By extending the tank filling time at a given pressure, the actual storage capacity would gradually approach the ideal capacity, and after a sufficiently long period, the difference between ideal and real filling times would completely disappear.

The development of systems for adequate cooling of MH tanks during the absorption process is crucial for their wider adoption, along with research into heat dissipation systems from the tank core, as the thermal conductivity of powdered alloys significantly complicates this process.

Alongside cooling research, the development of new alloys with improved properties such as higher capacity, faster kinetics, and better thermal conductivity must also proceed. This progress could significantly expand the usability of metal hydrides and contribute to the broader spread of the hydrogen economy.

ACKNOWLEDGEMENTS

This work was supported by the Slovak Research and Development Agency under the Contract no. APVV-21-0274 and APVV-23-0266. Further supported by VEGA granting agency within the Project No. 1/0224/23, Project No. 1/0587/25; by KEGA granting agency within the Project No. 031TUK-4/2025.

REFERENCES

- [1] Kölbig, M., Bürger, I., Linder, M.: *Thermal applications in vehicles using Hydralloy C5 in single and coupled metal hydride systems*. In: Applied Energy. 287, 2021, 116534.
- [2] Capurso, G. and et al.: *Development of a modular room-temperature hydride storage system for vehicular applications*. In: Applied Physics. 122, 2016, 236.
- [3] Giorgio, D.P and et al.: *Innovative battery thermal management system based on hydrogen storage in metal hydrides for fuel cell hybrid electric vehicles*. In: Applied Energy. 315, 2022, 118935.
- [4] Jasminská, N., Brestovič, T., Lázár, M.: *Výroba a uskladnenie vodíka*. Košice: TU, 2015. 141 p. ISBN 978-80-553-2378-7.
- [5] Martin, M., Gommel, C., Borkhart, C., Fromm, E.: *Absorption and desorption kinetic of hydrogen storage alloys*. In: Journal of Alloys and Compounds. 238 (1-2), 1996, 193-201.
- [6] Rudman, P.S.: *Hydriding and dehydriding kinetics*. In: J. Less-Common Met. 89(1), 1983, 93-110

Hamilton's Principle and Energy Profitability

Korotkevich S.V

RUP "Gomelenergo", Gomel, Belarus

Received: 03 September 2025/ Revised: 09 September 2025/ Accepted: 16 September 2025/ Published: 30-09-2025

Copyright © 2025 International Journal of Engineering Research and Science

This is an Open-Access article distributed under the terms of the Creative Commons Attribution Non-Commercial License (<https://creativecommons.org/licenses/by-nc/4.0>) which permits unrestricted

Non-commercial use, distribution, and reproduction in any medium, provided the original work is properly cited.

Abstract— *The kinetics of the interface between metals under contact and external influences (triboloading, rolling, physical and chemical effects of the environment, etc.) has been investigated. It is shown that the kinetics of the evolution of the structure of materials proceeds in accordance with the minimum production of entropy and maximum destruction. The conditions for obtaining a special nonequilibrium state of the crystal lattice of nickel under triboloading are determined. The main regularities of the kinetics of structural transformations, structural-scale levels of deformation and the properties of the interface between metals during contact and external interaction have been determined.*

Keywords— *principle of least action, energy profitability, nanocrystalline and submicrocrystalline structures invariants; dislocations, stresses, laws of kinetics, entropy, destruction.*

I. INTRODUCTION

The accumulated experimental database in the field of research of metal interface kinetics does not allow to use it to the full extent to create a database, for example, on tribotechnical characteristics and wear. The experimental data given in different sources differ from each other. On the one hand, this can be explained by some differences in the modes and technologies of obtaining the surface, as well as the conditions of their testing, and on the other hand by the lack of scientifically sound fundamental principles and, as a consequence, measurement parameters. The fragmentation of fundamental research directions and purely practical approach to solve applied and immediate problems, unfortunately, does not allow to concentrate efforts on classification and systematization of data in the fields of metallophysics, tribochemistry, condensed state physics and nanomaterial science. The obtained results of plastic deformation studies are often controversial and sometimes contradictory. The current state of the problem of studying the surface kinetics of metals and the creation, including nanomaterials is characterized as a transitional period between the accumulation of experimental data and their interpretation in the categories of mechanics, physics, chemistry and the development of generalizing invariants and regularities that do not depend on the modes, conditions and technologies of their production [1, 2].

The lack of a systematic approach leads to the fact that the problem of contact interaction of surfaces of different materials in terms of optimal selection to improve their wear resistance has not yet been solved. Experimenters, unfortunately, do not take into account the large-scale factor of external influence, for example, load-velocity parameters on the surface of materials. Obtaining a momentary and quick "positive" result of research puts the experimenter in the limited conditions of hard, not soft impact on the material. As a result, as a rule, many processes (heat conduction, diffusion, mass transfer, hardening, amorphization, fracture, etc.) occur simultaneously and we cannot divide a complex process into composite and simpler ones. It is this systematic and thorough approach that allows researchers to divide a complex process into simple processes and establish the course of the dominant process in their diversity and, as a consequence, to identify and establish the main fundamental regularities describing this simple process. The level of understanding of the problem by the author of this article is fully consistent with the works and statements of R. Feynman, V.D. Kuznetsov and I.V. Kragelsky [3–5] and others. The most common fatigue [6], energy [7] and lobe [8] theories do not consider the kinetics of layer-by-layer hardening and fracture of the surface layer of metals in detail, taking into account all (nano, micro, meso and macro) structural and scale levels of deformation. The mechanisms of fragmentation and relaxation channels of strain energy accumulated in the surface layers of conjugated materials are not fully understood. The process of superplasticity has not been fully investigated in which the

conditions of amorphization of the surface layer and facilitated slip of submicro and nanostructured elements relative to each other will be realized in the absence of hardening. Understanding of the short-range interaction between inter-nodal atoms and the electronic subsystem in the formation of nonequilibrium states of nanoclusters and their conglomerates will make it possible to realize corporate phenomena in nanomaterials to reduce their brittleness and increase their operational properties [9, 10].

Another reason for not studying this issue is the lack of fundamental approaches and scientific ideas for the study of strongly nonequilibrium thermodynamic systems. In the case of a nonequilibrium state of a surface in the accumulation of its strain energy using various model representations, the problem of interpreting the results of quantitative assessment of the magnitude of stresses and dislocation density arises [11].

Plastic deformation of solids is realized at several interrelated structural levels, the scale of which is determined by the physical nature of structural defects responsible for the shape change [12]. In most cases, the distribution of localization zones is ordered in space and time, and the type of localization is determined by the law of plastic flow. Consideration of a solid body as a multilevel hierarchically organized system consisting of 3D-crystalline and 2D-planar subsystems causes a sharp increase in the role of the curvature of the crystal structure in describing the behavior of solids in the fields of external contact effects [13, 14].

The purpose of the work is to determine the physical essence of the principle of least action and energy benefit to describe physical systems under external actions.

II. EXPERIMENTAL DETAILS

The effectiveness of studies of physical regularities of plastic deformation, hardening and fracture of surface layers of solid bodies under their frictional loading is largely determined by the level of experimental research due to the correctness of the applied methods, correctness and sufficient sensitivity of the applied research methods. In order to solve the problem of hardening and fracture of metal surface layers under frictional loading, it was necessary to use a wide range of modern physical research methods, such as ferromagnetic resonance, transmission electron microscopy, X-ray diffraction and metallographic analysis, medium and low energy electronography, etc. [15]. In accordance with the specifics of the tasks to be solved and the properties of the investigated objects, in some cases it was necessary to create specialized equipment [15]. In this regard, a technique for estimating the dislocation density was developed and the ferromagnetic resonance apparatus was created [15]. For electron-microscopic studies of the structure on the "lumen", the methods were improved and the tribometer units of specimen testing and unilateral electrolytic thinning were created [15].

Nuclear magnetic resonance (NMR) and electron paramagnetic resonance (EPR) methods have been widely used to study the wear kinetics of surface layers under triboloading [16]. The complex of these methods, along with transmission electron microscopy, allowed us to establish the relationship between the microstructure of the surface layers of solids and changes in the lubricating medium and wear kinetics.

The priority elements of this study are also the techniques of specimen preparation, their friction testing and a comprehensive study by the above mentioned methods. The disks of $\approx 5 \times 0.5 \text{ mm}^2$ were cut from 99.99% purity nickel foil produced by electron-beam melting using the electrospark method. Before friction testing, the specimens were electrolytically polished and annealed in a vacuum of 0.133 mPa at 973 K. The friction test was carried out on a machine of type AE-5 with a precision setting of the contact plane [15]. Triboloading of sliding Ni-Mo pair was carried out mainly in TsIATIM-201 grease at nominal contact pressure ≈ 84 and $\approx 168 \text{ kPa}$ and linear velocity $\approx 0.5 \text{ m/s}$.

Experimental FMR methods are the most convenient in the study of the dislocation structure of ferromagnetics, because at the frequency of the external electromagnetic field $\nu = 9600 \text{ MHz}$, the broadening of the resonance absorption line in a deformed ferromagnet is caused by the elastic fields of dislocations, while small-scale defects (vacancies, embedded atoms) and large-scale defects (cracks, pores, etc.) drop out of the absorption spectrum [15]. In these works, the dependence between the width of the FMR line (ΔH) and the dislocation density (ρ) was established. In the strain range $\varepsilon \approx 0 - 75 \%$ there is a linear dependence between the line broadening and dislocation density. At large deformations, the broadening of the FMR line is described by an inverse root dependence. The absence of line broadening in a deformed ferromagnet with a magnetostriction

constant equal to zero (permalloy) confirms the physical meaning of ΔH broadening due to local magnetic fields around dislocations [17, 18].

Another advantage of this method is that at this frequency, the penetration depth (δ) of the ultra-high frequency (UHF) field in metallic materials is $\delta = 10^{-7}$ to 10^{-6} m. This determines the selectivity of the method for the informativeness of the defective microstructure of thin surface layers, especially under frictional loading, when plastic deformation covers these layers commensurate with the skin layer thickness [19]. In accordance with the above provisions of FMR, direct electron microscopic and X-ray diffraction studies of thin surface layers of steel [20], the observed cyclic dependence $\Delta H = f(t)$ reflects the kinetics of the dislocation structure of the surface layer of a frictionally loaded ferromagnetic.

Electron-microscopic studies of nickel were carried out on an EVM-100AK microscope using the thin foil method “per lumen” and HITACHI H-800. The dislocation density data were obtained by averaging, while viewing, at least five localized sites in different grains.

It should be noted that triboloading is a small-amplitude, alternating (compression and tension of near-surface volumes) and cyclic contact loading of metal surfaces [21-23], where hardening and fracture can only be represented from dislocation representations [24].

III. RESULTS AND DISCUSSION

3.1 Using the principle of least action (PLA) to describe physical systems:

It is known that PLA or Hamilton's principle principle is used to formulate the equations of motion of a material point in mechanics [25]. Why this fundamental principle cannot be used to describe the kinetics of the processes of structural transformations in materials occurring in the same continuum of space and time? The question naturally arises, namely: where there is symmetry, there should be invariants to describe the kinetics of various structural transformations in multilevel, hierarchically organized processes occurring on the surface of metals? The kinetics of the system transition from one structural state (A) to another (B) is carried out in accordance with the PLA describing all structural-scale levels of deformation (Fig. 1).

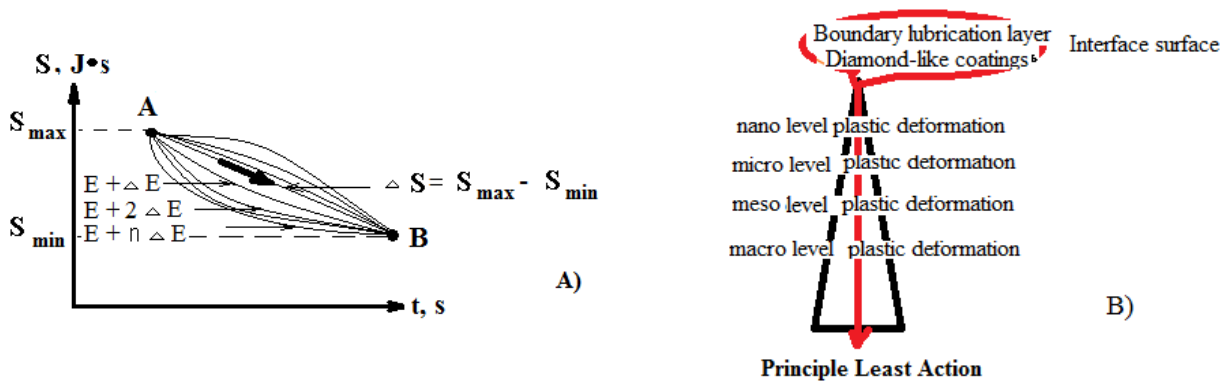


FIGURE 1: Principle Least Action (PLA): a) kinetics of system transition from one structural state (A) to another (B) according to LAP, where S – action, t – time; b) PLA action scheme covering all structural-scale levels of deformation

It is known that the mathematical formulation of the PLA for the motion of a material point is [25]:

$$\delta S = 0, \quad (1)$$

Where

$$S = \int_{t_1}^{t_2} L(q, q', t) dt \quad (2)$$

where q, q' – independent parameters characterizing the system, t – time. The integral in expression (2) takes the minimum value along the straight line AB (Fig. 1, A) and the expression is valid:

$$\delta S = \int_{t_1}^{t_2} \left(\frac{\partial L}{\partial q} \delta q + \frac{\partial L}{\partial q'} \delta q' \right) dt = 0 \quad (3)$$

Where the Lagrangian is given by the expression [25]:

$$L = E_{\text{kin}} - U_{\text{poten}} \quad (4)$$

Where E_{kin} – is the kinetic energy and U_{poten} – is the potential energy of the material point under the given external influence.

Under the action of external influences, ions in the nodes of the crystal lattice of metals or a set of ions forming the nucleus of a linear defect-dislocation or a set of dislocations in the form of boundaries (NC) or SMC structures move in elastic stress fields. In mechanics, the equation of motion of a material point is described by Newton's second law or using the principle of least action (PLA). The PLA was used to determine the frequency of oscillations of crystal sublattices ($\approx 4.87 \cdot 10^{13} \text{ s}^{-1}$) of positive and negative ions in two atomic crystals of NaCl or CsCl under external influences [26]. Besides, the Lagrangian formalism was used to describe physical systems under friction in [27]. However, there is no idea of justification of search and establishment of invariants in these works.

The penetration of light from one medium into another is described by Fermat's principle or the principle of least time or, respectively, integration along the path of least time leads to the realization of the principle of least action of PLA [3]. The equation for the self-consistent electromagnetic field and interacting photons is given in [28].

3.2 Using the principle of energy profitability (EP) to describe physical systems:

According to the second law of thermodynamics, an open physical system tends to a state characterized by the minimum of energy that is accumulated in it under external influences (it is impossible to transfer heat from a colder body to a hotter one) [29]. Therefore, the physical system seeks channels of energy relaxation. Naturally, the system finds the path that requires the minimum value of energy expenditure or the minimum work done [30, 31]. We give specific examples from the kinetics of nickel structure evolution under triboloading or rolling, which are in full agreement with the results given in [32–34].

Pre-annealed nickel samples subjected to triboloading already at the beginning of the process at 0.9 kc form NC states in the form of closed dislocation loops or twins. Under non-equilibrium deformation conditions, it is energetically advantageous (minimum of work done) for the material to form NC states (Fig. 2), since the number of moles in this case increases by two or three orders of magnitude and, accordingly, the energy dissipation area increases. The latter forms a relaxation channel for the energy accumulated during triboloading.



FIGURE 2: Formation of nanostructures at $t = 0.9$ ks on the nickel surface at nominal contact pressure: a) 84 kPa; b) 168 kPa

The slip band blocked by the grain boundary can be simplistically represented as a curved segment of fixed length L (grain size $\approx 30 \mu\text{m}$) (Fig. 3, a) with a certain curvature λ (Fig. 3, b).

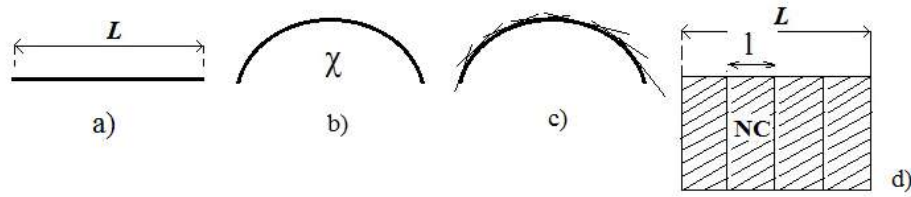


FIGURE 3: The scheme of SMC and NC states formation: a) initial structure in the form of a segment; b) structure evolution in the form of a segment bending under the action of external influences; c) beginning of SMC and NC states; d) formed SMC and NC states

Energy relaxation is realized by shifting and rotating the corresponding segments that make up the segment (Fig. 3, c), i.e., it is energetically favorable for it to break into segments (rectilinear sections) with zero or minimum possible (tending to zero) local curvature (Fig. 3, d). Energy relaxation is realized by shifting and rotating the corresponding segments that make up the segment (Fig. 3, c), i.e., it is energetically favorable for it to break into segments (rectilinear sections) with zero or minimum possible (tending to zero) local curvature (Fig. 3, d). The energy of the system in this case tends to the minimum value.

The most striking example of EP is the formation of slip bands, where a minimum of energy input is required to slide volumes of material relative to each other. Grain-boundary sliding of one grain in relation to neighboring grains, rather than grain-boundary sliding of a set of grains (10 or 100 grains) to a set of neighboring grains. In both the first and the second case, the sum of stress moments is zero and the condition of material continuity is fulfilled. However, in nature the first case is realized, i.e. the physical system chooses the path that requires minimum cost or work.

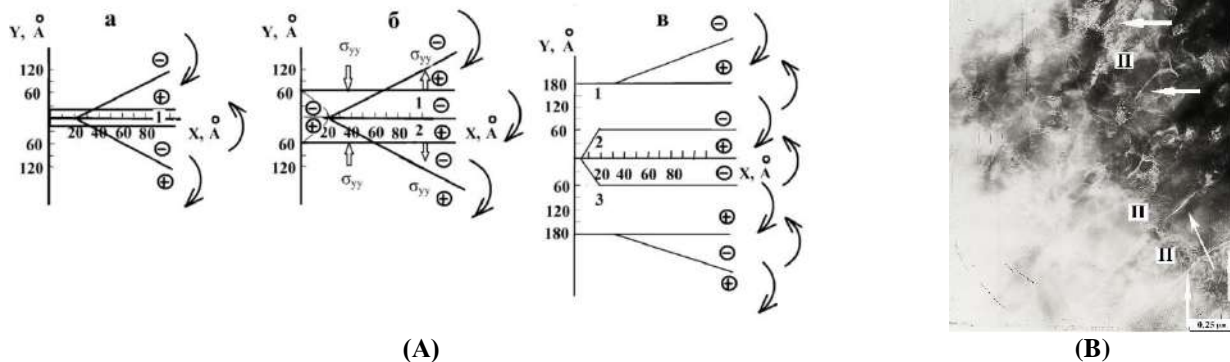
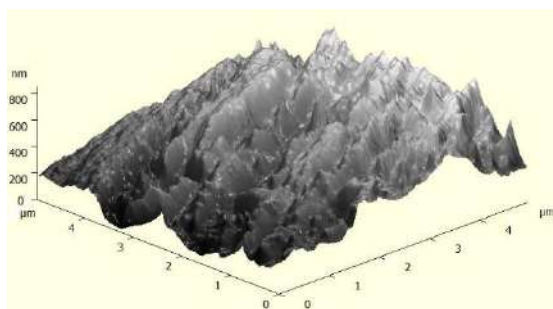
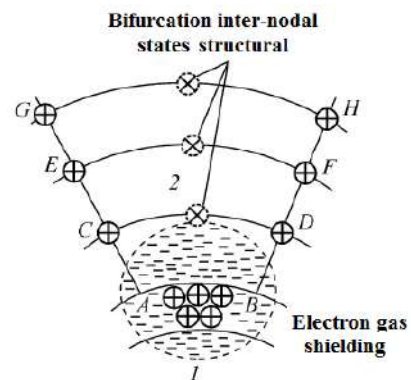


FIGURE 4: A) grain boundary slip pattern and distribution of compressive and tensile stresses, where minus the compression region, plus the stretching region; B) slip bands (arrows show microcracks along the slip bands)

The complex stress state of the compression and tension regions determines the formation of a developed relief with a folded structure on the nickel surface under triboloading (Fig. 5, a). The latter is possible only by forming a crystal lattice in the tensile regions with high local curvature (Fig. 5, b).



(A)



(B)

FIGURE 5: A) AFM image; B) bifurcation inter-nodal structural states in the zone of local curvature of the crystal lattice, where AB are clusters of positive ions at the boundary of grains 1 and 2 (B)

Similarly, the aggregation of micropores and microcracks into pores and cracks at grain boundaries (intergranular fracture) and (transgranular fracture that passes through the grain) proceeds in accordance with EB (Fig. 6).

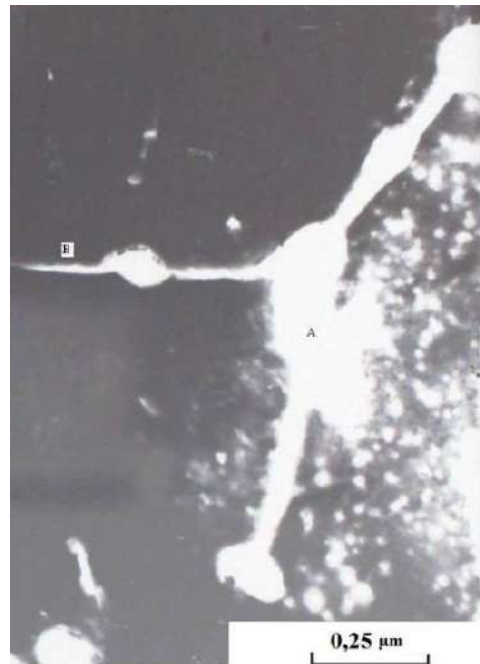


FIGURE 6: Inter- and transcrystalline fracture

Energy accumulation in the subsurface layers of nickel causes transverse sliding of dislocations in strips and their fragmentation. A submicrocrystalline structure (SMC) is formed with the time of frictional loading. The increase in image contrast confirms the accumulation of energy by the nickel surface with the triboloading time (Fig. 7).

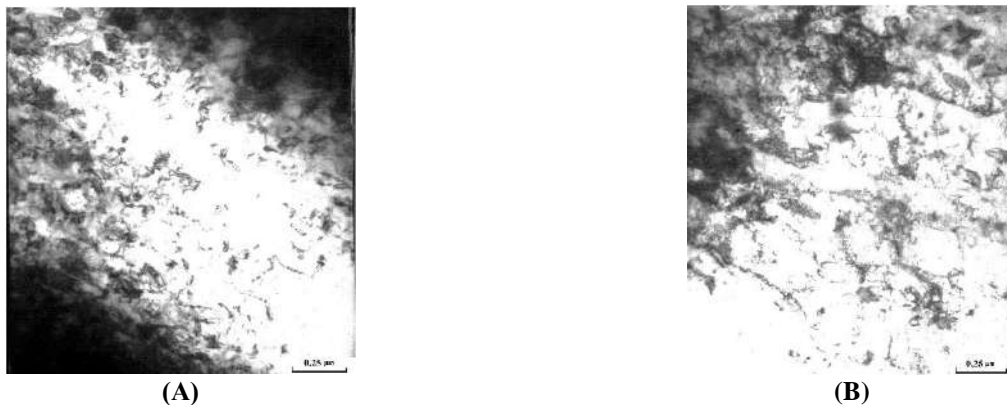


FIGURE 7: SEM images of SMC structures formed on the nickel surface with triboloading time: A) SMC structure (t = 52 ks); B) SMC structure (t = 75 ks)

The same principle of EB describes the model of lobe fracture, where the separation of the lobe is energetically advantageous and prevents the development of cracks deep into the metal. Changing the direction of the dislocation flow outward rather than inward and the onset of an avalanche-like selective mechanism of destruction of a metal layer hundreds of microns thick is also EP. The formation and motion of domain boundaries in paramagnetics, magnetic properties of paramagnetics and ferromagnetics (Larmor's theorem) in an external magnetic field are described on the basis of EP [16]. The flux of energy or work done in time to overcome the Peierls-Nabarro forces when dislocations move is also the smallest in densely packed directions. Therefore, the direction of dislocation motion coincides with the densest packing of atoms in the nodes of the crystal lattice [30].

The increase of dislocation density up to 10^{18} m^{-2} determines high catalytic activity of the surface. The latter causes a decrease in the free surface energy by transition from physical adsorption to chemisorption of the boundary lubricating layer (BLL) molecules with the metal surface (Fig. 8).

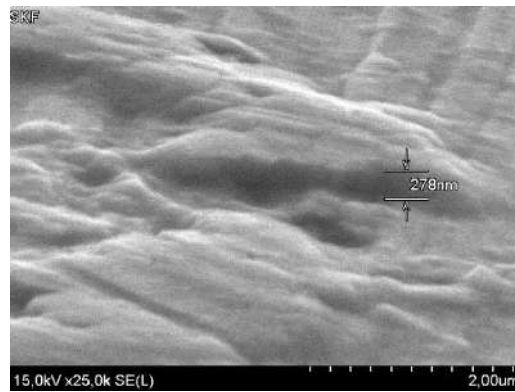


FIGURE 8: Electron microscopic image of 6202-2RS d16 C3 bearing ring surface with a chemisorbed LGBH-2 grease layer formed on it

Thus, the whole kinetics of structure formation at different scale levels, its evolution and destruction proceeds in accordance with energy profitability (Fig. 9).

The strength properties of BLL increase and the elastic modulus of such layers is ≈ 1.4 GPa, which is comparable to the elastic modulus of rubber.

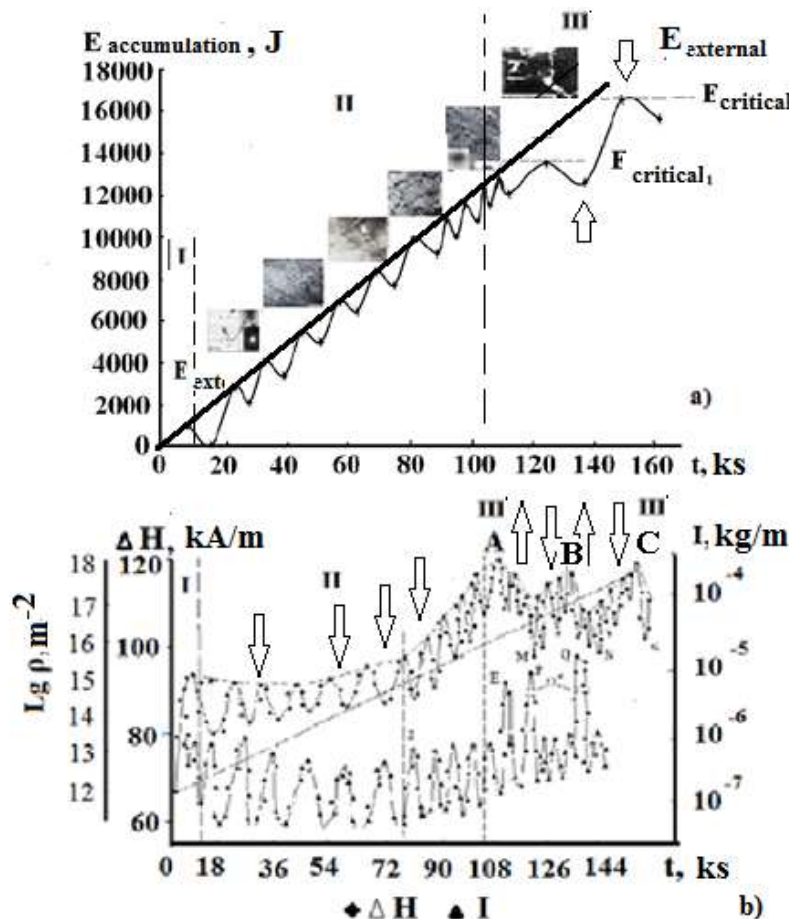


FIGURE 9: Dependence of kinetics of structural changes in the surface layer of nickel under triboloading: (a) - dependence of the external impact energy (E_{external}) of the accumulated energy (E_{ac}) on time (t), where $E_{\text{critical 1}}$ and $E_{\text{critical 2}}$ are the values of the critical energy for the destruction of the meso- and macroscale level of deformation; (b) - dependence of the broadening of the ferromagnetic resonance line (ΔH), dislocation density (ρ), wear intensity (I) on time (t) of triboloading

The number and size of defects determine the process of their interaction (Fig. 9, region III). An increase in the dislocation density up to some critical value $\rho \approx 10^{18} \text{ m}^{-2}$ determines the convergence of dislocations to a distance of $\approx 50 \text{ nm}$ and causes the overlap of the elastic fields of linear defects [15], which leads to a change in the direction of dislocation flows outward (Fig. 9, b). The surface is prepared for selective fracture mechanism [15]. This effect, the change of the dislocation flow direction under external influences, can be used for the development of sensors.

Consider the equilibrium deformation region (Fig. 9, region II). In Fig. 9, a, the curve $E_{ac}(t)$ has a monotonically increasing and oscillating dependence in time. Each cycle of change in the value of stored energy $E_{ac}(t)$ corresponds to a cycle of change in strength characteristics $\rho(t)$ and change in wear intensity $I(t)$ (Fig. 9, b, region II). The latter is determined by the physics of the process of accumulation of dislocation density (clumping), their facilitated exit to the surface (Rebinder effect [35, 36]) with the formation of nanocrystalline (NC) structures on the surface under triboloading in accordance with the scheme shown in Fig. 10. The increase in dislocation density proceeds up to some critical value, and then a lobe fracture mechanism occurs, accompanied by a decrease in dislocation density. The variation of free energy (E_{free}) and wear (I) from time t at constant contact pressure is presented. The plateau in Fig. 10 corresponds to the formation of a stable dissipative structure. The increase in dislocation density proceeds up to some critical value, and then a lobe fracture mechanism occurs, accompanied by a decrease in dislocation density. The variation of free energy (E_{free}) and wear (I) from time t at constant contact pressure is presented. The plateau in Fig. 10 corresponds to the formation of a stable dissipative structure.

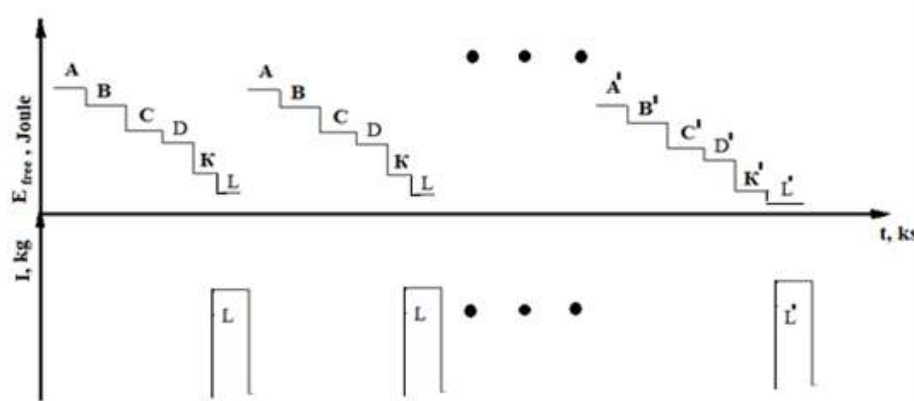


FIGURE 10: The generalized scheme of the kinetics of the free energy (E_{free}) and wear (I) changes of the metal surface layer for the equilibrium deformation region of the surface layer of metal. The structural formations: A - corresponds to nano- and submicrostructure; B - cellular or lamellar structure; C - slip bands; D - micropores; K - structure corresponding to transcrystalline and intercrystalline fracture of metal surface; L - structure corresponding to juvenile metal surface

Each formed dissipative structure will correspond to its own energy pumped into the system (ΔE_{free}). Each cycle of hardening and destruction of the surface layer (Fig. 9) corresponds to its structural changes A-K. The following structural formations are formed on the nickel surface under friction over time: A - corresponds to nano- and submicrostructure; B - cellular or lamellar structure; C - slip bands; D - micropores; K - structure corresponding to transcrystalline and intercrystalline destruction of the metal surface (Fig. 6); L - structure corresponding to juvenile metal surface. The latter is confirmed by analyzing the dislocation density on electron microscopic images of the nickel surface obtained at different times and corresponding to the wear intensity maxima [15]. The phenomenological model of lobe-layer fracture of the nickel surface layer under triboloading is described in [15].

Let us consider the region of nonequilibrium deformation (Fig. 9, b, region III). The amplitude of FMR line broadening (ΔN) for one cycle of change in strength characteristics of the nickel surface layer under triboloading is at least three times smaller than the amplitude of FMR line broadening (ΔN) for one cycle of change in strength characteristics in the region of equilibrium deformation (Fig. 9, b, region II). Since energy is directly proportional to the square of the amplitude, in the region of non-equilibrium deformation, the physical system reduces by an order of magnitude the energy cost between the upper and lower amplitude point of the hardening-strengthening cycle. With increasing strain energy accumulated in the nickel surface layer, the level of strain relaxation activation energy decreases so much that it acts as a regulator of both the number and size of defects and the way of their distribution and corporate interaction in accordance with the principle of energy profitability.

The formation of nanodoubles and nanodipoles of partial disclinations as carriers of noncrystallographic shift (Fig. 11, a, arrow, b and c), is also energetically advantageous, since the elastic field of interaction is localized between the elements of these structures rather than outside them, which determines a decrease in the value of the stored energy in the crystal lattice [34].

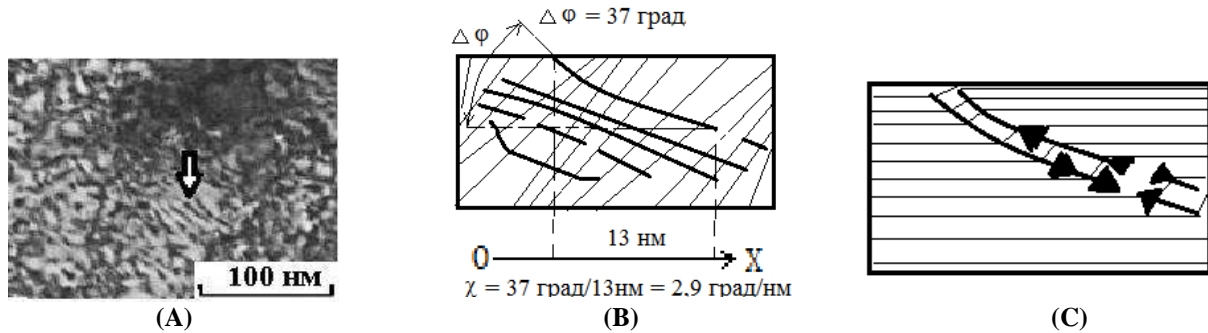


FIGURE 11: A) Propagation of nonlinear plastic distortion waves on nickel surface ($t = 133$ ks), B) schematic representation of nanobands (plastic distortion waves), C) schematic representation of nanobands as a set of partial disclinations

For materials made of copper, aluminum, nickel, etc., obtained by equal-channel angular pressing and severe plastic deformation on Bridgman anvils, for the curvature of the crystal structure, values of tens of $\text{deg}/\mu\text{m}$ are characteristic, and for NC materials - hundreds of $\text{deg}/\mu\text{m}$ [37–39]. The latter is fulfilled at high values of internal stresses, usually an order of magnitude lower than the elastic modulus of the materials. In our case, at long-term ($t > 108$ ks) triboloading of the nickel surface layer $\chi \approx 1 \text{ deg}/\text{nm}$, i.e., at least an order of magnitude higher. These results indicate an intensive fragmentation of the crystal lattice of the nickel surface layer under triboloading in the environment of surface-active substances, which promote an intensive exit of dislocations to the surface under the action of image forces and their splitting.

The fulfillment of the energy balance under triboloading will have the form [2]:

$$E_{\text{exter}} - E_{\text{ac}} = H + M, \quad (5)$$

Where H – is the entropy given by expression (5), M – is the energy determined by the mass of wear particles. Then it is obvious that the formation of NC and SMC structure at the points of contact of curves E_{exter} and E_{ac} is accompanied by entropy decrease (Fig. 9, a), since the area between these curves tends to zero. Table 1 summarizes the specific values of entropy and energy estimation, determined by the mass of worn particles, in the formation of a particular structure in the surface layer of nickel under triboloading. In the region of strongly nonequilibrium deformation, the formation of NC structures will also be accompanied by a decrease in entropy (Fig. 9, a, region III), but not as significant as for the region of equilibrium deformation (Fig. 9, a, region II). The entropy values in region III take both maximum and minimum values (Fig. 9, a, region III, arrows) at specific time values, which is consistent with the works [40, 41]. The entropy values in region III take both maximum and minimum values (Fig. 9, a, region III, arrows) at specific time values, which is consistent with the works [40, 41]. However, the entropy flux in time according to the principle of EP and PLA should take a minimum value. That is, the expression is fulfilled:

$$\int_{t_0}^{t_1} (E_{\text{exter}} - E_{\text{ac}}) dt = \int_{t_0}^{t_1} (H + M) dt \quad (6)$$

or taking into account the expression for entropy [42]:

$$H = \frac{\zeta (\nabla T)^2}{T^2} + \rho \frac{Z \Sigma}{T} \pm \frac{\rho}{T^2} ([\alpha, \Omega], \nabla T, t) \quad (7)$$

Where ζ - thermal conductivity, ρ - material density, Z - defect flux density, Σ - hydrostatic stress in the defect phase formation zone, parameters α and Ω characterize the energy flux through the surface. The first summand in expression (7) describes entropy production associated with heat generation. The second summand in expression (7) determines the work of the defects flux when they move in the stress field. The third summand in expression (7) describes the energy flow of the crystal mechanical field through the surface [42].

Thus, the value of the time integral in expression (8) takes the minimum value.

$$\int_{t_0}^{t_1} (H + M) dt = \int_{t_0}^{t_1} \left(\zeta \frac{(\nabla T)^2}{T^2} + \rho \frac{Z \Sigma}{T} \pm \frac{\rho([\alpha, \Omega], \nabla T, t)}{T^2} + M \right) dt \quad (8)$$

A truly physical system finds paths that require the least amount of work. Let us give some examples. In the region of equilibrium deformation (Fig. 9, region II), the time period of one cycle of hardening and de-hardening (≈ 18 ks) accompanied by flake fracture of a thin layer is 8 times longer than in the region of non-equilibrium deformation (≈ 2.3 ks) (Fig. 9, region III). Thus, in accordance with the PLA, the value of the work done per one hardening - de-hardening cycle decreases. At points A, B and C (Fig. 9, b) the dislocation density values reach maximum values, which corresponds to surface hardening and formation of NC states after these points selective fracture mechanism with exposure of juvenile surface occurs. However, the time interval between the onset of the selective fracture mechanism is: OA (from the moment of the beginning of triboloading) is ≈ 108 ks; AB is ≈ 34.105 ks, and between points BC is ≈ 20.845 ks. That is, the work or action done by the friction force at each subsequent time interval is less than at the previous one. The physical system has realized the path in accordance with the PLA and EP, at which the minimum work for the realization of the selective destruction mechanism is performed. The physical system finds a path of energy relaxation in accordance with the PLA, at which the minimum work is done to realize the selective destruction mechanism. The question of mathematical formulation of the external impact on the physical system is open and debatable. The value of the integral over time in expression (8) takes the minimum value (table 1), based on the fulfillment of the energy balance (6).

TABLE 1

QUANTIFICATION OF ENTROPY AND ENERGY, DETERMINED BY THE MASS OF WORN PARTICLES, IN THE FORMATION OF A PARTICULAR STRUCTURE IN THE SURFACE LAYER OF NICKEL UNDER TRIBOLOADING

Type of structure	t, 10 ³ s	H+M, entropy plus energy determined by the mass of wear particles, 10 ⁶ J·s
NC structures	0.9	0.097200
Slip strips	6.5	2.514270
Fragmented NC and SMC structures	108	57.828210
Loose and porous surface layer	160	120.380200

Execution of the energy balance (5) taking into account the expression for the dislocation energy shows that in the conditions of strongly nonequilibrium system (Fig. 9, region III), the number of point defects (atom-vacancy states) increases by orders of magnitude (3-5), i.e. their role sharply increases in the description of such systems.

Thus, the ways to describe the external influence on a system (physical, chemical, biological [2]) can be different: the principle of least action or energy profitability, but the result is the same (Fig. 12).

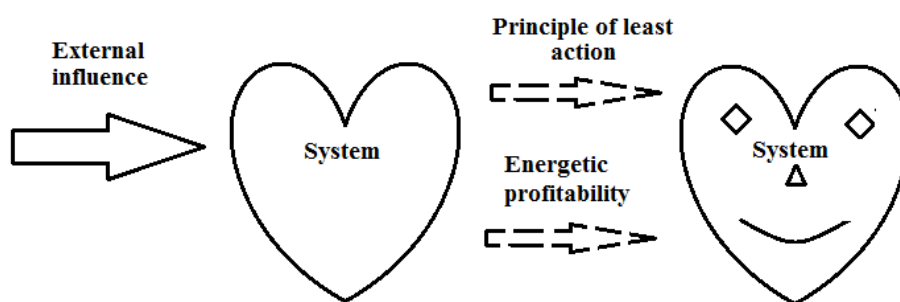


FIGURE 12: The scheme of external influence on the system (physical, chemical, biological) and its description by the method of energetic profitability and the principle of least action

It is established that the kinetics of the structure formation and evolution of the metal interface surface under external influences proceeds in accordance with the following provisions of thermodynamics:

- To each steady state of the metal interface will correspond its own structure with a certain value of free energy and, accordingly, with types of its redistribution between the elements of the boundaries and within the structural formation;

- If the action of load-velocity parameters or external influence exceeds some critical value of the energy supplied to the system, then it passes to a new structural state in accordance with EP and PLA and characterized by a lower value of free energy;
- The intensity of external impact determines the duration of the cycle of change in strength characteristics, the amount of strain energy accumulation and the degree of fragmentation of the surface layer of metals and, accordingly, the gradient of disorientation between structural elements, where the number, density, and their interaction (nano-, submicro-, slip bands, pores, etc.) determine the dominant role of one or another scale level of plastic deformation at a given moment of time of the kinetics of structure formation and the mechanism of its destruction in accordance with EP and PLA.

IV. CONCLUSION

The physical essence of the processes: heat conduction, diffusion, mass transfer, hardening, amorphization, fracture, etc., occurring at contact localized interaction of metal surfaces, and the result is the same and does not depend on the way of its description. The work done or the response of a physical system (material) is commensurate with the magnitude of the external influence. It does not matter what mathematical approach we use (calculus of variations to describe IPA or differential equations based on Newton's laws, continuum physics, kinetics of physical and chemical processes) to describe physical processes in a solid body.

The main thing is the result in the form of minimum energy costs for the formation, evolution and destruction of a structure with certain properties. However, the PLA (Hamilton's principle) is a more basic and fundamental principle, as it describes equilibrium and non-equilibrium processes than the minimum or maximum of entropy production for describing non-equilibrium processes. In addition, the use of PLA implies, based on the properties of space and time symmetry, the search and establishment of invariants, which does not follow from the principle of energetic favorability. The latter is most important as it has practical value in the study and evolution of the properties of emerging structures. Analysis of literature data and the existence of invariants, for example, in chemistry (D.I. Mendeleev's table, the law of conservation of mass during chemical reactions), biology (Mendel's second law), nuclear and quantum physics (conservation laws, etc.) determine the fundamentality and universality of the use of PLA and energy benefits for processes occurring in the space-time continuum. The issue of the inverse effect of material properties on the properties of the space-time continuum is debatable and open to further research.

REFERENCES

- [1] "Problems of Wear of Solid Bodies in the Aspect of Mechanics, A. Y. Ishlinsky et al, Friction and wear, 1986, Vol. 7, № 4, p. 581-591.
- [2] Korotkevich, S.V. Properties of Symmetry of Space and Time, Hamilton's Principle and the Invariants / S.V. Korotkevich // International Journal of Engineering Research and Science. – 2024. – Vol. 10, issue 8. – P. 21–30.
- [3] Feynman R., Leighton R., Sands M. Feynman Lectures on Physics. – Vol. 3: Radiation. Waves. Quanta. – M. : World. – 1965. – 238 p.
- [4] V. D. Kuznetsov, "Solid State Physics" : in 4 vol., Tomsk : Krasnaya Znamya, 1937-1949, Vol. 4: "Materials on Physics of External Friction, Wear and Internal Friction of Solids", 1947, 543 p.
- [5] Kragelskii, I. V. Fundamentals of friction and wear calculations / I. V. Kragelskii, M. N. Dobychin, V. S. Komalov. - M. : Mashinostroenie, 1977. - 525 p.
- [6] Marchenko, E. A. About the nature of destruction of metal surface at friction / E. A. Marchenko. - Moscow : Nauka, 1979. - 118 p.
- [7] The role of dislocations in hardening and fracture of metals / V. S. Ivanova [et al]. - Moscow : Nauka, 1965. - 180 p.
- [8] Suh, N. P. An Overview of the Delamination Theory of Wear / N. P. Suh // Wear. – 1977. – Vol. 44, № 1. – P. 1–16.
- [9] Valiev, R. Z. Volumetric nanostructured metallic materials: preparation, structure and properties : [monograph] / R. Z. Valiev, I. V. Aleksandrov. - Moscow : Akademkniga, 2007. - 397 p.
- [10] Winkelmann, K. Global Perspectives of Nanoscience and Engineering Education / K. Winkelmann, B. Bhushan. – Springer, 2016, XII. – 400 p.
- [11] Korotkevich, S. The properties of strongly nonequilibrium surface layer of nickel / S. Korotkevich, Ya. Kavaliou, A. Kupo // International independent scientific journal. – 2024. – №. 67. – P. 43–52.
- [12] Korotkevich, S.V. Scale levels of deformation and destruction of the nickel surface layer under localized external impact / C.B. Korotkevich, S.V. Panin. Korotkevich, S.V. Panin // Actual Problems of Strength / A.V. Alifanov [et al.], ed. by V.V. Rubanik. Rubanik. - Mn.: Izd. "IVTs of the Ministry of Finance", 2022, 540 p.
- [13] Fundamental role of crystal structure curvature in plasticity and strength of solids / V. E. Panin [et al.] // Phys. Mesomechanics. - 2014. - T. 17, № 6. - P. 7-18.
- [14] Multiscaling of Lattice Curvature on Friction Surfaces of Metallic Materials as a Basic of Their Wear Mechanism / V.E. Panin, V.G. Pinchuk, S.V. Korotkevich, S.V. Panin // Physical Mesomechanics. – 2017. – Vol. 20, № 1. – P. 69 – 77.
- [15] Pinchuk, V.G. Kinetics of hardening and fracture of metal surface under friction / V.G. Pinchuk, S.V. Korotkevich; Ministry of Education of the Republic of Belarus; F. Skaryna State University; reviewers: Dr. D.G. Lin; Dr. N.V. Gruntovich. - Saarbrücken: Lambert Academic Publishing, 2014. - 181 p.
- [16] Physical Encyclopedia : in 10 vol. / edited by A. M. Prokhorov. - Moscow : Big Russian Encyclopedia, 1998. - Vol. 5. - 691 p.

- [17] Baryakhtar, V. G. Influence of dislocations on the line width of homogeneous ferro- and antiferromagnetic resonances / V. G. Baryakhtar, M. A. Savchenko, V. V. Tarasenko // *Jurn. of Experim. and Theoretical Physics*. - 1968. - Vol. 54, issue 5. - P. 1603-1612.
- [18] Bulatov, A. S. Dependence of the FMR line width on the dislocation density in nickel / A. S. Bulatov, V. G. Pinchuk, M. B. Lazareva // *Physics of Metals and Metallurgy*. - 1972. - Vol. 34, issue 5. - P. 1066-1069.
- [19] Morkowski, I. Broadening of Ferromagnetic Resonance Line of Dislocation / I. Morkowski // *Act Phys. Polonica*. - 1969. - Vol. 36, № 35. - P. 565-583.
- [20] Marchenko, E. A. About the nature of destruction of metal surface at friction / E. A. Marchenko. - Moscow : Nauka, 1979. - 118 p.
- [21] Yurkova, A. I. Structure and mechanical properties of iron after surface intense plastic deformation by friction with simultaneous nitrogen saturation. Part I, Features of structure formation / A. I. Yurkova, Y. V. Milman, A. V. Byakova // *Deformation and fracture of materials*. - 2011. - № 2. - P. 1-8.
- [22] Yurkova, A. I. Structure and mechanical properties of iron after surface intensive plastic deformation by friction with simultaneous nitrogen saturation. Part II, Mechanical properties of nano- and submicrocrystalline iron saturated with nitrogen during deformation / A. I. Yurkova, Y. V. Milman, A. V. Byakova // *Deformation and fracture of materials*. - 2011. - № 3. - P. 1-8.
- [23] Tarasov, S. Yu. Effects of Friction on Subsurface Layer Microstructure in Austenitic and Martensitic Steels / S. Yu. Tarasov, A. V. Kolubaev // *Wear*. - 1999. - Vol. 231, № 2. - P. 228-234.
- [24] Orowan, B. Dislocations in Metals / B. Orowan // *AIME*. - 1954. № 1. - P. 69.
- [25] L. D. Landau, E. M. Lifshits, "Theoretical Physics in Ten Volumes. T. 1 Mechanics", Moscow: Nauka, 1988. - 215 p.
- [26] C. Kittel, *Quantum Theory of Solids*, M.: Nauka, Gl. ed. Phys.-Mat. Litt., 1967. - 492 p.
- [27] Antoni, K.-H. Thermodynamics of the friction process and Lagrangian formalism: a contribution to the mesoscopic approach in the theory of plasticity / K.-H. Antoni // *Physical Mechomechanics*. - 2001. - T. 4, № 4. - P. 33-46.
- [28] L. D. Landau, E. M. Lifshits, "Theoretical Physics : in 10 vol.", Moscow : Main Editorial Board of Physical and Mathematical Literature, 1988, Vol. 2 : "Field Theory", 512 p.
- [29] Cottrell, A. Theory of dislocations / A. Cottrell ; edited by A. L. Roitburd. - M. : Mir, 1969. - 95 p.
- [30] R. Honiccombe, "Plastic Deformation of Metals", R. Honiccombe ; edited by B. Y. Lyubov, Moscow : Mir, 1972, 408 p.
- [31] Orlov, A. N. Introduction to the theory of defects in crystals : [textbook for universities on specialty "Physics of Metals"] / A. N. Orlov. - Moscow: Vysh. shk., 1983. - 144 p.
- [32] Moser, B. Cyclic Strain Hardening of Nanocrystalline Nickel / B. Moser, T. Hanlon, K. S. Kumar // *Scripta Materialia*. - 2006. - Vol. 54, № 6. - P. 1151-1155.
- [33] Holste, C. Cyclic Plasticity of Nickel, from Single Crystals to Submicrocrystalline Polycrystals / C. Holste // *Philos. Mag.* - 2004. - Vol. 84, № 3-5. - P. 299-315.
- [34] Nanodipoles of partial disclinations as carriers of noncrystallographic shift and reorientation of the crystal lattice in nickel and vanadium nanocrystals / A. N. Tyumentsev [et al.] // *Izv. of Higher Educational Institutions. Physics*. - 2010. - Vol. 53, № 12. - P. 67-76.
- [35] Rebinder, P. A. Surface phenomena in solids in the processes of their deformation and fracture / P. A. Rebinder, E. D. Shchukin // *Uspekhi fiz. nauki*. - 1972. - Vol. 108, issue 1. - P. 3-42. 3-42.
- [36] Shchukin, E. D. Influence of the active medium on the mechanical stability and damage resistance of a solid body surface / E. D. Shchukin // *Vestnik. Mosk. un-ta. Series 2, Chemistry*. - 2012. - T. 53, № 1. - C. 50-72.
- [37] Tyumentsev, A.N., Ditenberg, I.A. Structural States with High Curvature of the Crystal Lattice in Submicrocrystalline and Nanocrystalline Metallic Materials, *Izvestiya vuzov, Physics*, 2011, vol. 54, no. 9. - pp. 26-36.
- [38] Tyumentsev, A.N. and [et al.], Evolution of the Curvature of the Crystal Lattice in Metallic Materials at the Meso- and Nanostructured Levels of Plastic Deformation, *Physical mesomechanics*, 2013, vol. 16, no. 3, pp. 61-77.
- [39] Kozlov, E.V. and [et al.], Influence of Equal-channel Angular Pressing on the Structure and Yield Stress of 10G2FT Steel, *Deformation and destruction of materials*, 2016, no. 3, pp. 10-14.
- [40] Nicolis, G. Self-organization in nonequilibrium processes / G. Nicolis, N. Prigozhin. - M. : Mir, 1977. - 512 p.
- [41] Martyushev, L.M. Principle of maximum entropy production in physics and related fields / L.M. Martyushev, V.D. Seleznyov. - Ekaterinburg: GOU VPO UGTU, 2006. - 83 p.
- [42] Panin, V. E. Deformable solid body as a nonlinear hierarchical organized system / V. E. Panin, V. E. Egorushkin // *Phys. Mesomechanics*. - 2011. - T. 14, № 3. - P. 7-26.

Pan-genome Sequence Alignment Algorithm Research

LuFang Yu

School of Big Data Statistics, Guizhou University of Finance and Economics, Guiyang, Guizhou Province

Received: 04 September 2025/ Revised: 12 September 2025/ Accepted: 21 September 2025/ Published: 30-09-2025

Copyright @ 2025 International Journal of Engineering Research and Science

This is an Open-Access article distributed under the terms of the Creative Commons Attribution Non-Commercial License (<https://creativecommons.org/licenses/by-nc/4.0>) which permits unrestricted

Non-commercial use, distribution, and reproduction in any medium, provided the original work is properly cited.

Abstract— With the rapid development of sequence alignment technologies, their role in responding to public health emergencies and epidemic prevention has become increasingly prominent. Compared to traditional linear reference sequences, the pan-genome effectively reduces reference bias and misalignment. However, when facing long reference sequences with abundant repetitive regions, candidate positions may proliferate, thereby compromising alignment efficiency and accuracy. This paper proposes a novel alignment algorithm that integrates elastic degenerate strings with the longest common substring strategy. Single nucleotide polymorphisms (SNPs) are linearly encoded using elastic degenerate symbols, while minimizer indexing is combined with a longest common substring interval-based seed filtering strategy to effectively reduce candidate positions. Experimental validation on simulated datasets demonstrates that the proposed method significantly improves both recall and precision rates, while also achieving high accuracy in fragment localization. Further experiments on real datasets reveal that this method outperforms existing mainstream alignment tools in terms of alignment sensitivity, indicating that the longest common substring-based filtering strategy is well suited for complex genomic regions. Overall, this approach provides an alternative technical pathway for enhancing the accuracy of pan-genome sequence alignment and offers a feasible algorithmic framework for subsequent research on pan-genome alignment and viral mutation analysis.

Keywords— Sequence Alignment; Seed-and-Extend; Elastic Degenerate String; Longest Common Substring.

I. INTRODUCTION

At the end of 2019, the outbreak of pneumonia caused by the novel coronavirus (SARS-CoV-2) rapidly spread worldwide, leading to severe economic losses and significant healthcare burdens[1][2]. Existing studies have identified single-nucleotide polymorphism (SNP) sites and related genes potentially associated with pneumonia symptoms, and some mutation sites have even been shown to influence vaccine efficacy, thereby posing a potential risk of further enhancing the transmissibility of COVID-19[3][4]. When dealing with highly variable viruses such as SARS-CoV-2, researchers must rapidly collect a large number of samples from infected individuals. Using high-throughput sequencing and sequence alignment technologies, they are able to analyze the pathogenic mechanisms, transmission routes, and evolutionary relationships of the virus in depth. These studies provide crucial scientific evidence for vaccine development and epidemic control. However, performing pairwise sequence alignment between short reads and long reference genomes presents substantial computational challenges, requiring not only algorithmic efficiency but also accuracy in short-read alignment. Therefore, improving the efficiency and accuracy of existing sequence alignment algorithms is of significant research value and practical importance for advancing viral genomics research and epidemic surveillance.

With the advancement of sequencing technologies and in consideration of the length and complexity of genomic sequences, an increasing number of alignment algorithms construct auxiliary index structures for reference genomes to accelerate the alignment process. Based on the type of index used, alignment algorithms can generally be divided into two categories: suffix-based indexing and hash-based indexing. Suffix-based methods typically employ suffix arrays[5], Burrows-Wheeler Transform (BWT) [6], and FM-index[7] for alignment, and are suitable for large-scale genomic data such as the human reference genome. Although such methods do not require additional positioning operations, they consume substantial memory resources. For relatively short reference genomes such as those of viruses, hash-based indexing is often preferred for rapid sequence analysis

in order to obtain more accurate alignment results. In this process, however, the seed selection strategy plays a pivotal role in enhancing both the efficiency and accuracy of sequence alignment algorithms.

Regarding seed selection strategies, numerous studies have proposed effective improvements. Roberts et al. introduced the concept of the minimizer[8], which selects the k-mer with the smallest hash value within a consecutive window of seeds as the alignment seed. This approach significantly reduces the storage space required for indexing and has led to the development of alignment tools such as Giraffe[9] and GraphAligner[10]. While this method greatly reduces memory usage and computational overhead in alignment, the abundance of repetitive sequences in long reference genomes often leads to false positives caused by high-frequency minimizers. To address this, the weighted-minimizer approach[11] was proposed, assigning weights to minimizers according to their frequency in the reference genome, thereby prioritizing seeds with higher weights for read placement. However, relying solely on single-seed extension can result in locally optimal alignments, necessitating consideration of relationships among multiple seeds. By employing collinear chaining[12] in the intermediate seed extension step, seeds that satisfy collinearity constraints are selected, producing higher-quality seed sets and improving alignment accuracy. One of the most widely used pairwise sequence alignment algorithms, Minimap2[13], adopts this strategy, substantially enhancing long-read alignment efficiency. Similarly, the graph-based alignment tool GED-MAP[14] leverages collinear chaining to accelerate candidate position filtering, achieving both faster alignment and reduced memory usage. For short reads, however, directly computing collinear chains does not provide significant alignment optimization benefits and can even increase computational costs during the filtering phase. Ding Shengnan et al. proposed a region-based coarse-grained filtering method, which accelerates alignment using sliding window indexing tables and filtering formulas. Nevertheless, this method faces challenges of computational and memory consumption when applied to large-scale datasets[15]. Song Siyi et al. introduced a low-frequency seed voting strategy to accelerate alignment, but its scalability is limited and requires improvements in indexing structures to accommodate large genome datasets[16]. Gao Jia and Xu Yun further combined minimizer-based seeding strategies to reduce false-positive alignments, though this approach may still encounter mismatches in repetitive regions[17]. While these methods have made progress in enhancing alignment efficiency, they continue to face limitations when applied to pan-genomes or large-scale complex datasets.

To address the above issues, this paper proposes a semi-global alignment algorithm based on longest common substring intervals. Specifically, the improvements of this study focus on two aspects: first, by employing elastic degenerate symbols, SNP variations are incorporated into the reference genome, providing a concise linear representation of the pan-genome. Second, given the critical role of the longest common substring in biological sequences, this study introduces a seed filtering strategy based on longest common substring intervals.

II. BASIC CONCEPTS AND METHODS

2.1 Basic Concepts:

In the analysis of high-throughput sequencing data, particularly the massive short fragments generated by second-generation sequencing technologies, the limited read length often carries insufficient biological information to independently reveal their functions or significance. Therefore, it is necessary to align these short reads against a reference genome to determine their potential genomic locations, a process referred to as sequence alignment[18]. For sequence alignment problems, Hamming distance and edit distance are two commonly used similarity measures.

Hamming distance[19] refers to the number of single-character substitution operations required to transform one string into another. Edit distance[20], on the other hand, denotes the minimum number of edit operations needed to convert one string into another, where the allowed edit operations include substitution, insertion, and deletion. Considering that sequencing errors in reads often involve substitutions, insertions, and deletions, and that genetic variation across different samples also introduces insertions and deletions, edit distance is generally a more realistic measure.

With the advancement of sequence analysis technologies, using a single reference genome in alignment often fails to adequately capture population-specific variations, thereby increasing the difficulty of identifying disease-related genetic associations. To address this challenge, the concept of the pangenome was introduced in the context of studying the dynamic nature of bacterial genomes. A pangenome refers to the collection of multiple genomic sequences from the same species[21]. In recent years, an

increasing number of studies have shifted toward graph-based pangenomes, which help mitigate reference bias and misalignment issues. Specifically, a pangenome graph is a graph representation of the pangenome, where each node corresponds to a nucleotide sequence, and each path through the graph represents a genotype, as illustrated in Figure 1.

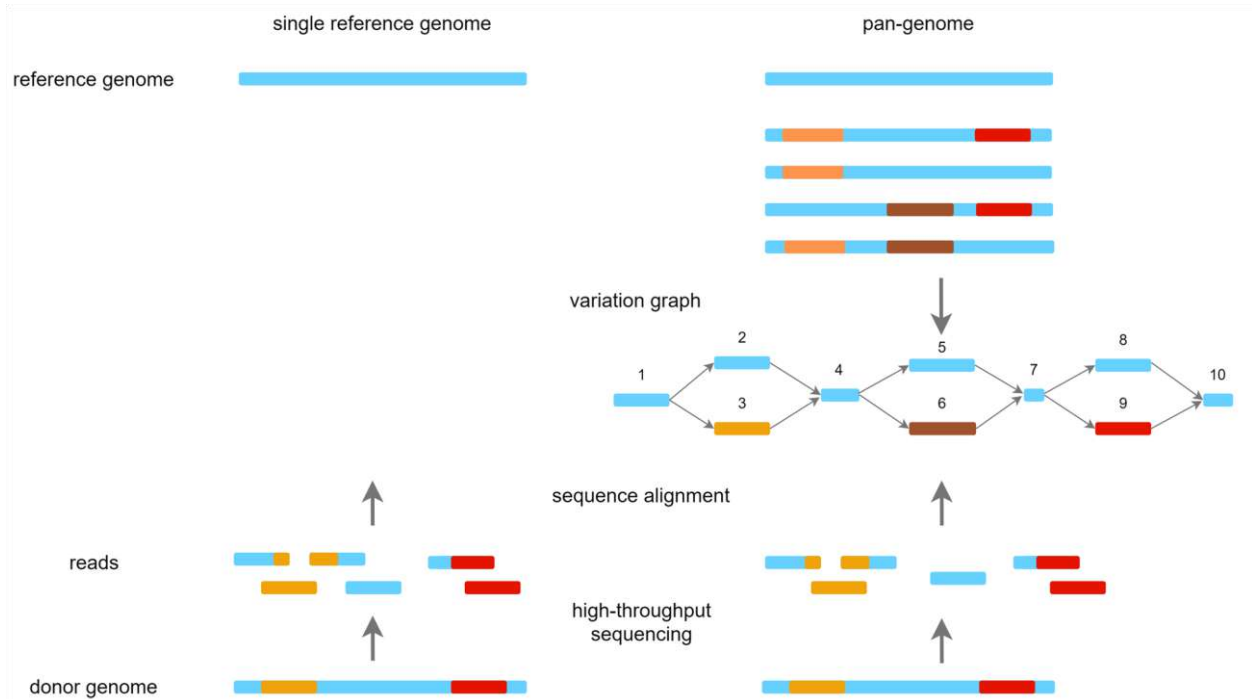


FIGURE 1: Comparison between a single reference genome and a pangenome

Figure 1 illustrates alignment scenarios based on different reference genomes. A pangenome compresses the linear sequences of a population into a variation graph. In this representation, nodes correspond to specific nucleotide sequences; for instance, nodes 1, 4, 7, and 10 represent fragments shared across all genomes, while variant fragments form “bubble” structures within the graph. A path constructed from a series of adjacent nodes represents a possible biological sequence. Compared to the traditional linear reference genome, this approach not only maximizes sequence similarity to reduce redundant storage but also provides a more intuitive and effective way to represent genetic variation within a population.

2.2 Methods:

2.2.1 Elastic-Degenerate Strings:

Having established the concept of the pangenome, it is clear that while graph representations can capture a broader range of genetic variation, they also introduce additional complexity. Functions that are relatively trivial on linear genomes often become more challenging on genome graphs. To represent SNP variations concisely on a graph, the Elastic-Degenerate Strings (EDS) method[22] is adopted. The following provides detailed definitions and illustrates how SNP variations can be expressed.

Definition 1 Elastic-Degenerate Symbol (ξ):

Given the character set $\Sigma = \{A, C, G, T\}$, where ε denotes the empty character, and Σ^* represents the set of all strings over Σ including ε . An elastic-degenerate symbol ξ is defined as a finite, non-empty set of strings ($\xi \in \Sigma^*$ and $\xi \neq \emptyset$), which can be expressed as $\xi = [E_1 | \dots | E_m]$, where each E_i is referred to as an alternative string.

Definition 2 Elastic-Degenerate String (\hat{S}):

An EDS over Σ is a string consisting of a sequence of elastic-degenerate symbols, i.e., $\hat{S} = \xi_1 \dots \xi_n$.

Definition 3 Possibility Set (\mathfrak{R}): A string Y matches an elastic-degenerate string \hat{S} if and only if $Y \in \mathfrak{R}$, where \mathfrak{R} is the set of all possible strings generated from \hat{S} . In other words, by substituting each elastic-degenerate symbol with one of its alternative strings, a new string can be obtained.

To better illustrate the above definitions, consider a pangenome represented by the elastic-degenerate string $\hat{P} = \text{CG}[\text{T}|\text{G}]\text{GCCA}[\text{C}|\text{T}]\text{AT}$. Here, $[\text{T}|\text{G}]$ denotes an elastic-degenerate symbol at position 3, which can be substituted by either T or G; similarly, $[\text{C}|\text{T}]$ represents another substitution at the corresponding position.

2.2.2 Seed-and-Extend Method:

In sequence alignment algorithms, the Seed-and-Extend strategy[23] is widely employed. Its primary purpose is to narrow the alignment search space from the entire reference genome to a subset of candidate regions by means of seed localization. This method generally consists of three steps:

Step 1. Extract fixed-length substrings (k-mers) from the read. These substrings are referred to as seeds.

Step 2. Perform rapid seed lookup using an index. With a pre-built reference genome index, the positions of the read seeds in the genome can be efficiently queried. Candidate positions of poor quality are then filtered out according to specific strategies.

Step 3. Map the seed positions onto the reference genome and extend them in combination with the read length to generate candidate regions, which are then aligned with the read at base-level resolution. The alignment quality is assessed using dynamic programming algorithms, producing the final matching location. The overall workflow of the Seed-and-Extend method is illustrated in Figure 2.

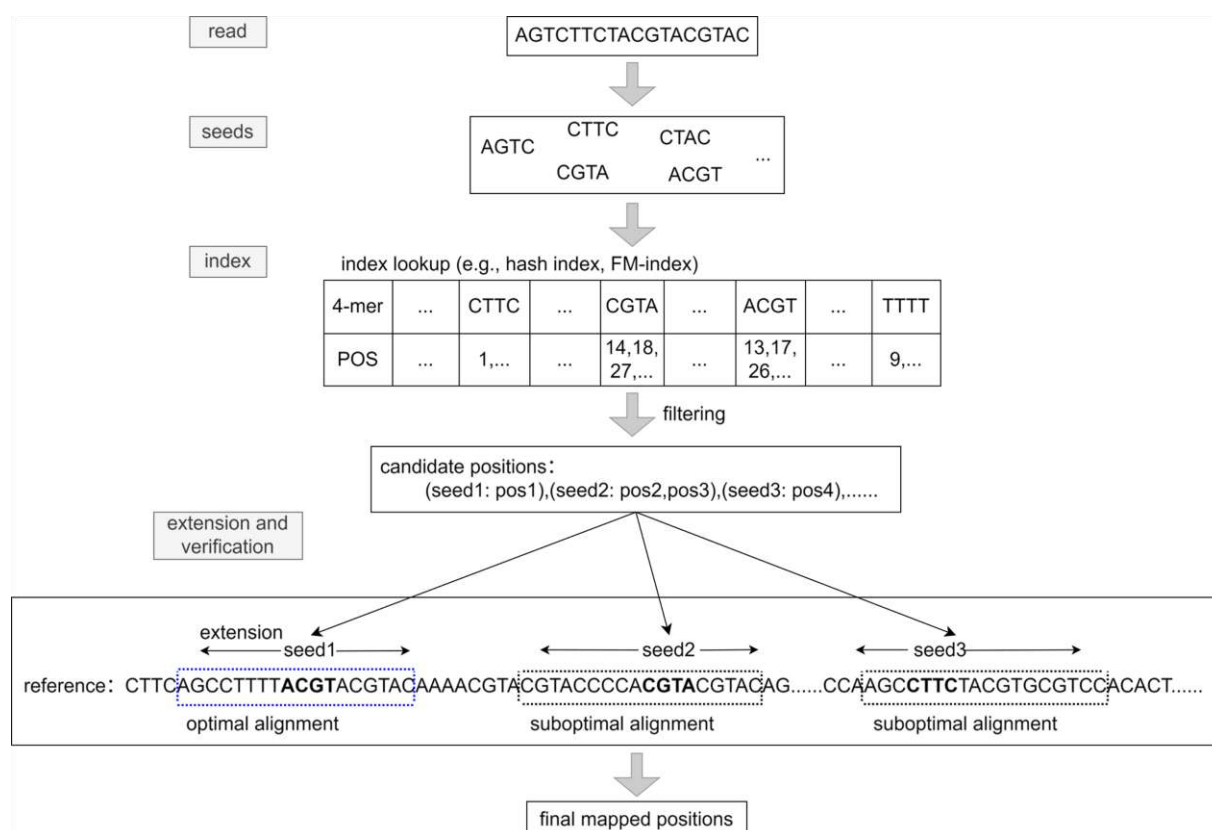


FIGURE 2: Seed-and-Extend method

As shown in Figure 2, the seeds generated from a read can result in numerous redundant and erroneous candidate positions, which must be filtered out. Therefore, while maintaining alignment sensitivity, it is essential to adopt effective filtering strategies for low-quality seeds in order to reduce the computational burden during the verification stage and to obtain the final alignment positions efficiently.

2.2.3 Longest Common Substring:

The Longest Common Substring (LCSstr)[24] refers to the longest identical substring that appears contiguously in both strings. In contrast, the Longest Common Subsequence (LCS)[25] is the longest sequence that appears in two or more sequences, with elements occurring in the same relative order in all sequences but not necessarily contiguously. Their applications differ: LCSstr

is suitable for scenarios requiring strictly contiguous matches (e.g., genomic sequence alignment), whereas LCS is applicable to tasks where order preservation is required but interruptions are allowed (e.g., text difference comparison).

For two given strings S_1 and S_2 , the LCSstr can be computed using a dynamic programming algorithm. A two-dimensional array $c[i, j]$ is defined, where $c[i, j]$ denotes the length of the LCSstr ending at $S_1[i]$ and $S_2[j]$. The values of $c[i, j]$ can be computed using recurrence relation (1).

$$c[i, j] = \begin{cases} 0, & i = 0 \text{ or } j = 0 \\ c(i-1, j-1) + 1, & \text{if } S_1[i] = S_2[j] \\ 0, & \text{else} \end{cases} \quad (1)$$

By filling the entire array according to this recurrence, the maximum value in the array represents the length of the LCSstr between S_1 and S_2 . For example, given the read $r = \text{GTGCCATT}$ and the pangenome $\hat{P} = \text{CG[T|G]GCCA[C|T]AT}$, the longest common substring is “GCCA”. To enable subsequent seed filtering, it is necessary to record the starting and ending indices of all maximum LCSstr occurrences in both the read r and the pangenome \hat{P} , denoted as $[r_i, r_j]$ and $[\hat{P}_i, \hat{P}_j]$, respectively. In this case, $[r_i, r_j] = [2, 5]$ and $[\hat{P}_i, \hat{P}_j] = [7, 10]$.

III. ALIGNMENT ALGORITHM DESIGN

The sequence alignment algorithm proposed in this study is primarily based on the Seed-and-Extend paradigm, and the entire alignment process can be divided into three major stages: (1) Index construction; (2) Seed selection; (3) Extension and verification. The specific workflow is illustrated in Figure 3.

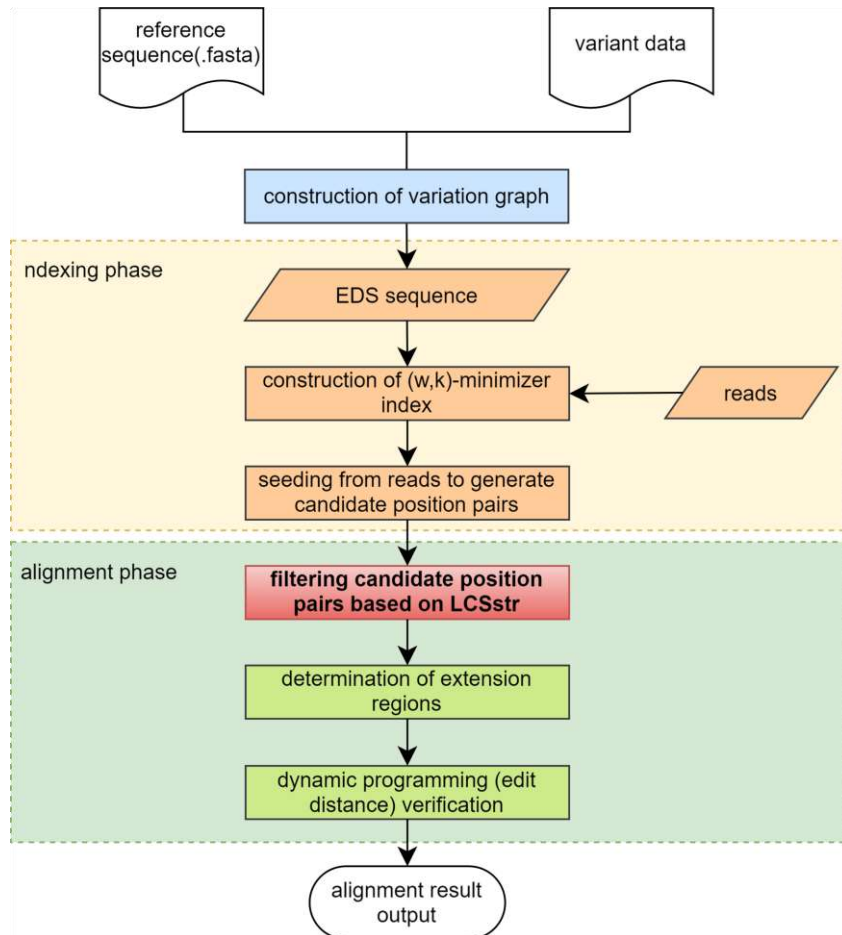


FIGURE 3: Workflow of the sequence alignment algorithm

In the indexing stage, minimizer indexes are constructed for both the pangenome \hat{P} and the read r , and stored in hash tables. In the seed selection stage, the positions of seeds from the read are queried against the pangenome, forming a series of position pairs. These numerous candidate positions are then filtered using the LCSstr ranges to obtain the candidate seeds. In the

alignment stage, the candidate regions are determined by combining seed positions with read length extension, followed by base-level verification using dynamic programming to produce the final alignment results. The sections marked in red in Figure 3 highlight the main improvements proposed in this paper. The following subsections provide a detailed description of these three stages.

3.1 Index Construction:

To further reduce memory overhead during the sequence alignment process, this study employs the (w, k) -minimizer method[8]. The core idea is to select, from every consecutive set of w k -mers (each of length k), the lexicographically smallest k -mer as the seed, which is referred to as the minimizer. The sequence formed by these consecutive w k -mers is called a window, and its length is defined as $win = k + w - 1$. In this paper, lexicographic order is adopted as the sorting rule. Figure 4 illustrates the $(4, 3)$ -minimizer computation for the example read $r = \text{GTGCCATT}$. Each row represents a window of length 6, with the bolded 3-mer indicating the minimizer for that window.

	0	1	2	3	4	5	6	7
read:	G	T	G	C	C	A	T	T
window:	G	T	G	C	C	A		
		T	G	C	C	A	T	
			G	C	C	A	T	T

FIGURE 4: Index table construction for the read

When constructing the minimizer index table for the pangenome \hat{P} special syntactic symbols (“[”, “[”, “]”) must be considered. Specifically, each alternative option within an elastic-degenerate symbol needs to be evaluated, while k-mers overlapping with syntactic symbols are excluded. If consecutive windows produce the same minimizer, only the positional information of that minimizer is added to the index table. Figure 5 shows the process of generating the index table for the pangenome $\hat{P} = \text{CG}[\text{T}|\text{G}]\text{GCCA}[\text{C}|\text{T}]\text{AT}$.

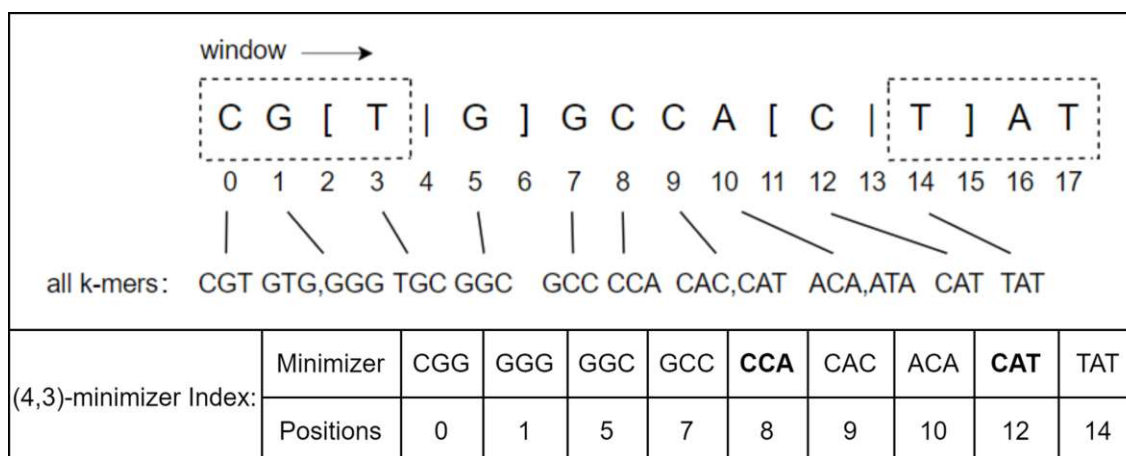


FIGURE 5: Minimizer index table construction for the pangenome

As can be seen, in real reference genomes, due to long sequence lengths and abundant repetitive regions, the sliding window technique can effectively reduce memory requirements. This not only preserves alignment sensitivity but also provides a more efficient computational foundation for downstream sequence analysis and alignment tasks. However, it is important to note that the construction of minimizer index tables involves a trade-off between sensitivity and speed. Therefore, appropriate values of w and k must be carefully chosen. Algorithm 1 presents the pseudocode for computing the minimizer set of a pangenome using the sliding window approach.

Algorithm 1: Minimizer Index Construction Algorithm for the Pangenome**Input:** pangenome \hat{P} , window length w , substring length k **Output:** index table $index$

```

1.  initialization:  $L = \text{len}(\hat{P})$ ;  $R_s \leftarrow []$ ;  $R_i \leftarrow [0] * L$ ;  $i \leftarrow 0$ ;  $index \leftarrow \{\}$ ;  $start \leftarrow 0$ 
2.  while  $i < L$  do // construct the compressed sequence  $R_s$  and the index mapping  $R_i$ 
3.    if  $P[i] \neq "["$  then
4.       $R_i[i] \leftarrow \text{len}(R_s)$ ;  $R_s.append(P[i])$ ;  $i \leftarrow i + 1$ 
5.    else
6.      treat the ED symbol as an atomic unit and update the index into  $R_i$ 
7.      append the lexicographically smallest character within the ED symbol to  $R_s$ 
8.    while  $start + w \leq L$  do
9.       $end \leftarrow start + w - 1$ 
10.      $A \leftarrow []$ 
11.     for  $j \leftarrow (start, end + 1)$ 
12.       if  $P[j] \in \{ '[', '|', ']' \}$  continue
13.        $idx \leftarrow R_i[j]$ 
14.       if  $idx + k > \text{len}(R_s)$  continue
15.        $r \leftarrow P[j] + R_s[idx + 1 : idx + k]$ 
16.        $A \leftarrow A \cup \{(r, j)\}$ 
17.     if  $A = \emptyset$  continue
18.      $r' \leftarrow \text{minLex}(A)$ 
19.     for  $(r', p) \in A$ 
20.        $index[r'].appendUnique(p)$ 
21.   return  $index$ 

```

3.2 Seed Selection:

Considering that during biological variation and evolution, certain identical gene sequences are retained, these regions are referred to as conserved regions[26]. Conserved regions generally play important physiological or genetic roles. The Longest Common Substring (LCSstr) can reflect a degree of conservation, making it an important reference in alignment. Therefore, this study employs the LCSstr interval to filter seeds.

By querying the positions of seeds from the read in the reference genome index table, a series of position pairs $(P_r, P_{\hat{P}})$ can be obtained. These position pairs $(P_{r_n}, P_{\hat{P}_n})$ are then filtered using the LCSstr interval. If a position pair satisfies Formula (2), it is retained as a candidate position pair (i^*, j^*) for subsequent extension and verification. In this formula, r_i and r_j denote the start and end indices of the LCSstr within the read r , while \hat{P}_i and \hat{P}_j denote the start and end indices of the LCSstr within the pangenome \hat{P} .

$$r_i \leq P_{r_n} \leq r_j \ \& \ \hat{P}_i \leq P_{\hat{P}_n} \leq \hat{P}_j \quad (2)$$

If no candidate positions remain after LCSstr-based filtering, the relationships among seeds are further considered by applying the colinear chaining method[12] to filter the initially formed position pairs. The colinearity rule specifies that two position pairs (x, y) and (x', y') are colinear if and only if $x < x'$ and $y < y'$, denoted as $(x, y) < (x', y')$. The score of a position pair (x, y) is defined as the length of the maximum colinear chain ending at (x, y) . Finally, the chain with the highest score is used for base-level alignment. If the resulting alignment is unsatisfactory, the position pair from the chain with the second-highest score is selected for alignment.

In the example above, querying the seeds from Figure 4 in the pangenome index table yields candidate seeds, as indicated by the bolded minimizers in Figure 5. By combining their positions in r and \hat{P} , the position pairs (3,8) and (4,12) are obtained. Finally, by computing the interval of the longest common substring between the read and the pangenome, the final candidate position retained for alignment is (3,8). Algorithm 2 provides the pseudocode for the seed filtering algorithm based on the LCSstr interval.

Algorithm 2: Seed Filtering Algorithm Based on Longest Common Substring Intervals

Input: pangenome \hat{P} , its index M_idx , read set R , and its index R_idx , seed score s

Output: candidate seed set $filt$

```

1.  initialization:  $pos \leftarrow []; filt \leftarrow []; s \leftarrow []$ 
2.  for  $r \in R$  do
3.    for  $(k, p_r)$  in  $R\_idx[r]$  do
4.      if  $k \in M\_idx$  then
5.        for  $p_p$  in  $M\_idx[k]$  do
6.           $pos \leftarrow pos \cup \{(p_r, p_p)\}$ 
7.        for  $(p_r, p_p) \in pos$  do
8.          for  $(r_s, r_e, p_s, p_e)$  in  $LCSstr(r, P)$  do
9.            if  $r_s \leq p_r \leq r_e$  &  $p_s \leq p_p \leq p_e$  then
10.              $filt \leftarrow filt \cup \{(p_r, p_p)\}$ 
11.   if  $filt = \emptyset$  then
12.     for  $(x, y) \in pos$  do
13.        $s(x, y) \leftarrow |\{(x', y') \in pos | x' < x \text{ and } y' < y\}|$ 
14.    $filt \leftarrow filt$  store in descending order of  $s$ 
15.   return  $filt$ 

```

3.3 Extension and Verification:

In the verification stage, the filtered candidate positions are mapped to the reference genome, and appropriate extension strategies are applied to determine candidate regions. Finally, the edit distance between the read and these candidate regions is computed. This process effectively narrows down the alignment scope: instead of performing a time-consuming alignment of the short read against the entire long reference genome, the comparison is confined to localized regions of the reference sequence, thereby significantly improving alignment efficiency.

Specifically, the forward alignment fragment of the read can be represented as $r[i^*, m]$, where i^* denotes the starting position of the candidate seed in the read, and m is the read length. Correspondingly, on the pangenome \hat{P} , the forward alignment fragment is extended based on the coordinate j^* of the candidate seed combined with the read length. The final alignment is then computed using a variant of the edit distance algorithm[14], provided in Algorithm 3.

Algorithm 3: Dynamic Programming-based Edit Distance Variant AlgorithmCase1: $\hat{P}[j] \in \Sigma$

$$D_{i,j} = \begin{cases} i, \text{ if } j = 0 \\ j, \text{ if } i = 0 \\ \min \begin{cases} D_{i-1,j-1} \text{ if } r[i] = P[j] \\ D_{i-1,j-1} + 1 \text{ if } r[i] \neq P[j] \\ D_{i,j-1} + 1 \\ D_{i-1,j} + 1 \end{cases} \end{cases}$$

Case2: $\hat{P}[j] = "["$

$$D_{i,j} = D_{i,j-1}$$

Case3: $\hat{P}[j] = "|"$

$$D_{i,j} = D_{i,j'}, \text{ if } P[j'] = '|'$$

Case4: $\hat{P}[j] = "]"$

$$D_{i,j} = \min(D_{i,j''}) \text{ if } j' \leq j'' < j \text{ and } P[j'' + 1] \in \{[, \}$$

Starting from the selected seed position (i^*, j^*) , forward alignment is performed. Let $D_{i,j}$ represent the edit distance from the sequence fragment $r[i^*, i]$ to the fragment $\hat{P}[j^*, j]$. Algorithm 3 describes the method for calculating the edit distance in the presence of elastic degenerate symbols, which is divided into four cases. The first case follows the standard definition of edit distance, while the second, third, and fourth cases provide explicit rules for handling the special syntax symbols "[", "|", and "]". Specifically:

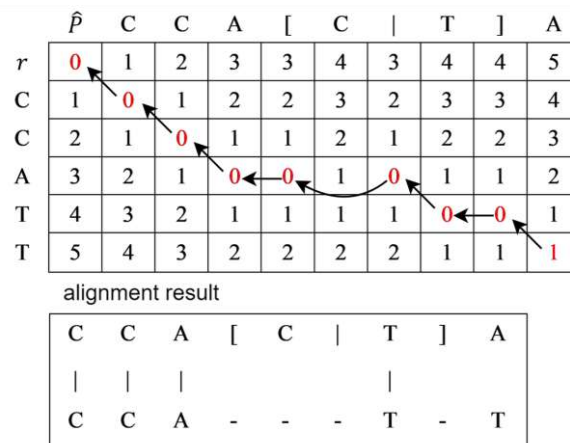
If $\hat{P}[j] = "["$, then the value of column j is set equal to the value of column $j - 1$.

If $\hat{P}[j] = "|"$, then the value of column j corresponds to the value of a specific column j' , where $P[j'] = "|"$, meaning that under the constraints of the syntax definition, the value from column j' is adopted.

If $\hat{P}[j] = "]"$, then the value of column j is the minimum among the values of certain columns j'' , where the constraint requires $P[j'' + 1] \in \{[, \}$, indicating that the minimum value is selected based on the column corresponding to the syntax symbol.

This variant of edit distance calculation enables more accurate and effective handling of alignment tasks involving syntax symbols, thus improving precision in pangenome sequence alignment.

In the example above, the forward alignment fragment of r is $r[3,8] = \text{CCATT}$, and the corresponding forward alignment fragment of \hat{P} is $\hat{P}[8,17] = \text{CCA}[C|T]A$. Using Algorithm 3 to compute the edit distance between these two fragments yields the alignment result shown in Figure 6.

**FIGURE 6: Edit Distance computation and traceback path**

From the lower-right corner of the dynamic programming matrix in Figure 6, it can be observed that the edit distance between the read and the candidate region in the pangenome is 1. The red-highlighted values represent the optimal alignment path, from which the best alignment result of the example is obtained through traceback. Similarly, the reverse alignment between r and

\hat{S} can also be computed, where reverse alignment is treated as the forward alignment of the reversed string. Finally, combining the forward and reverse alignment results yields the complete alignment outcome.

IV. EXPERIMENTAL RESULTS AND ANALYSIS

4.1 Experimental Data and Evaluation Metrics:

The experimental data used in this study were obtained from the China National Center for Bioinformation (CNCB). From this database, the SARS-CoV-2 reference sequence NC_045512.2 (length: 29,903 bp) and its corresponding variant data were downloaded. Considering the generation of the longest common substring and the presence of special syntax markers in elastic-degenerate symbols, a limited number of variants were introduced to the reference sequence to minimize potential interference. After preprocessing steps such as deduplication and removal of overlapping variants, a total of 1,383 SNPs were retained and incorporated into the reference sequence using elastic-degenerate symbols, generating a pangenome for alignment.

For the read datasets, experiments were conducted on both simulated and real datasets. To evaluate the performance of the proposed method in precise alignment, a series of comparative experiments were performed with leading sequence alignment algorithms. Two mainstream BWT-based aligners, BWA and Bowtie2, were selected. BWA includes three alignment algorithms; the two most performant, BWA-SW and BWA-MEM, were used in the experiments. Additionally, the popular hash-based aligner Minimap2 was included as a control. All tools were run with default parameters.

In experiments with the simulated dataset, the recall rate and precision rate were calculated by comparing the alignment positions reported by the algorithms with the true positions of reads. The recall rate reflects the ability of the alignment tool to correctly locate reads on the reference sequence, while the precision rate measures whether reads are aligned to their original positions on the reference sequence. The formulas are as follows:

$$\text{recall rate} = \frac{TM}{N} * 100\% \quad (3)$$

$$\text{precision rate} = \frac{TM}{M} * 100\% \quad (4)$$

where N is the total number of reads in the dataset, M is the number of reads that can be aligned to the reference sequence, and TM is the number of reads correctly aligned to their original positions on the reference. A read is considered correctly aligned if the difference between its reported position and true position falls within a predefined threshold.

For experiments with the real dataset, since the exact positions of sequenced reads on the reference genome are unknown, precision cannot be directly assessed. Instead, sensitivity is used as the evaluation metric. Sensitivity measures the proportion of correctly identified bases by the alignment algorithm and is calculated as follows:

$$\text{sensitivity} = \frac{M}{N} * 100\% \quad (5)$$

4.2 Results of Simulated Dataset Experiments:

For the simulated datasets, considering that the constructed pangenome contains elastic-degenerate symbols, the following procedure was adopted: first, a random starting position was uniformly selected in the pangenome sequence, and a segment of a specified length was extracted from this position, with its location in the reference sequence recorded. For known variant sites, one alternative allele was randomly selected for substitution. Errors were then introduced into the extracted subsequence, including base substitutions, insertions, or deletions, with an error probability of 0.1% per base.

In terms of experimental setup, seven short-read simulated datasets were generated with read lengths ranging from 50 bp to 150 bp, specifically 45 bp, 65 bp, 85 bp, 105 bp, 125 bp, 145 bp, and 165 bp, with each dataset containing 100,000 reads. Additionally, to evaluate the applicability of the proposed method for long reads, seven long-read simulated datasets were constructed with read lengths of 200 bp, 250 bp, 300 bp, 350 bp, 400 bp, 450 bp, and 500 bp, also containing 100,000 reads each.

In all experiments, (20,5)-minimizers were used to construct the index tables, and algorithm performance was tested across datasets of different scales. Figure 7 presents the alignment results of different algorithms on the simulated short-read datasets.

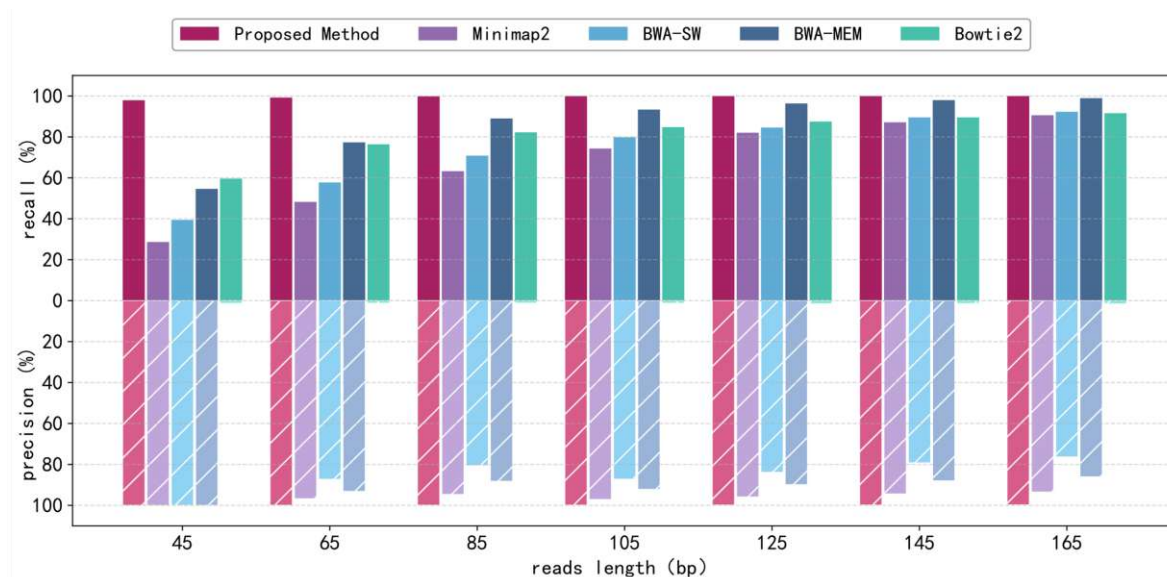


FIGURE 7: Recall and precision for short-read datasets aligned to the pangenome

From Figure 7, it can be observed that for short-read alignment to the pangenome, the proposed method outperforms mainstream alignment tools in both recall (97.94%–99.99%) and precision (99.72%–99.93%). In comparison, Minimap2 achieved a recall of 28.68%–90.60% and precision of 93.47%–99.94%; BWA-SW had a recall of 39.46%–92.30% and precision of 76.27%–99.91%; BWA-MEM reached a recall of 54.62%–98.95% and precision of 86.01%–99.93%; Bowtie2 showed a recall of 59.63%–91.62% but relatively lower precision. This reduced precision is likely due to its alignment strategy, which may produce nonspecific mappings when short reads contain insufficient information, thereby affecting accuracy.

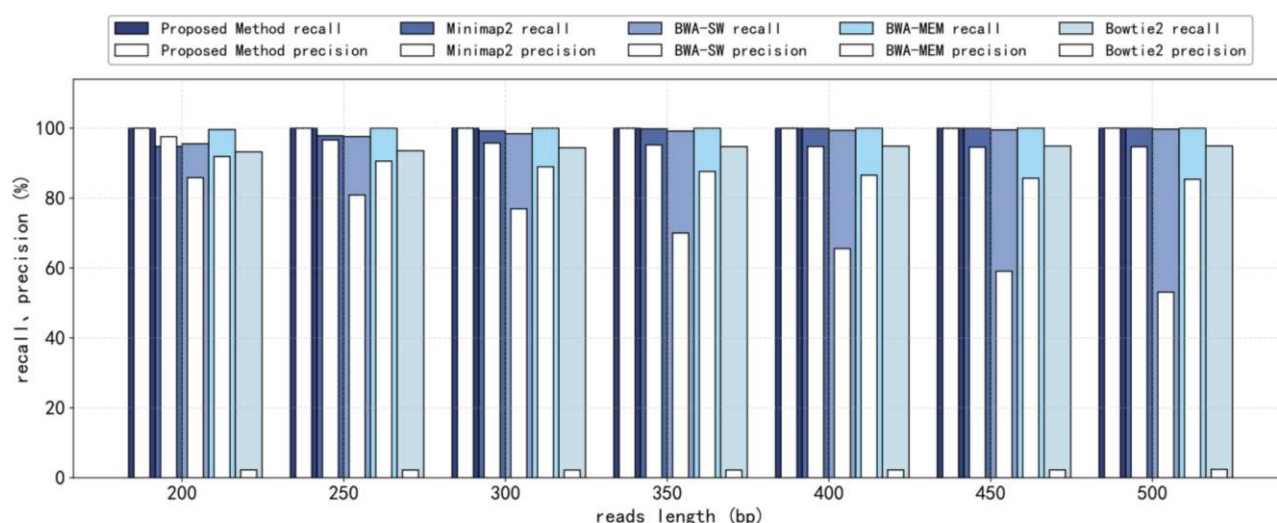


FIGURE 8: Recall and precision for long-read datasets aligned to the pangenome

Furthermore, as shown in Figure 8, for long-read alignment, the proposed method exhibits even more prominent advantages. Specifically, in long-read experiments, the method achieved a recall of 99.99%–100% and a precision of 99.94%–99.99%, indicating its ability to accurately locate reads on the reference sequence. In comparison, Minimap2 also performed stably in long-read scenarios, maintaining high recall and precision. The BWA algorithms remained competitive in recall but had slightly lower precision overall, whereas Bowtie2 performed poorly in both recall and precision. This is likely due to its design targeting short reads and reliance on an FM-index-based local alignment strategy, which may result in higher mismatch rates for long reads and consequently reduce overall precision.

In addition to recall and precision, positional error was introduced as a supplementary metric to evaluate the distance between the aligned and true positions. Smaller positional errors indicate higher accuracy in read placement. Figure 9, shown on a semi-logarithmic scale, presents the average positional errors for aligned reads across simulated short-read and long-read datasets.

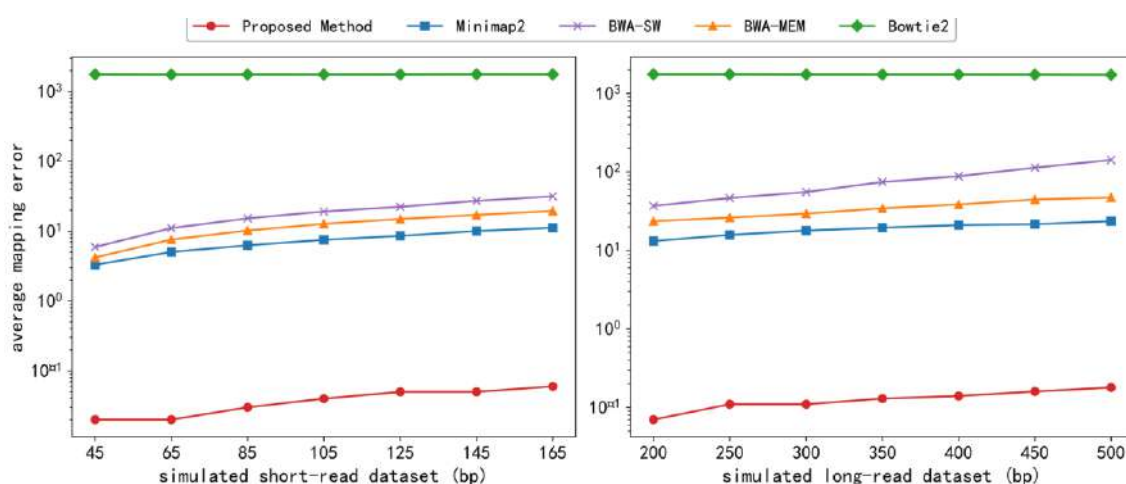


FIGURE 9: Average positional error of different algorithms on simulated datasets

As seen in Figure 9, the proposed method consistently outperforms existing tools in terms of average positional error for both short and long reads, demonstrating higher placement accuracy. Comparative results indicate that Minimap2 and BWA exhibit similar levels of positional error, while Bowtie2 shows the largest error, reflecting a higher proportion of false-positive alignments. These results further validate the superiority of the proposed method in alignment accuracy.

4.3 Results of Real Dataset Experiments:

Since simulated datasets cannot fully replicate the structural variants and sequencing errors present in real sequencing data, alignment rates and accuracy are typically higher for simulated reads than for real reads. To better evaluate the performance of the proposed algorithm in practical applications, comparative experiments were conducted on multiple real sequencing datasets.

For the real sequencing datasets, SARS-CoV-2 sequencing data were downloaded from the Sequence Read Archive (SRA) of the National Center for Biotechnology Information (NCBI). From datasets SRR33976238, SRR33976240, SRR34288732, and SRR31052680, the first 100,000 single-end reads of lengths approximately 51 bp, 76 bp, 102 bp, and 152 bp, respectively, were extracted for the experiments. Additionally, experiments were conducted on four longer-read datasets: the first 100,000 reads of lengths approximately 202 bp and 251 bp from SRR31052679, the first 100,000 reads of length approximately 300 bp from SRR11810739, and 81,000 reads of length approximately 351 bp from SRR11788183.

The four groups of real SARS-CoV-2 sequencing reads were aligned to the constructed pangenome, and the results are shown in Table 1.

TABLE 1
ALIGNMENT SENSITIVITY FOR REAL SARS-COV-2 SEQUENCING DATA

Comparison tools	Dataset			
	51bp	76bp	102bp	152bp
Proposed Method	56.74%	72.63%	74.16%	98.98%
Minimap2	30.57%	47.06%	60.22%	76.08%
BWA-SW	41.54%	57.54%	61.67%	86.73%
BWA-MEM	58.35%	76.34%	73.28%	97.20%
Bowtie2	58.43%	56.21%	61.29%	68.11%

From Table 1, it can be observed that due to the higher complexity of sequencing errors and variants in real data, the alignment sensitivity of all algorithms decreased compared with the simulated datasets. In the 51 bp dataset, the proposed method exhibited slightly lower sensitivity, likely because the short reads themselves contain limited information, and the method primarily relies on the generation of the longest common substring (LCSstr) during seed selection. Variants present in short reads can also impact the construction of LCSstr, thereby affecting the final alignment results. In the 76 bp dataset, BWA-MEM demonstrated higher sensitivity, while the proposed method showed slightly lower sensitivity but still outperformed the

other two algorithms. As read length increased, in the 102 bp and 152 bp datasets, the proposed method exhibited higher sensitivity, indicating that the method has advantages in handling real sequencing read alignment.

To further evaluate algorithm performance, experiments were conducted on the four real long-read datasets, with results presented in Table 2.

TABLE 2
ALIGNMENT SENSITIVITY FOR REAL LONG-READ SARS-CoV-2 DATASETS

Comparison tools	Dataset			
	202bp	251bp	300bp	351bp
Proposed Method	99.22%	99.86%	99.90%	99.98%
Miimap2	91.99%	97.71%	99.60%	98.51%
BWA-SW	91.13%	95.39%	99.50%	98.32%
BWA-MEM	98.86%	99.70%	99.99%	99.95%
Bowtie2	89.19%	89.30%	20.10%	58.97%

From Table 2, it can be seen that the proposed method also demonstrates high sensitivity for long-read alignment. For reads of 202 bp, 251 bp, and 351 bp, the algorithm consistently shows strong alignment performance. In the 300 bp dataset, the proposed method has slightly lower sensitivity than BWA-MEM but still significantly outperforms other alignment tools. These results indicate that the proposed method can effectively improve alignment sensitivity for real long reads, demonstrating considerable potential for practical application.

V. CONCLUSION

The algorithm achieves linear representation of SNP variants by introducing elastic-degenerate symbols, and combines minimizer indexing with a seed filtering strategy based on longest common substring intervals. This approach allows large-scale read alignment tasks to balance both sensitivity and accuracy.

Testing on simulated datasets demonstrated that the proposed method achieves high recall and precision across reads of varying lengths, with significantly lower positional errors compared to other alignment tools. This indicates that the method can more accurately map short reads back to the reference genome, thereby improving alignment accuracy. Further evaluation on real SARS-CoV-2 sequencing datasets showed that the proposed method outperforms other tools in terms of sensitivity in most datasets, with its advantage becoming particularly pronounced in long-read alignment tasks. These results validate the effectiveness of the proposed method for viral short sequence alignment and suggest that it provides a viable computational approach for large-scale genome alignment, as well as for pangenome-based alignment and viral variant analysis.

However, this work primarily focuses on aligning sequencing reads to reference genomes. Extracting biological interpretations from these differences requires close integration of biological and bioinformatics analyses to fully leverage the data. Additionally, while the dynamic programming-based seed filtering strategy enables optimal semi-global alignment, computational efficiency remains an area for improvement. Future work will focus on optimizing the algorithm's structure and implementation to enhance its generalizability and runtime performance, thereby broadening its applicability in complex genomic environments.

REFERENCES

- [1] Carlos W G, Cruz C S D, Cao B, et al. Novel Wuhan (2019-nCoV) Coronavirus[J]. American Journal of Respiratory & Critical Care Medicine, 2020, 201(4).
- [2] Van Dorp L, Acman M, Richard D, et al. Emergence of genomic diversity and recurrent mutations in SARS-CoV-2[J]. Infection, Genetics and Evolution, 2020, 83: 104351.
- [3] Wu P, Chen D, Ding W, et al. The trans-omics landscape of COVID-19[J]. Nature Communications, 2021, 12(1): 4543.
- [4] Bian Z., Liu R. Y., Ouyang H. T., et al. Investigation of non-structural protein mutations associated with non-selective mutations in SARS-CoV-2[J]. Virologica Sinica, 2024, 40(05): 961-969.
- [5] Manber U, Myers G. Suffix arrays: a new method for on-line string searches[J]. siam Journal on Computing, 1993, 22(5): 935-948.
- [6] Burrows M, Wheeler D J .A Block-Sorting Lossless Data Compression Algorithm[J].technical report digital src research report, 1994.
- [7] Ferragina P, Manzini G. Opportunistic data structures with applications[C]//Proceedings 41st annual symposium on foundations of computer science. IEEE, 2000: 390-398.

- [8] Roberts M, Hayes W, Hunt B R, et al. Reducing storage requirements for biological sequence comparison[J]. *Bioinformatics*, 2004, 20(18): 3363-3369.
- [9] Sirén J, Monlong J, Chang X, et al. Pangenomics enables genotyping of known structural variants in 5202 diverse genomes[J]. *Science*, 2021, 374(6574): abg8871.
- [10] Rautiainen M, Marschall T. GraphAligner: rapid and versatile sequence-to-graph alignment[J]. *Genome biology*, 2020, 21(1): 253.
- [11] Jain C, Rhie A, Zhang H, et al. Weighted minimizer sampling improves long read mapping[J]. *Bioinformatics*, 2020, 36(Supplement_1): i111-i118.
- [12] Rajput J, Chandra G, Jain C. Co-linear chaining on pangenome graphs[J]. *Algorithms for Molecular Biology*, 2024, 19(1): 4.
- [13] Li H. Minimap2: pairwise alignment for nucleotide sequences[J]. *Bioinformatics*, 2018, 34(18): 3094-3100.
- [14] Büchler T, Olbrich J, Ohlebusch E. Efficient short read mapping to a pangenome that is represented by a graph of ED strings[J]. *Bioinformatics*, 2023, 39(5): btad320.
- [15] Ding S. N., Wu M., Xu Y. Research on sequencing read alignment algorithms based on regional filtering[J]. *Information Technology and Network Security*, 2018, 37(04): 45-48+64.
- [16] Song S. Y., Cheng H. Y., Xu Y. A third-generation sequencing read alignment method based on low-frequency seeds[J]. *Computer Engineering and Science*, 2019, 41(09): 1551-1556.
- [17] Gao J., Xu Y. Pangenome graph sequence alignment algorithm based on combined minimizer seeds[J/OL]. *Computer Engineering*, 1-10[2024-11-26].
- [18] Gao J., Jiao Y., Zhang W. G. Review of high-throughput sequencing read alignment research[J]. *Life Science Research*, 2014, 18(05): 458-464.
- [19] Rathod A B, Gulhane S M, Padalwar S R. A comparative study on distance measuring approaches for permutation representations[C]//2016 IEEE international conference on advances in electronics, communication and computer technology (ICAECCT). IEEE, 2016: 251-255.
- [20] Levenshtein V I. Binary coors capable or 'correcting deletions, insertions, and reversals[C]//Soviet physics-doklady. 1966, 10(8).
- [21] Zheng Z. Y., Niu X. R., Xing K., et al. From assembly to application: challenges and breakthroughs in high-quality chromosome-level pig genomes[J]. *Chinese Journal of Animal Husbandry*, 2025(8).
- [22] Iliopoulos C S, Kundu R, Pissis S P. Efficient pattern matching in elastic-degenerate strings[J]. *Information and Computation*, 2021, 279: 104616.
- [23] Wilbur W J, Lipman D J. Rapid similarity searches of nucleic acid and protein data banks[J]. *Proceedings of the National Academy of Sciences*, 1983, 80(3): 726-730.
- [24] Wang K. Y., Kong S. Q., Fu Y. S., et al. Two bidirectional comparison-based longest common substring algorithms[J]. *Computer Research and Development*, 2013, 50(11): 2444-2454.
- [25] Skiena S S. The algorithm design manual[M]. New York: springer, 1998.
- [26] Bejerano G, Pheasant M, Makunin I, et al. Ultraconserved elements in the human genome[J]. *Science*, 2004, 304(5675): 1321-1325.
- [27] Lin H N, Hsu W L. Kart: a divide-and-conquer algorithm for NGS read alignment[J]. *Bioinformatics*, 2017, 33(15): 2281-2287.

Analysis of Global Trade Competition Pattern of New Energy Vehicles and Fuel Vehicles based on Multi-Layer Network

QiYu Hu

School of Big Data Statistics, Guizhou University of Finance and Economics, Guiyang, Guizhou Province

Received: 04 September 2025/ Revised: 10 September 2025/ Accepted: 20 September 2025/ Published: 30-09-2025

Copyright @ 2025 International Journal of Engineering Research and Science

This is an Open-Access article distributed under the terms of the Creative Commons Attribution

Non-Commercial License (<https://creativecommons.org/licenses/by-nc/4.0>) which permits unrestricted

Non-commercial use, distribution, and reproduction in any medium, provided the original work is properly cited.

Abstract— Use the 2023 global trade export data of new energy vehicles and fuel vehicles to build a multi-layer network of global new energy vehicles and fuel vehicles (including inter-country trade relationship networks and competition relationships networks), and use this network model to analyze new energy vehicles and fuel vehicles. The market competition landscape at the trade level is analyzed, and the application of multi-level exponential random graph model (ERGM) in this field is discussed. The results show that the global trade network of new energy vehicles and fuel vehicles shows an obvious center-periphery structure. Some countries have significantly maintained import relationships with multiple countries in the auto trade, and some countries have shown that they are interested in multiple countries. The propensity of a country to engage in export trade. Further ternary structure analysis revealed the existence of stratification in the trade patterns between new energy vehicles and fuel vehicles. In addition, the network structure analysis of competitive relationships shows that there are direct trade competition relationships between only a few countries, which means that only a few countries play the role of key industrial countries in the automotive trade field.

Keywords— Multilayered Network, Automobile Trade Network, Competition Network, Exponential Random Graph Model.

I. INTRODUCTION

Automobile trade is an important part of international trade, and its development trend not only reflects the global economic dynamics, but also indicates the direction of technological innovation and industrial development[1]. Its background can be traced back to the early 20th century, with the rapid development of the automobile industry, international trade has gradually risen. The purpose of automobile trade is to optimize the allocation of resources, meet the market demand for automobiles and related products through trade between different countries, and promote the growth of the global economy. With the acceleration of globalization, automobile trade not only promotes the transfer and innovation of technology, but also promotes the progress of production technology and the reconstruction of industrial chain [2][3]. According to their comparative advantages, countries have formed a pattern of division of labor and cooperation in the fields of automobile manufacturing, parts production and design. In addition, the automotive trade is closely related to changes in international policies, environmental regulations and market demand[4].

In recent years, with the enhancement of consumer awareness of environmental protection and the emphasis of policies on sustainable development, the trade volume of new energy vehicles has been rising, at the same time, the market of traditional fuel vehicles still maintains a certain demand, which reflects the transformation of the market structure and the change of consumer preferences. This not only reflects the diversity of market demand, but also promotes cooperation and competition among countries in the automobile trade[5]. At present, the research on automobile trade mainly includes two research directions: new energy automobile trade, which mainly focuses on the application of new technology and market expansion[6][7]; In the traditional fuel vehicle trade, relevant studies have discussed trade barriers, market share changes and so on[8]. Combining these two directions, this paper will discuss the current global trade competition pattern of new energy vehicles and fuel vehicles from the perspective of multi-layer networks.

In the pattern of trade competition, the status and role of the same country in different trade may change, which often leads to new structural characteristics of trade structure. Therefore, in order to deeply analyze the influencing factors of trade network, it is particularly important to establish a suitable empirical model. Among them, quadratic assignment program (QAP) and

exponential random graph model (ERGM) are two commonly used methods, but QAP analysis method has some shortcomings compared with ERGM[9] [10][11][12][13]. First, Mao Yang used the QAP method to discuss the influential factors of the global new energy vehicle trade network, such as reciprocity, network density and economic scale, but did not combine the network structure with some external factors. The reason is that QAP method fails to consider the influence of network structure such as ternary structure and endogeneity[14]. Secondly, Yiwen Deng believes that metal resources play an indispensable role in the field of automobile manufacturing, and the formation and evolution of the global metal value flow network are influenced by both endogenous and exogenous mechanisms. In order to explore these drivers in depth and overcome the single-dimensional limitations of quadratic allocators (QAP) in analyzing networks, the exponential random graph model (ERGM) can be applied to enrich the application of complex network theory in this area[15].

In general, existing studies usually discuss new energy vehicles and traditional fuel vehicles respectively from the perspective of network analysis, but lack a systematic and comprehensive analysis framework. Research on the construction of multi-layer frameworks based on complex networks and the exploration of the competitive relationship between the two types of automobile trade between different countries is relatively weak, which fails to fully reveal their potential connections in the global automobile trade network. Based on this, this paper analyzes the global trade competition network of new energy vehicles and fuel vehicles through the multi-layer network theory, filling the gap in the comprehensive analysis of the two types of vehicles in the existing research. This paper introduces the calculation method of cross-product competition intensity, quantifies the competition relationship between the two types of vehicles, and identifies the important factors affecting the trade competition network through the analysis of multi-layer network influencing factors.

II. DATA SOURCES AND NETWORK CONSTRUCTION

2.1 Data sources:

This study selected data from the United Nations Trade Database (UN Comtrade) to build a global automobile trade network at two network levels and applied a threshold to the data to ensure that only the most relevant connections were retained while preserving the network structure[16]. This procedure also helped to ignore countries that did not contribute much to trade but increased the degree of reciprocity. The threshold for retaining trade relations was 0.01% of total trade. This threshold was determined by applying a threshold to review the proportion of world trade retained to ensure that the network represented the majority of global trade. The 0.01% cut retained 96% and 94% of world trade for new energy vehicles and fuel vehicles, respectively, with 96 countries for new energy vehicles and 121 countries for fuel vehicles.

This paper selects 2023 as the research year, and selects eight types of new energy vehicles with HS codes of 870220, 870230, 870240, 870340, 870350, 870360, 870370, and 870380 in UN Comtrade. Eight types of fuel vehicles with HS codes of 870210, 870321, 870322, 870323, 870324, 870331, 870332, and 870333 are selected as the research objects. The GDP per capita data (in US dollars) can be obtained by visiting the World Bank website. In order to obtain more accurate estimation results, we logarithmize the GDP per capita. The data of trade distance network and common language network come from the CEPII database.

2.2 Network construction:

A multilayer network is a complex network structure composed of multiple single-layer networks. Each single-layer network represents a level, and the layers are interconnected through connections of various attributes and types[17]. This network structure goes beyond the single property limitation of a single node and edge, and can contain different types of nodes and their various connection methods, thereby showing the interactions and dependencies between different sub-networks. It provides a more powerful tool for understanding and analyzing complex systems with multiple attributes.

This paper uses the multi-layer network theory framework to analyze the trade relationship and trade competition relationship between new energy vehicles and fuel vehicles among countries. The new energy vehicle trade and fuel vehicle trade are constructed as single-layer networks respectively, and the cross-category trade competition relationship between different countries of new energy vehicles and fuel vehicles is used as the inter-layer relationship (trade competition network), so as to construct a multi-layer network structure of the trade relationship and competition relationship between new energy vehicles and fuel vehicles among countries. The specific construction process is as follows:

First, at the level of new energy vehicle trade network, this study reveals the flow direction of new energy vehicle trade by analyzing the trade relationship of new energy vehicles, and builds A new energy vehicle trade network (recorded as directed network A) accordingly. This network is a single-layer network, with countries as nodes in the network, and the trade between

countries is represented by edges, reflecting the import and export relationship between them. Secondly, from the perspective of the trade of fuel vehicles, this study analyzes the trade relations between countries to reveal the trade flow of fuel vehicles. Based on this, a fuel vehicle trading network (referred to as directed network B) is constructed. Finally, combining the two dimensions of new energy vehicles and fuel vehicles, a trade competition network of new energy vehicles and fuel vehicles (recorded as undirected network X) is constructed based on the trade competition relationship between them. The trade competition network is a binary network, which contains two types of nodes, representing new energy vehicles and fuel vehicles trading countries respectively. A connected edge between nodes of different classes indicates a competitive relationship between the two countries, while there is no connected edge between nodes of the same country. The final trade competition network connects the single-layer new energy vehicle trade network with the fuel vehicle trade network to form a multi-layer network (Figure1).

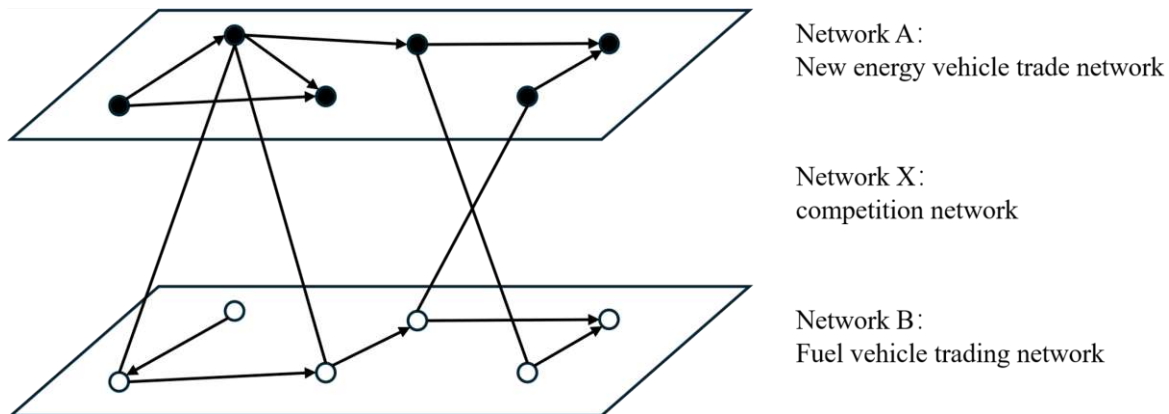


FIGURE 1: Schematic Diagram of the Global Trade Competition Network for New Energy Vehicles and Fuel Vehicles

III. DESCRIPTIVE ANALYSIS OF NETWORKS

3.1 Centrality analysis:

According to the above data, a network model is established and its structural characteristics are investigated. The calculation method of network centrality and its explanation are shown in Table 1.

TABLE 1
NETWORK CENTRALITY AND INTERPRETATION

Network indicator	Formulation	Explanation
Out and degree centrality	$C_{in}(i) = \frac{\sum_{j=1; i \neq j}^n x_{ij}}{n-1}, C_{out}(i) = \frac{\sum_{j=1; i \neq j}^n x_{ij}}{n-1}$	Represents the ability of a node to generate trade relationships with other nodes
Intermediation centrality	$C_B(i) = \frac{2 \sum_{j=1; k=1; j \neq k, j < k}^n \frac{d_{jk}(i)}{d_{jk}}}{(n-1)(n-2)}$	Represents the ability of the node to control the trade path in the network

According to the above formula, the centrality index of each country is measured and the top five countries in each index are listed in Table 2. European countries dominate the top rankings, indicating that they play an important role in the global automotive trading countries. This is mainly due to the fact that many European countries, due to their special geographical location and developed trade infrastructure, have become hubs connecting different regions, especially in the transnational supply chain and logistics system. At the same time, policy coordination and economic integration within the EU have enabled European countries to efficiently coordinate their cooperation with other countries and regions in international trade, thus enhancing their influence in global trade flows[18]. Therefore, the high ranking of European countries in the centrality indicators reflects their central position among the global automotive trading countries.

The centrality of exportation reflects its activity in the export activities of the automotive trade and its key role in the global automotive supply chain. With advanced technological advantages and strong production capacity, Germany, China, Japan and South Korea are the most active countries in the export of new energy vehicle trade and fuel vehicle trade, and have established

direct trade links with many countries. From the perspective of import centrality, European countries rank in the forefront of new energy vehicles and fuel vehicles trading countries in the world, showing strong import attraction and excellent global automotive supply chain integration capabilities. It is worth noting that the value of inbound centrality and the gap between countries is smaller than that of outbound centrality, indicating that there is a clear asymmetry in the import and export structure of the global automotive trading countries - that is, the source of imports is relatively concentrated, while the export market is more widely distributed.

TABLE 2
RANKING OF TOP FIVE COUNTRIES FOR AUTOMOBILE TRADE CENTRALITY

Type	Country	Out-degree Centrality	Country	In-degree Centrality	Country	Betweenness Centralit
New Energy Vehicles	Germany	0.716	Germany	0.232	Germany	0.112
	Japan	0.600	Belgium	0.200	Japan	0.054
	China	0.579	France	0.189	China	0.029
	United Kingdom	0.463	United Kingdom	0.179	Belgium	0.028
	South Korea	0.389	Italy	0.179	United Kingdom	0.026
Fuel Vehicles	Germany	0.550	Germany	0.267	Germany	0.121
	Japan	0.542	Belgium	0.200	United Arab Emirates	0.067
	China	0.400	France	0.192	Japan	0.064
	South Korea	0.392	United Arab Emirates	0.192	United States	0.035
	United States	0.367	Italy	0.183	Mexico	0.028

Betweenness centrality reflects the control a country node has over the trade paths in a network. Both Germany and Japan are ranked among the top five in the two automotive trade networks, playing a crucial hub role in these trade networks. This is not only due to their significant position in trade volume but also to their geographic location, economic strength, and trade policies, which together make these two countries key "bridges" connecting different nations and regions [19].

3.2 Core-Periphery Analysis:

The core-periphery structure was originally developed as a theoretical framework to explain the uneven economic development of regions, but it is now widely applied to describe various network structures. This structure refers to a network formed by numerous interconnected entities, where the nodes in the core are tightly connected, while the nodes in the periphery are relatively scattered. In other words, the central nodes of the network play a significant role, while the peripheral nodes occupy a relatively secondary position. This paper uses the core-periphery structure model developed by Borgatti to analyze the core-periphery structure in global new energy vehicle trade and conventional vehicle trade networks[20].

Using the core-periphery structure algorithm in UCINET software, we can calculate the core degree of each node in the network, which reflects the node's position in the trade network. The higher the core degree, the more important the node is in global trade. Based on the core degree values and in reference to relevant literature, we can categorize countries in the global automotive trade network into three levels: countries with a core degree greater than 0.2 are considered core countries, countries with a core degree between 0.1 and 0.2 are classified as semi-peripheral countries, and countries with a core degree below 0.1 are categorized as peripheral countries[7].

TABLE 3
CORE-PERIPHERY ANALYSIS OF GLOBAL AUTOMOBILE TRADE

Type	Core Country	semi-core country
New Energy Vehicles	Germany, South Korea, Japan, China, Slovakia, Hungary, United Kingdom, Belgium, Spain, Sweden, Czech Republic.	United States, France, Italy, Turkey, Poland, Austria, Netherlands.
Fuel Vehicles	Germany, Spain, France, Slovakia, Belgium, Italy, Hungary, Czech Republic, Japan, United Kingdom, Austria, Turkey, South Korea.	United States, Sweden, China, Netherlands, Romania, Morocco, Poland, Portugal.

The core-periphery analysis in Table 3 shows that the global trade network of new energy vehicles and fuel vehicles shows a clear core-periphery structure, and there are significant differences between the two. The number of core countries in the new energy vehicle trading countries is 11, which is reduced from the 13 core countries in the fuel vehicle trading network. Nine countries, including Germany, South Korea and Japan, are core countries in both automotive trade networks, thanks to their combined advantages in terms of automotive industry base, technological innovation, policy support and market demand. As a global automotive manufacturing power, Germany occupies an important position in the new energy vehicle and fuel vehicle trade network. This position is mainly due to the great contribution of its automotive industry to the national economy, as well as its continued leadership in technological innovation. It is with these advantages that Germany has been able to maintain its central position in the global automotive trade; South Korea and Japan each have unique competitive advantages in the field of fuel vehicles. South Korea is known for its advanced hybrid technology, excellent fuel efficiency and continuous technological innovation; Japan, on the other hand, has won the favor of global consumers with its high level of engine and transmission technology, excellent fuel economy, high warranty rate, as well as user-friendly design and excellent after-sales service. At the same time, traditional car manufacturers in both countries are actively transitioning to electrification; Slovakia stands out for its world-leading car production per capita and the significant contribution of the automotive industry to GDP [21]. Known as the "European law", Hungary has a strong car manufacturing and supply chain system, which has attracted many of the world's top car manufacturers to set up factories here. Belgium, with its superior geographical location and policy environment, has become an important hub for Chinese new energy vehicle exports to Europe. With its strategic location in Europe, Spain has the potential to become a "transit point" for the new energy vehicle industry. The UK has demonstrated in the field of new energy vehicles.

China and Sweden are both core countries in the new energy vehicle trading countries. China's rise is mainly due to the government's policy support, the growth of market demand, and the high importance of environmental protection [22]. With its huge market size and high consumer acceptance of new technologies, China has quickly become the world's largest market for new energy vehicles. At the same time, Sweden has successfully promoted the widespread popularity of new energy vehicles due to its long-term advocacy of environmental protection concepts and the implementation of positive government incentives [23]. However, in the trade of fuel vehicles, China is relatively weak in technology research and development and brand influence, and has not yet formed a global dominant position; Sweden's fuel vehicle market is small and is shrinking in the context of the rise of new energy vehicles. Therefore, the two countries have not yet become core countries in the field of fuel vehicles. In contrast, Turkey, Italy and Austria occupy a central position in the fuel vehicle trading network, mainly due to their strong vehicle manufacturing capabilities and mature market base. However, the policy support, technology research and development and market development in these countries in the field of new energy vehicles are relatively lagging behind. Although they have made some progress in new energy vehicles, their market penetration is still low, and the electrification transformation process is slow, so they are still in a semi-core state.

3.3 Competitive Relationship Analysis:

Since competition is mutual, its measurement indicators are usually considered undirected. In the network construction of this article, it is mentioned that there may be cross-product competition in automobile trade between countries with different energy forms. In order to quantify this cross-product trade competition, this study draws on previous methods for quantifying market competition to measure the intensity of competition between different countries and different energy forms in the same market in new energy automobile trade and fuel automobile trade [24][25][26]. The specific method is as follows:

$$W_{ij}^{\alpha\beta} = \sum_c \left\{ \left(\frac{H_{ic}^{\alpha}}{H_w^{\alpha}} \times \frac{H_{jc}^{\beta}}{H_w^{\beta}} \right) \times \left[1 - \frac{|(H_{ic}^{\alpha}/H_i^{\alpha}) - (H_{jc}^{\beta}/H_j^{\beta})|}{(H_{ic}^{\alpha}/H_i^{\alpha}) + (H_{jc}^{\beta}/H_j^{\beta})} \right] \right\} \times 100 \quad (1)$$

The formula $W_{ij}^{\alpha\beta}$ represents the competitiveness intensity between two countries in cross-product export. Here, c is a common market country for both new energy vehicle (NEV) exporting countries and fuel vehicle exporting countries. α and β represent new energy vehicles and fuel vehicles, respectively. H_w^α and H_w^β denote the total trade volume of new energy vehicles and fuel vehicles. H_{ic}^α represents the export volume from country i to country c for new energy vehicles, and H_{jc}^β represents the export volume from country j to country c for fuel vehicles. H_i^α and H_j^β are the total export volumes of country i for new energy vehicles and country j for fuel vehicles, respectively. The cross-product competitiveness intensity formula consists of two main parts. The first part $\left(\frac{H_{ic}^\alpha}{H_w^\alpha} \times \frac{H_{jc}^\beta}{H_w^\beta}\right)$ measures the competitive trade share. A larger competitive share indicates higher competitive pressure between the two countries. The second part $\left[1 - \frac{|(H_{ic}^\alpha/H_i^\alpha) - (H_{jc}^\beta/H_j^\beta)|}{(H_{ic}^\alpha/H_i^\alpha) + (H_{jc}^\beta/H_j^\beta)}\right]$ measures the similarity in the export structure between the new energy vehicle exporting country and the fuel vehicle exporting country. The higher the similarity, the more intense the cross-product competition between the two countries. Thus, a larger value of $W_{ij}^{\alpha\beta}$ indicates a higher level of cross-product competition between the two countries.

TABLE 4

TOP 20 COUNTRIES IN TERMS OF TRADE COMPETITION INTENSITY BETWEEN NEW ENERGY VEHICLES AND FUEL VEHICLES.

Rank	New Energy - Fuel	Competitiveness Intensity
1	South Korea - Japan	0.164
2	South Korea - Mexico	0.140
3	Japan - Mexico	0.121
4	Japan - Germany	0.119
5	Japan - South Korea	0.103
6	South Korea - Canada	0.099
7	Canada - Mexico	0.096
8	Japan - Canada	0.085
9	Germany - Japan	0.079
10	South Korea - Germany	0.063
11	Germany - Mexico	0.053
12	Canada - Japan	0.052
13	Germany - South Korea	0.048
14	Canada - South Korea	0.045
15	United Kingdom - Germany	0.044
16	Slovakia - Germany	0.039
17	Germany - Canada	0.037
18	China - Germany	0.031
19	Japan - United Kingdom	0.030
20	Japan - Italy	0.029

Table 4 shows the top 20 links between the exporters of new energy vehicles and fuel vehicles in 2023. As can be seen from the table, there is fierce trade competition between South Korea and Japan in the fields of new energy vehicles and fuel vehicles, which means that the export destinations of the two countries' automobiles are highly overlapped. In other words, some countries import new energy vehicles from South Korea and fuel vehicles from Japan at the same time. When the export volume of one party changes, the export volume of the other party will also be affected. This interconnected trade relationship shows that South Korea and Japan compete fiercely in the same market, and the export performance of the two countries is often driven by similar market dynamics.

Germany, Japan and South Korea have a high level of competition in the automobile trade, which is mainly due to their common technological advantages and global strategic layout in the automobile industry, and this competition is becoming more and more intense with the transformation of the global automobile industry. The German automotive industry is known for its precision engineering, advanced manufacturing processes and top design concepts, making it a global synonym for quality and

innovation. In contrast, the automotive industries of Japan and South Korea occupy an important position in the global market with efficient production models, excellent fuel efficiency and excellent reliability. They have shown significant advantages in mass production and cost control, especially in the low-end market and bulk consumer goods sector, and have successfully attracted a large number of consumers with their products' high cost performance and excellent durability. In addition to the technical competition, the global market strategy is also an important factor in the automobile trade competition of the three countries[27]. The automobile brands of the three countries have highly overlapping layouts and expansion strategies in many key markets around the world, especially in Europe, the United States, Asia and emerging markets, which have launched fierce market share competition. German companies usually occupy mature markets through high-end positioning and brand effect, while Japan and South Korea have successfully occupied price-sensitive markets with strong production capacity, advanced manufacturing technology and low production costs. Through large-scale production and efficient supply chain management, they are able to offer cost-effective models that meet consumers' demand for a balance between price and quality, especially in emerging markets and the low - and mid-range markets. Through cooperation with local enterprises, the establishment of production bases and research and development centers, the three countries have continuously optimized the supply chain and increased market penetration, forming an all-round competitive landscape.

Since the 1980s, Mexico has played an increasingly important role in North American automotive manufacturing. Its geographical proximity to the United States, coupled with lower production costs and higher production efficiency, makes Mexico an important investment destination for global automotive assemblers (including multinational companies from Europe, Asia and the Americas) and their suppliers land. These factors have allowed Mexico to occupy a key position in the global automotive industry supply chain, especially in meeting the needs of the North American market, becoming an important hub in a highly competitive market. In addition, Mexico has further enhanced its competitiveness in the global automobile industry through trade agreements with the United States (such as the North American Free Trade Agreement, NAFTA), attracting a large amount of foreign investment. As the center of gravity of the global automotive industry gradually shifts to Mexico, the region's manufacturing and supply chain networks have also developed significantly, consolidating Mexico's position as the core base for automotive production and assembly in the North American market[28].

Canada's automotive industry benefits from its high value-added activities, competitive market environment, increasing technical requirements and high employment characteristics, which together promote the competitiveness of its automotive industry. In addition, Canada's stable political environment, developed manufacturing base, advanced technology and well-trained workforce all provide a solid foundation for the competitiveness of its automotive industry. Canada's regional competitiveness is also reflected in its ability to provide a sustainable environment that attracts businesses and residents, especially its close economic ties with the United States, which provides a huge market advantage for Canadian automotive exports[1].

IV. ANALYSIS OF FACTORS AFFECTING MULTI-LAYER NETWORKS

4.1 Exponential Random Graph Model:

The exponential random graph model (ERGM) is a statistical model used to analyze the edge relationships between nodes in a network and the mechanisms by which they are formed. Traditional network analysis methods view relationships as networks consisting of nodes and edges, and different conclusions can be inferred by analyzing these networks[29]. In contrast, the exponential random graph model takes a different perspective, viewing the observed network as one of many possible network structures. The probability of its occurrence is affected by the structural effects of the network, node attributes, and covariate network factors. Among them, the structural effect is a key component of the ERGM framework, which can directly model the interdependence between nodes in the network[30]. Node attributes regard the formation of network connections as the result of the attributes of the participants themselves, thereby determining whether nodes with specific attributes are more or less likely to establish relationships[31]. Covariate networks refer to external variables that affect network structure and node relationships, such as language, geographic location, and other factors that may affect the connections between nodes[32].

According to Wang et al.'s multi-layer network extension of the ERGM model[33], the extension involves multiple network levels, including network level A, network level B, and meso-network X. The general form of the multi-layer ERGM model is:

$$P(A = a, X = x, B = b) = \frac{1}{k(\theta)} \exp \sum_Q \{ \theta_Q Z_Q(a) + \theta_Q Z_Q(x) + \theta_Q Z_Q(b) + \theta_Q Z_Q(a, x) + \theta_Q Z_Q(b, x) + \theta_Q Z_Q(a, x, b) \} \quad (2)$$

Where,

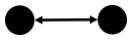


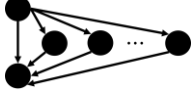
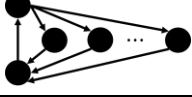


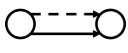
- $Z_Q(a)$ and $Z_Q(b)$ are internal network statistics for network layer A and network layer B.
- $Z_Q(x)$ is a network statistics of structural effects on meso-networks.
- $Z_Q(a, x)$ and $Z_Q(b, x)$ are network statistics that involve configurations of a single network (either a or b) and a meso network (x), representing the interaction between the two networks.
- $Z_Q(a, x, b)$ are the network statistics for the configurations that involve ties from all three networks.

MCMC-MLE (Markov Chain Monte Carlo Maximum Likelihood estimation) is usually used in ERGM (exponential random graph model) studies, but this study uses Bayesian inference method because it has more obvious advantages. MCMC-MLE first obtains a preliminary estimate through the pseudo-likelihood method, then compares the simulation results of multiple random networks with the results derived from the data, and finally adjusts the coefficients to increase the likelihood of matching between the two. Bayesian inference, on the other hand, incorporates more information by gradually updating the probabilities rather than simply comparing and adjusting the results of the analysis. Specifically, Bayesian estimation evaluates the probability of different values of various parameters in the analysis for a given observation data through MCMC, and uses a posterior distribution to reduce the uncertainty of the parameters. Compared with the maximum likelihood method, Bayesian inference usually achieves better results when dealing with complex data[34].

4.2 Network Configuration:

Table 5 provides an overview of the configurations contained in each individual level and their economic interpretations, including reciprocity in the network, transitive closure, etc. Among them, reciprocity indicates whether there is a mutual export trade relationship between countries in the network; if the estimated value is positive, it means that the network tends to form a mutual export trade relationship. Among the node attributes, GDP (gross domestic product) is used as an example of economic interpretation to analyze whether a country with a larger market size and a higher economic level is more likely to form trade import and export relationships. Network covariates are used to determine whether other network relationships are conducive to the establishment of existing network relationships. For example, the distance network is included to test whether trade is inhibited by distance, as predicted by the gravity model of international trade[35].

TABLE 5
SINGLE-LAYER NETWORK CONFIGURATION

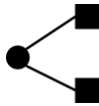
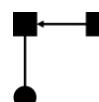
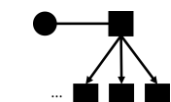
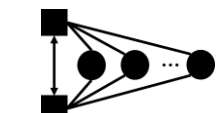
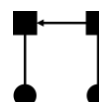
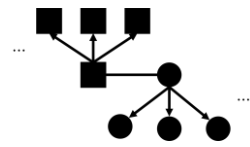
Configuration Name	Configuration	Economic Explanation
Reciprocity		Two-way reciprocal relationships established between countries. They import and export to each other.
AinSA		The tendency of some countries in the network to trade imports with multiple countries.
AoutSA		The tendency of some countries in the network to export to multiple countries.
ATA-T		Some countries in a network are more likely to trade with countries that have multiple trading partners.
ATA-C		The tendency for trade to occur within subgroups of countries.
Sender Effect		Is it true that the stronger a certain attribute is, the easier it is to conduct export trade?
Receiver Effect		Is it true that the stronger a certain attribute is, the easier it is to conduct import trade?
Covariate Network		Whether other network relationships are conducive to the establishment of trade relations between countries.

Note: ● represents the national node.

When exploring multi-level configurations, we focus on the interactions between different network levels, including the new energy vehicle trade relations between countries, the fuel vehicle trade relations, and the competitive relations between

countries in automobile trade. Table 6 summarizes these configurations in detail and provides corresponding economic explanations, mainly referring to the research of [36]. Through these explanations, we can better understand the competitive relations between countries in the trade of new energy vehicles and fuel vehicles, and how these relations affect the competitive landscape of global automobile trade.

TABLE 6
MULTI-LAYER NETWORK CONFIGURATION

Configuration Name	Configuration	Economic Explanation
XStar2A		Do some countries in the network establish trade competition relationships with multiple countries?
In2StarAX		Countries with high levels of competition tend to establish import relationships in international trade.
AAoutS1X		Countries with high levels of competition tend to establish multiple trade export relationships in international trade.
ATXAXrecipority		The tendency for two countries with the same rivalry to induce trade.
L3XAX		The tendency for countries with high levels of competition to trade.
AoutasxAoutBS		When two competing countries have a large trade export relationship, will it cause the other country to export a large amount of trade?

Note: ● represents a country-level node for automobile trade of one energy type, ■ represents a country-level node for automobile trade of another energy type.

V. RESULTS

5.1 ERGM estimation results:

All estimation procedures in this article are performed using MPNet software [37]. Under the conditions of network configuration and other effect parameters set by a specific model, parameter estimates can reflect the probability of occurrence of network configuration. A positive and significant configuration parameter indicates that the structure is observed in the test network more frequently than chance.

TABLE 7
ERGM ESTIMATION RESULTS OF NEW ENERGY VEHICLES

Configuration Name	Bayesian estimation [posterior mean (posterior standard deviation)]		
	Model 1	Model 2	Model 3
Reciprocity	1.121 (0.316)*	1.416 (0.259)*	1.231 (0.004)*
AinSA	-0.575 (0.182)*	1.040 (0.160)*	1.202 (0.004)*
AoutSA	1.087 (0.251)*	2.011 (0.197)*	1.981 (0.002)*
ATA-T	1.838 (0.162)*	0.399 (0.113)	0.320 (0.004)*
ATA-C	-0.263 (0.067)*	-0.072 (0.051)	0.008 (0.009)
GDP ReceiverA		3.958 (0.694)*	-0.156 (0.001)*
GDP Out2StarA		0.057 (0.002)*	0.080 (0.002)*
Common Language Network		-0.196 (0.137)	0.167 (0.001)*
Distance Network		-0.020 (0.009) *	-0.036 (0.009) *
Xstar2A			-0.207 (0.003) *
In2StarAX			-0.007 (0.003) *
AAoutS1X			0.036 (0.004) *
ATXAXrecipority			0.595 (0.006) *
L3XAX			0.002 (0.00005) *
AoutasxAoutBS			0.035 (0.0002) *

*Note: * Significant effect.*

In Table 7 we specify the impacts in increasing order of complexity. Model 1 only measures the structural effect of the new energy vehicle trade network, Model 2 adds attribute variables and covariate networks, and Model 3 adds the fuel vehicle trade network that competes with new energy vehicles to the former.

Model three covers both the structural effects of model one and the attribute variables and covariate network of model two. Using this model we can effectively analyze the trade competition network based on the interaction of various factors. In Model 3, the estimated coefficient of reciprocity is 1.231, indicating that there is significant reciprocity in global new energy vehicle trade, which means that many countries import and export to each other in the field of new energy vehicle trade. This reciprocity reflects the interdependent relationship between many countries in the international trade network and promotes cross-border commodity flows and economic cooperation. The estimated coefficient of AinSA is 1.202, which shows that there are obviously some countries that maintain trade and import relations with multiple countries at the same time. On the other hand, the estimated coefficient of AoutSA2 is 1.981, which shows that in the global automobile trade network, some countries have a significant tendency to trade exports to multiple countries. This phenomenon shows that these countries may have comparative advantages in some aspects and can become important supplier countries in the global automobile trade network, especially in the export of new energy vehicles and fuel vehicles. The ATA-T estimated coefficient is 0.320, further revealing a stratified trade pattern in which certain countries dominate the trade of new energy vehicles. This structural feature shows that in the global new energy vehicle trade network, there are obvious differences in the trade status of different countries. Some countries not only have advantages in exports, but also play an important role in imports, forming a global new energy vehicle trade "hub" countries. The results of GDP attribute variables at the new energy vehicle trade network level show that rich countries are more likely to have multiple export relationships, but are less likely to be importers in this sector. This reflects the ability of larger wealthy countries to source domestically rather than rely on imports. For the covariate network parameters of new energy vehicles, the estimated coefficient of the common language network is 0.167, indicating that there is significant overlap between the new energy vehicle trade network and the common language network and has an important positive impact on it. This is because a common language is conducive to trade between countries, helps to reduce and solve problems that arise during the trade process, and is conducive to the formation of trade relations. The estimated coefficient of the distance network is negative, which shows that distance has a certain restrictive effect on the development of global new energy vehicle trade. This is mainly because the automobile trade mainly relies on sea transportation. Although the cost of sea transportation is relatively low, distance still imposes certain restrictions on trade. We find that the Xstar2A estimated coefficient is -0.207, indicating that only a few countries have established extensive competitive linkages across multiple markets. This finding further emphasizes the key role of industrial competition in measuring the competitive position and economic strength of a

country or region within a specific industrial field, and also provides support for the existence of a core-periphery structure[38]. Specifically, in the new energy vehicle trade, only a few countries dominate and play a key role in the competition in the new energy industry. These countries usually have strong technological innovation capabilities, production scale advantages and market influence, thus occupying a key position in the competitive landscape of the global automobile industry. The estimated coefficients of $AAinS1X$ and $AAoutS1X$ are -0.007 and 0.036 respectively. It shows that key countries in the industrial field are more likely to have multiple trade and export relationships (positive and significant export trade), but are less likely to become trade importers (negative and significant import trade). This finding reveals the unique status and behavioral patterns of key industrial countries in the global trading system. Specifically, countries at key positions in the industrial chain usually have strong production capabilities, technological innovation capabilities and market influence, allowing them to occupy a dominant position in export trade. Especially in terms of high value-added and technology-intensive automotive products, these countries are able to meet global market demand and occupy important shares. However, these countries show lower dependence on import trade. This trade pattern reflects that key industrial countries prefer to pursue domestic self-sufficiency rather than rely on external supplies. This self-sufficiency strategy not only enhances their autonomy and competitiveness in the industry chain, but also reflects their control and resource allocation advantages in the global automobile industry chain. In addition, in the context of globalization, countries with the same competitive relationship often form upstream and downstream cooperative relationships in a certain field. This cooperation not only promotes similarities in types of export products but also deepens economic ties between countries. By estimating the reciprocal trade parameter with the same competitive relationship, we obtained an estimated value of 0.595, which indicates that countries with competitive relationships may have similar consumption habits and brand perceptions, thereby being more inclined to trade in the international market. contacts. The estimated coefficient of $L3XAX$ is 0.002, indicating that countries with many competitive relationships are often more likely to establish close trade ties. This phenomenon shows that in the context of globalization, competition does not always lead to estrangement. Instead, it can promote trade links between countries, thereby achieving mutual benefit and win-win results. When a country builds a strong export network in international markets, other countries may feel competitive pressure. This is verified through the $AoutASXAoutBS$ parameter, whose estimated value is 0.035, which shows that when a country builds a huge trade export system in the international trade market, other countries may face competition challenges. In order to maintain or enhance their position in the global market, these countries may increase exports to other countries to prevent the loss of market share.

TABLE 8
ERGM ESTIMATION RESULTS FOR FUEL VEHICLES

Configuration Name	Bayesian estimation [posterior mean (posterior standard deviation)]		
	Model 4	Model 5	Model 6
Reciprocity	1.670 (0.299)*	2.372 (0.242)*	2.524 (0.113)*
AinSB	-0.713 (0.136)*	1.293 (0.265)*	0.557 (0.225)*
AoutSB	0.868 (0.166)*	0.808 (0.329)*	2.100 (0.081)*
ATB-T	1.939 (0.113)*	1.648 (0.396)*	1.542 (0.243)*
ATB-C	-0.203 (0.068)*	-0.018 (0.171)	-0.104 (0.087)
GDP ReceiverB		-0.863 (0.425)*	1.729 (0.160)*
GDP Out2StarB		0.069 (0.030)*	0.529 (0.129)*
Common Language Network		-0.125 (0.375)	-0.121 (0.110)
Distance Network		-0.091 (0.108)	-0.673 (0.193)*
Xstar2B			-0.285 (0.089)*
In2StarBX			0.013 (0.092)*
ABoutS1X			0.062 (0.056)
ATXBXrecipority			13.059 (0.097)*
L3XBX			-0.002 (0.006)
AoutASXAoutBS			0.039 (0.014)*

*Note: * Significant effect.*

For fuel vehicles, the results are quite different (Table8). In Model 6, the estimated coefficient of reciprocity is 2.524, indicating that there is an obvious reciprocal trade relationship between countries in global fuel vehicle trade. This means that multiple countries import and export to each other in the field of fuel vehicles. This reciprocity facilitates the international flow of goods and promotes the development of transnational economic cooperation. The AInSB estimated coefficient is 0.557, indicating that in the global automobile trade network, some countries maintain significant trade and import relationships with multiple countries. This phenomenon reflects the key position of these countries in the global supply chain. They not only import automotive products from multiple source countries, but also meet domestic market demand through diversified import channels. This may be related to the country's large market size, diversified consumer demand and the complexity of the industrial structure. On the other hand, the AoutSB2 estimated coefficient is 2.100, indicating that some countries have a significant tendency to export to multiple countries in global automobile trade, and this trend is often closely related to the competitive advantages of these countries in automobile production and technology. The ATB-T estimated coefficient is 1.542, revealing the obvious layered structure in global fuel vehicle trade, with some countries occupying a dominant position in this field. This phenomenon reflects the asymmetry in the global fuel vehicle trade network and indicates that some countries may have strong automobile manufacturing industries and advanced technological levels, allowing them to dominate the global market. The estimated results of GDP attribute variables at the fuel vehicle trade network level are 1.729 and 0.529 respectively. This shows that economically wealthy countries not only tend to have more complex export relationships in the fuel vehicle trade network, but are also often important importing countries. This phenomenon shows that rich countries play a more complex role in the trade of fuel vehicles due to their higher level of economic development and industrial diversification. They not only export high value-added products to achieve economies of scale and scope, but also import to optimize resource allocation and reduce production costs to meet domestic market demand and maintain the integrity of the industrial chain. The distance network estimated coefficient is -0.673, indicating that geographical distance plays a certain restrictive role in global fuel vehicle trade. Although sea transportation is relatively economical in terms of cost, long transportation distances will still increase transportation time and risks, thus affecting the efficiency and reliability of trade. Longer distances can lead to higher transportation costs and require more time to complete transactions, thereby inhibiting the frequent occurrence of cross-border trade. The estimated coefficient of Xstar2B is -0.285, which implies that among many countries, only a few are able to establish extensive competitive ties. The ABinS1X estimated coefficient is 0.013, indicating that key countries in the fuel vehicle industry are more likely to have multiple trade import relationships. First of all, the complexity of the global supply chain of the fuel vehicle industry requires extensive cooperation among countries in raw materials, parts, and technology. Secondly, there may be complementary trade relations between key countries, that is, one country has comparative advantages in some links, while another country has advantages in other links. This complementarity promotes the formation of multilateral trade relations. The estimated coefficient of ATXBXrecipority is 13.059. In the fuel vehicle industry, competing countries have enhanced trade ties due to similar consumption habits and brand recognition. The estimated value of the AoutASXAoutBS parameter is 0.039, which shows that when a country establishes a strong export network in the field of international trade, other competitors may feel the pressure. In order to consolidate or enhance their competitiveness in the international market, these countries may strive to expand exports to other countries to avoid losing market share.

VI. CONCLUSION AND DISCUSSION

This paper mainly studies the global trade competition pattern of new energy vehicles and fuel vehicles. To this end, this paper regards the automobile trade network as a multi-level network, including the new energy vehicle trade network, the fuel vehicle trade network, and the cross-category trade competition relationship network between different countries. In this multi-level network, a few countries play the role of key industrial countries in the field of new energy vehicles. These countries tend to have multiple export trade relationships, but are unlikely to become trade importers. This shows that industrial powers prefer domestic self-sufficiency rather than relying on external imports. In the field of fuel vehicles, these key countries often have multiple trade import relationships. When a country establishes a strong export network in the international market, other countries may feel competitive pressure and increase exports to other countries to prevent the loss of market share. Overall, the global automobile trade pattern is jointly shaped by the trade network of new energy vehicles and fuel vehicles and their competition pattern. These networks and competition patterns are affected by many factors, including the country's economic strength, geographical environment, market demand, etc. These factors work together to form the current global automobile trade pattern.

The multi-layer ERGM method used in this paper has certain shortcomings. The model cannot handle weighted relationships and time series data, but it is full of unlimited possibilities in future research, especially when multi-layer network models and data sets are applied to different industries or different fields of the same industry. In addition, this method has the possibility

of further development. It can conduct a more in-depth comparative analysis of different trade industries, so as to more accurately understand the trade pattern in the global economy.

This analysis can be further extended to all links of automobile trade. Although we currently focus on automobile trade, this study can be extended to all links from Research and Development design to final use. By expanding the multi-layer dataset to cover all links of the automobile global value chain, we will be able to study the trade patterns of countries in more depth. In this way, the analysis will be more comprehensive and help reveal the trade dynamics and investment patterns of different countries in the automobile industry.

REFERENCES

- [1] Nagy J, Jámbo Z. Competitiveness in global trade: The case of the automobile industry[J]. *Economic Annals*, 2018, 63(218): 61-84.
- [2] Solvell O. Is the global automobile industry really global?[M]//*Strategies in Global Competition* (RLE International Business). Routledge, 2013: 181-208.
- [3] Rao R S. A Review on Competitive Structure of Automobile Industry[J]. *Asian Journal of Applied Science and Technology*, 2017, 1(9): 175-185.
- [4] C. Zuo. Research on the impact of trade policy uncertainty on the innovation of Chinese new energy vehicle enterprises. Master's thesis, Anhui University of Finance and Economics, 2022.
- [5] Rosal I D .European dieselization: Policy insights from EU car trade[J]. 2022.
- [6] Bharathidasan M, Indragandhi V, Suresh V, et al. A review on electric vehicle: Technologies, energy trading, and cyber security[J]. *Energy Reports*, 2022.
- [7] W. Qi and Q. Li. Research on the dynamic evolution characteristics and influencing factors of the global new energy vehicle trade network. *World Regional Studies*, 33(2), 2024.
- [8] Subhani M I, Ezhak E, Osman A, et al. Volatilities in Market Shares through Financial Fundamentals for Global Automobile Industry[J]. *Transportation Research Procedia*, 2022, 63: 2409-2420.
- [9] Cranmer S J, Leifeld P, McClurg S D, et al. Navigating the range of statistical tools for inferential network analysis[J]. *American Journal of Political Science*, 2017, 61(1): 237-251.
- [10] Krackardt D .QAP partialling as a test of spuriousness[J]. *Social Networks*, 1987, 9(2):171-186.
- [11] Snijders T A B, Pattison P E, Robins G L, et al. NEW SPECIFICATIONS FOR EXPONENTIAL RANDOM GRAPH MODELS[J]. *Sociological Methodology*, 2006, 36(1).
- [12] H. Wu, R. Wang, and M. Y. Yin. Analysis on the global forest products export trade network pattern and influencing factors based on ERGM model. *Journal of Agricultural and Forestry Economics and Management*, 21(02):188-197, 2022. ISSN 2095-6924.
- [13] Hoff P D, Raftery A E, Handcock M S .Latent Space Approaches to Social Network Analysis[J]. *Publications of the American Statistical Association*, 2002, 97(December):1090-1098.
- [14] M. Yang. Research on the evolution and influencing factors of global new energy vehicle trade network. Master's thesis, Hebei University of Economics and Business, 2024.
- [15] Deng Y, Guo Y, Zhang H, et al. Spatio-temporal evolution and driving mechanism of metal value flow networks: A global value chain perspective[J]. *Journal of Cleaner Production*, 2024, 468: 143012.
- [16] Shore J C. Market formation as transitive closure: The evolving pattern of trade in music[J]. *Network Science*, 2016, 4(2): 164-187.
- [17] F. An, X Gao, N Liu, Z Wang, Y. Li, Gao, and H. E. Stanley. Cluster-based topological features of nodes in a multiplex network—from a network of networks perspective. *New Journal of Physics*, 21(10): 103014, 2019.
- [18] Soete S, Van Hove J. Dissecting the trade effects of Europe's economic integration agreements[J]. *Journal of Economic Integration*, 2017: 193-243.
- [19] S. Bakari. Trade and Economic Growth in Germany. 2017.
- [20] Borgatti S P, Everett M G. Models of core/periphery structures[J]. *Social networks*, 2000, 21(4): 375-395.
- [21] Saxunova D, Novackova D, Bajzikova L. Focus on the Automotive Industry in the Context of a Globalization Process in Slovakia[J]. *Journal of Eastern Europe Research in Business and Economics*, 2018, 2018.
- [22] Zhang L, Qin Q. China's new energy vehicle policies: Evolution, comparison and recommendation[J]. *Transportation Research Part A: Policy and Practice*, 2018, 110: 57-72.
- [23] Haustein S, Jensen A F, Cherchi E. Battery electric vehicle adoption in Denmark and Sweden: Recent changes, related factors and policy implications[J]. *Energy Policy*, 2021, 149: 112096.
- [24] Glick R, Rose A K. Contagion and trade: why are currency crises regional?[J]. *Journal of international Money and Finance*, 1999, 18(4): 603-617.
- [25] Zhang H Y, Ji Q, Fan Y. Competition, transmission and pattern evolution: A network analysis of global oil trade[J]. *Energy Policy*, 2014, 73: 312-322.
- [26] Z. Ma, M. Jiang, and C. Liu. The network structure and evolution characteristics of global graphite trade competition from the perspective of multi-layer networks. *China Mining*, 33(3):1-10, 2024.
- [27] Y. Liu and L. Tong. Dynamic analysis of the industrial competitiveness performance of the three major german automobile manufacturers. *Scientia Geographica Sinica*, 38(7), 2018..

- [28] Contreras O F, Carrillo J, Alonso J. Local entrepreneurship within global value chains: a case study in the Mexican automotive industry[J]. *World development*, 2012, 40(5): 1013-1023.
- [29] Jackson M O. *Social and Economic Networks*[J]. 2008.
- [30] Jang Y, Yang J S .The dynamics of the EU's nuclear trade network: An ERGM analysis[J].*Structural Change and Economic Dynamics*, 2022, 63.
- [31] Toivonen R, Kovanen L, Kivelä M, et al. A comparative study of social network models: Network evolution models and nodal attribute models[J]. *Social networks*, 2009, 31(4): 240-254.
- [32] Cranmer S J, Desmarais B A. Inferential network analysis with exponential random graph models[J]. *Political analysis*, 2011, 19(1): 66-86.
- [33] Wang P, Robins G, Pattison P, et al. Exponential random graph models for multilevel networks[J]. *Social Networks*, 2013, 35(1): 96-115.
- [34] Koskinen J, Snijders T A B, Lusher D, et al. Simulation, estimation and goodness of fit[M]//*Exponential random graph models for social networks: Theory, methods and applications*. Cambridge University Press, 2013: 141-166.
- [35] De Groot H L F, Linders G J, Rietveld P, et al. The institutional determinants of bilateral trade patterns[J]. *Kyklos*, 2004, 57(1): 103-123.
- [36] Smith M, Gorgoni S, Cronin B. International production and trade in a high-tech industry: A multilevel network analysis[J]. *Social Networks*, 2019, 59: 50-60.
- [37] Wang P, Robins G, Pattison P, et al. MPNet: Program for the simulation and estimation of (p^*) exponential random graph models for multilevel networks[J]. Melbourne, Australia, 2014.
- [38] Li Y, Liu Y, Pu Y. Dynamic changes in the bauxite trade competition network structure and its influencing factors: Based on temporal exponential random graph model[J]. *Resources Policy*, 2024, 95: 105176.

Solar versus Electrolysis Methods for Green Hydrogen Production: A Meta-Analysis of Efficiency, Yield, and Cost Performance

Arjun Aditya Shah

Ahmedabad International School, Ahmedabad, Gujrat, INDIA

Received: 05 September 2025/ Revised: 14 September 2025/ Accepted: 19 September 2025/ Published: 30-09-2025

Copyright © 2025 International Journal of Engineering Research and Science

This is an Open-Access article distributed under the terms of the Creative Commons Attribution

Non-Commercial License (<https://creativecommons.org/licenses/by-nc/4.0>) which permits unrestricted

Non-commercial use, distribution, and reproduction in any medium, provided the original work is properly cited.

Abstract—

The global transition to sustainable energy systems has accelerated interest in green hydrogen production, with solar and electrolysis methods emerging as leading technological pathways. However, systematic comparative evidence across multiple performance dimensions remains limited, creating challenges for evidence-based technology selection decisions.

This study aims to compare the effectiveness of solar and electrolysis methods for green hydrogen generation through systematic review and meta-analysis, examining efficiency, hydrogen yield, and levelized cost of hydrogen (LCOH) across recent scientific literature.

A comprehensive literature search was conducted across multiple databases (Web of Science, Scopus, PubMed, IEEE Xplore, ScienceDirect) for studies published from 2015-2025. Data were extracted and standardized using established conversion factors for efficiency (%), hydrogen yield (kg/day), and cost (USD/kg). Statistical analyses used Mann-Whitney U tests due to assumption violations, with effect sizes calculated using Cohen's conventions.

Forty-seven studies met the inclusion criteria, providing 8-20 studies per outcome measure. Electrolysis methods demonstrated significantly higher efficiency (55.8% vs 19.4%, $p = 0.001$, large effect $r = 0.62$) and more consistent, lower costs (\$5.09 vs \$8.03/kg, $p < 0.10$, medium effect $r = 0.335$). No statistically significant difference was found in hydrogen yield despite solar methods showing 14.72 times higher geometric mean, indicating that deployment scale influences yield more than technology choice.

Electrolysis methods currently offer superior consistency and commercial readiness, while solar approaches show potential for breakthrough performance under optimal conditions. The findings suggest that diversified technology portfolios may optimize adoption of green hydrogen across countries, with technology selection depending on specific application requirements, risk tolerance, and local conditions rather than technological superiority.

Keywords— *Green hydrogen production, Meta-analysis, Electrolysis technologies, Solar hydrogen systems, Renewable energy comparison.*

I. INTRODUCTION

The global green hydrogen market has experienced unprecedented growth, with production capacity reaching 0.3 million tons annually in 2022 and projections indicating expansion to 38 million tons by 2030 (International Energy Agency, 2023). Leading developed economies have established ambitious targets: Germany aims for 5 GW electrolyzer capacity by 2030, Japan targets 3 million tons of hydrogen imports annually, and Australia plans 1.7 GW of renewable hydrogen projects, while developing nations including India (5 million tons production target), Brazil (18 GW planned capacity), and South Africa (500 MW electrolyzer installations) are rapidly scaling their hydrogen capabilities (Hydrogen Council, 2024).

The factors affecting green hydrogen production effectiveness vary significantly across technological approaches, with numerous studies demonstrating diverse performance characteristics. Solar-based hydrogen generation studies by Ahmad et al. (2025) and Li et al. (2023) have examined photoelectrochemical and photovoltaic-electrolysis systems showing efficiency

ranges of 4-35%, while electrolysis research by Kumar (2024), Shaban (2024), and Muhammad et al. (2025) has investigated alkaline, PEM, and solid oxide technologies demonstrating 60-95% conversion efficiencies. Cost effectiveness studies across different regions have revealed varying economic performance, with Vartiainen et al. (2022) reporting European costs of €1.0-2.7/kg, Abdelsalam (2024) finding Middle Eastern costs of \$6.78/kg, and Selvam (2025) documenting global ranges of \$3.2-7.1/kg for different technological configurations.

Meta-analysis is a systematic quantitative synthesis methodology that enables strong statistical comparison of heterogeneous research findings by standardizing diverse experimental conditions, measurement protocols, and outcome reporting formats. This approach can be used to overcome the limitations of individual studies and provide evidence-based insights into the relative effectiveness of competing technologies.

There is extensive existing research on the performance drivers and factors affecting the effectiveness of green hydrogen production over recent years across different countries, but limited research exists in comparing the systematic performance differences between solar and electrolysis methods. Most studies have focused on individual technologies or specific applications within single geographic contexts, creating knowledge gaps in comparative technology assessment. Recent changes in materials science, system integration approaches, and manufacturing scale economies have led to significant shifts in the relative performance patterns of solar and electrolysis hydrogen production technologies.

A systematic comparative study can help emerging economies such as India, Brazil, and South Africa make informed technology selection decisions for their national hydrogen strategies, thereby contributing to accelerated clean energy transition and economic development through optimal resource allocation toward the most effective technological pathways.

It is essential to understand how various performance factors impact hydrogen production effectiveness across different technological approaches in comparison to established benchmarks, enabling governments, policy advisors, and organizations working toward clean energy deployment to understand technological similarities and dissimilarities for informed policy decisions. It is equally important to study the evolving performance characteristics and changing technological advantages as both solar and electrolysis methods undergo rapid development. To the best of the researcher's knowledge, there is very limited research that systematically compares the effectiveness of solar hydrogen production methods with electrolysis approaches using standardized meta-analytical techniques.

Therefore, this study aims to investigate the factors affecting green hydrogen production effectiveness and the extent to which different technological approaches demonstrate superior performance, comparing solar and electrolysis methods for recent technological developments through comprehensive meta-analysis.

More specifically, the study addresses the following research questions:

- RQ1: What are the comparative efficiency levels between solar and electrolysis methods for green hydrogen production?
- RQ2: To what extent do hydrogen yield capacities differ between solar and electrolysis technological approaches?
- RQ3: What are the differences in levelized cost of hydrogen (LCOH) between solar and electrolysis methods across different studies and contexts?

The paper is organized as follows. The next section deals with an in-depth literature review of green hydrogen production technologies and their comparative assessment worldwide. The next section discusses the research methodology adopted for systematic review and meta-analysis. This is followed by the findings of the statistical analysis conducted using data from 47 studies across solar and electrolysis methods. The conclusions from the findings are presented next. Finally, the discussion section discusses the practical inferences of the study, limitations and further scope for research..

II. LITERATURE REVIEW

2.1 Green Hydrogen:

Green hydrogen has become an essential part of the world energy transition as hydrogen made by electrolysis from renewable energy sources, with little or no carbon emissions (Chiroșcă et al., 2024). The term was initially officially coined by the National Renewable Energy Laboratory, which applied renewable hydrogen as a synonym for green hydrogen production from renewable sources (NREL, 1995). The International Renewable Energy Agency (IRENA, 2019) considers green hydrogen a

near-zero carbon production path employing renewable electricity for water electrolysis, separating it from gray hydrogen from fossil fuels and blue hydrogen with the help of carbon capture technologies.

The rationale behind the development of green hydrogen is based on several reasons. According to Gondal et al. (2018), hydrogen can be a good alternative to fossil fuels because of political, economic, and ecological benefits, whereas Kakoulaki et al. (2021) demonstrate that the technical potential of renewable energy sources such as wind, solar, and hydro is adequate to supply present electricity demand and extra demand for the production of green hydrogen. This abundance of renewable materials places green hydrogen as a scalable response to energy security needs as well as climate mitigation goals (Raman et al., 2022).

The strategic relevance of hydrogen towards deep decarbonization has been underscored by several researchers. Parra et al. (2019) and Maestre et al. (2021) emphasize how hydrogen has the potential to be an integral component of holistic hybrid renewable energy systems, allowing for higher system integration and robustness. The "Hydrogen Economy" idea has undergone revived interest, fueled by international sustainability needs, decreasing costs of renewables, and fast technological progress (Yap et al., 2023; Østergaard et al., 2020; IRENA, 2023). Bibliometric studies demonstrate exponential growth in hydrogen research during the last decade, both indicating scientific attention and policy pressure (Kar et al., 2022; Kourougianni et al., 2024).

Green hydrogen production synergizes across several Sustainable Development Goals, most importantly SDG 7 (Affordable and Clean Energy) and SDG 13 (Climate Action), by providing energy access with reduced environmental footprint (Armaroli & Barbieri, 2021). Green hydrogen growth in the market is mainly fueled by industrial sectors that are hard to decarbonize such as steel, chemicals, transport, and energy storage applications (Oliveira et al., 2021)

2.2 Current State and Challenges:

Despite its potential, the current global hydrogen production landscape remains dominated by fossil fuel-based methods. The International Energy Agency (2023) reports that gray hydrogen production results in over 900 million tonnes of CO₂ emissions annually, representing 2.5% of global emissions. Only 0.7% of hydrogen production (approximately 1 Mt out of 95 Mt total) comes from low-emission methods, primarily blue hydrogen with carbon capture technologies. Production from water electrolysis using renewable electricity remains below 0.1 Mt annually, highlighting the significant scale-up challenge ahead (IEA, 2023).

Investment trends indicate growing recognition of hydrogen's strategic importance. Hydrogen technologies represented approximately 5% of global clean energy research and development budgets in 2021, with public investment increasing by 35% to reach \$1.3 billion USD (IEA, 2022). By 2022, this research area had grown to 7.5% of clean energy technology budgets, which is an indication of accelerating policy support and commercial interest (IEA, 2023). These investments have made Green Hydrogen Energy Systems central elements in sustainable energy and climate mitigation strategies (Kourougianni et al., 2024).

However, significant technical and economic challenges persist. Dincer and Acar (2015) note that green hydrogen technologies are not readily accessible with reasonable effectiveness and cost, citing studies showing photovoltaic electrolysis costs exceeding \$5/kg for hydrogen with energy efficiencies below 5%. Nevertheless, technological improvements and declining renewable energy costs are steadily reducing production costs (Islam et al., 2024; Reda et al., 2024).

The technological maturity varies significantly across different green hydrogen production approaches. While some electrolysis technologies have reached commercial deployment, many solar-based hydrogen production methods remain at laboratory or pilot scales, creating disparities in performance validation and cost assessment (Chiroșcă et al., 2024).

2.3 Green Hydrogen Production Technologies:

2.3.1 Electrolysis Technologies:

Water electrolysis is the most mature approach for green hydrogen production, using electricity to split water molecules into hydrogen and oxygen (IEA, 2019). Three primary electrolysis technologies have emerged as leading candidates for commercial deployment.

Alkaline Electrolysis (AEL) is the most mature electrolysis technology, using liquid alkaline electrolytes, typically potassium hydroxide (KOH), operating at temperatures between 60-80°C (Schmidt et al., 2017). Alkaline systems benefit from lower material costs due to the absence of noble metal catalyst requirements, using stainless steel electrodes instead (Buttler & Spliethoff, 2018). The technology operates at current densities ranging from 100-300 mA/cm² with single cell voltages of 1.7-

1.8 V, and can achieve lifespans exceeding 100,000 hours with appropriate maintenance (Domenech et al., 2021). Current investment expenses range from 500-1000 €/kW with operation and upkeep costs of 2-6% annually.

Proton Exchange Membrane Electrolysis (PEME) uses solid polymer electrolytes with high proton conductivity, enabling higher current densities around 1,000 mA/cm² and rapid response to power fluctuations in the millisecond range (Schmidt et al., 2017). This technology features high modularity and compactness through zero-gap architecture and Membrane-Electrode Assembly (MEA) design, making it suitable for coupling with variable renewable electricity sources (Buttler & Spliethoff, 2018). However, PEME systems require expensive noble metal catalysts (platinum, iridium) and have higher stack costs, with investment costs ranging from 600-1300 €/kW and operation and maintenance costs of 3-5% annually (Domenech et al., 2021).

Solid Oxide Electrolysis (SOEC) operates at high temperatures (500-850°C) using solid ceramic electrolytes, typically yttria-stabilized zirconia, achieving higher electrical efficiencies through combined heat and electricity utilization (Bhandari et al., 2014). SOEC systems can operate above 1,000 mA/cm² with single cell voltages around 1.3 V, though durability challenges remain with continuous operation limited to approximately 10,000 hours due to thermal cycling effects (Domenech et al., 2021). The technology remains at early development stages with higher investment costs estimated above 2000 €/kW.

2.3.2 Solar-Based Hydrogen Production:

Solar hydrogen production covers multiple technological approaches that directly use solar energy for hydrogen generation. The historical development of solar hydrogen research traces back to early work by Lodhi (1987) on high-temperature water dissociation, thermochemical water splitting, and photolysis processes. Later classifications by Lodhi (2004) identified solar, sea/ocean, hydro, wind, and nuclear energy as primary green sources for hydrogen production, with potential feedstocks including fresh water, seawater, hydrogen sulfide, and biomass (Dincer & Acar, 2015).

Solar hydrogen production methods can be categorized based on their primary energy conversion mechanism and feedstock requirements. These approaches include photoelectrochemical water splitting, concentrated solar power thermochemical processes, photovoltaic-powered electrolysis systems, and biomimetic artificial photosynthesis techniques (Miltner et al., 2010; Alstrum-Acevedo et al., 2005). Each approach has distinct advantages in terms of direct solar energy utilization and unique challenges related to efficiency, scalability, and cost-effectiveness.

2.4 Comparative Studies and Performance Assessment:

Limited systematic comparative analysis exists between solar and electrolysis methods for green hydrogen production, despite the importance of such comparisons for technology selection and policy development. Most existing studies focus on individual technologies or specific applications within single geographic contexts, creating knowledge gaps in cross-technology performance assessment.

Studies examining photovoltaic electrolysis systems have reported variable performance characteristics depending on system integration, scale, and operating conditions. While some research shows competitive efficiency potential, cost analyses consistently indicate challenges in achieving economic competitiveness with conventional hydrogen production methods (Dincer & Acar, 2015). The variability in reported performance metrics across different studies suggests significant influence of experimental conditions, measurement methodologies, and system boundaries on comparative assessments.

Electrolysis technologies benefit from more extensive commercial deployment and standardized performance reporting, facilitating more consistent comparative analysis. However, differences in system integration, renewable electricity sources, and operational profiles lead to variability in real-world performance.

Lack of comparable frameworks in consideration creates challenges for evidence-based technology choice. Various studies use different definitions of efficiency, methods of calculation of costs, and boundaries of performance, making quantitative comparison between solar and electrolysis methods difficult.

2.5 Research Gaps and Meta-Analysis Motivation:

Recent research identifies a few significant gaps in comparative green hydrogen technology evaluation. In the first place, the failure to systematically quantitatively synthesize findings across studies constrains the potential to make strong conclusions regarding relative technology performance. Specific studies might be subject to certain experimental conditions, regional contexts, or methodological decisions that are not indicative of wide-scale technology potential.

Second, the dynamics of very fast technological progress in solar as well as electrolysis solutions imply that performance standards set in previous research may no longer be indicative of current performance capability. Recent breakthroughs in

materials science, systems integration, and scale-up of production mean new comparative estimates reflecting latest technological advancements are needed.

Third, most studies concentrate on individual performance metrics like cost or efficiency without systematic assessment across multiple outcome measures. Large-scale technology selection calls for comprehension of efficiency-yield capacity-economic performance trade-offs, which individual studies hardly cover.

Fourth, the variability of measurement units, reporting standards, and system boundaries between studies poses difficulties in direct comparison. Standardization is required to facilitate meaningful cross-study synthesis and meta-analytical strategies.

Lastly, geographic and economic context differences profoundly impact cost-effectiveness and performance of technology, but little research considers these factors in comparative evaluations. It is vital to understand variations in performance across varying deployment contexts for guiding technology selection decisions in various global markets.

These gaps in research highlight the call for systematic review and meta-analysis methods that would integrate quantitative evidence from a variety of heterogeneous studies, harmonize different outcome measures, and yield strong statistical contrasts between solar and electrolysis approaches. These analysis processes can help guide evidence-based decisions on technology choices and highlight areas of research investment needs

III. METHODOLOGY

The research applied a systematic review and meta-analysis design in comparing the efficiency of solar and electrolysis technologies in producing green hydrogen. The study adhered to the Preferred Reporting Items for Systematic Reviews and Meta-Analyses (PRISMA) to maintain methodological soundness and transparency (Page et al., 2021).

A comparative effectiveness research strategy was taken to present evidence-based advice for technology choice in green hydrogen production.

Extensive literature searching was done in several electronic databases such as Web of Science, Scopus, PubMed, IEEE Xplore, and ScienceDirect. The search term used included the following keywords and Boolean operators:

- **Hydrogen production:** ("hydrogen production" OR "hydrogen generation" OR "H2 production")
- **Solar methods:** ("solar hydrogen" OR "photoelectrochemical" OR "PEC" OR "photovoltaic electrolysis" OR "PV electrolysis" OR "solar-to-hydrogen" OR "thermochemical water splitting")
- **Electrolysis methods:** ("water electrolysis" OR "electrolyzer" OR "alkaline electrolysis" OR "PEM electrolysis" OR "solid oxide electrolysis" OR "SOEC")
- **Green hydrogen:** ("green hydrogen" OR "renewable hydrogen" OR "clean hydrogen")
- **Performance metrics:** ("efficiency" OR "yield" OR "cost" OR "LCOH" OR "levelized cost")

The search was limited to peer-reviewed journal articles, conference proceedings, and technical reports published between 2015 and 2025 to capture recent technological developments while maintaining sufficient temporal scope. No language restrictions were initially applied, though non-English articles were excluded during screening if adequate translation resources were unavailable.

3.1 Inclusion Criteria:

Studies were included if they met the following criteria:

- **Technology focus:** Investigated solar-based or electrolysis-based hydrogen production methods
- **Quantitative data:** Reported numerical values for at least one primary outcome measure (efficiency, hydrogen yield, or LCOH)
- **Study type:** Experimental studies, modeling studies, techno-economic analyses, or technology demonstrations
- **Data quality:** Provided sufficient methodological detail to assess data reliability
- **Scope:** Focused on green hydrogen production using renewable energy sources

3.2 Exclusion Criteria:

Studies were excluded based on the following criteria:

- **Technology scope:** Fossil fuel-based hydrogen production, biological hydrogen production, or hybrid systems without clear renewable energy components
- **Data availability:** Review articles, editorials, or studies without extractable quantitative data
- **Study quality:** Studies with insufficient methodological detail or unclear measurement procedures
- **Scope limitations:** Studies focusing solely on catalyst development, materials research, or component-level analysis without system-level performance data

The study selection process was conducted in two phases. Initial screening involved review of titles and abstracts to identify potentially relevant studies. Full-text review was then performed for all studies passing initial screening, with inclusion decisions made based on the pre-established criteria.

A standardized data extraction form was developed to capture key study characteristics and outcome measures. The extraction framework included:

- Author information and publication year
- Study design and methodology
- Technology type and specifications
- Scale of operation (laboratory, pilot, industrial)
- Geographic location and context
- Outcome measures:
- Efficiency values and measurement basis
- Hydrogen yield data and units
- Cost information and economic parameters
- Experimental conditions and operational parameters

Given the diversity of measurement units and reporting conventions across studies, comprehensive data standardization procedures were implemented as under.

Efficiency standardization: All efficiency values were converted to percentage values on a consistent measurement basis. Solar efficiencies were primarily reported as solar-to-hydrogen conversion efficiency, while electrolysis efficiencies represented electrolyzer conversion efficiency.

Hydrogen yield standardization: Yield data were standardized to kilograms of hydrogen per day (kg/day) using the following conversion factors:

- Hydrogen density at standard temperature and pressure: 0.08988 kg/m³
- Temporal conversions: seconds/day (86,400), hours/day (24), days/year (365.25), days/month (30.44)
- Mass conversions: grams to kilograms (0.001), tons to kilograms (1,000)
- Cost standardization: All cost data were converted to United States dollars per kilogram of hydrogen (USD/kg) using:
- Currency conversion: EUR to USD rate of 1.10 (average rate for study period)
- Volume-to-mass conversion for hydrogen using standard density
- Studies reporting ranges or multiple values required standardized treatment:
- Range values: Midpoint calculation for ranges (e.g., "10-20%" converted to 15%)

- Multiple values: Arithmetic mean for multiple discrete values
- Approximations: Exact values extracted from approximate indicators (e.g., "~15%" converted to 15%)
- Upper/lower limits: Limit values used when ranges extended to infinity or zero

IV. STATISTICAL ANALYSIS

Comprehensive descriptive statistics were calculated for each outcome measure within technology categories, including measures of central tendency (mean, median), variability (standard deviation, variance), and distribution shape (range, interquartile range).

Prior to comparative analysis, statistical assumptions were evaluated:

- Normality assessment: Shapiro-Wilk tests conducted for sample sizes ≤ 50
- Variance homogeneity: Levene's test applied to assess equal variance assumptions
- Independence: Verified through study selection criteria ensuring non-overlapping datasets

Test selection followed a decision tree approach based on assumption testing results:

Parametric tests: Independent samples t-test for normally distributed data with equal variances; Welch's t-test for normally distributed data with unequal variances.

Non-parametric tests: Mann-Whitney U test used when normality or equal variance assumptions were debased.

Effect sizes were calculated to assess practical significance:

- Cohen's d: For parametric analyses
- Effect size r: For Mann-Whitney U tests, calculated as $r = |Z|/\sqrt{N}$
- Interpretation criteria: Small (≥ 0.1), medium (≥ 0.3), large (≥ 0.5) effects based on Cohen's conventions

4.1 Efficiency Comparison:

The efficiency assessment analysed standardized percentage values for 8 solar studies and 19 electrolysis studies (one descriptive entry excluded). Data extraction required careful standardization of various efficiency metrics, with solar studies typically reporting system-level solar-to-hydrogen conversion efficiency and electrolysis studies reporting electrolyser component efficiency.

- H01: No difference in mean efficiency between solar and electrolysis methods
- H11: There is a difference in mean efficiency between solar and electrolysis methods

TABLE 1
EFFICIENCY DATA
A) Solar Methods Efficiency Data (n = 8)

Sr. No	Paper	Original Value	Standardized (%)	Notes
1	Ahmad et al., 2025	14.20%	14.2	Single value
2	Li et al., 2023	10–20%	15	Range midpoint
3	Zhao & Yuan, 2023	18%	18	Single value
4	Tang et al., 2025	22.40%	22.4	Single value
5	Bozkurt & Yilmaz, 2025	36.09%, 18.43%	27.3	Average of both values
6	Peng et al., 2025	Up to 15%	15	Upper limit
7	Calnan et al., 2022	4–13%	8.5	Range midpoint
8	Tran et al., 2024	30–40%	35	Range midpoint

b) Electrolysis Methods Efficiency Data (n = 19)

Sr. No	Paper	Original Value	Standardized (%)	Notes
1	Zainal et al. (2024)	SOEC ~90%, PEM 60–70%	73.3	Average of ranges
2	Hassan et al. (2023)	3.68–4.84%	4.3	Range midpoint
3	Muhammad et al. (2024)	13.80%	13.8	Single value
4	Kumar (2024)	85–90%	87.5	Range midpoint
5	Shaban (2024)	82.20%	82.2	Single value
6	Khan (2018)	66%	66	Single value
7	Shudo (2023)	62%	62	Single value
8	Ghorbani (2024)	18.70%	18.7	Single value
9	Muhammad (2025)	62–82, 67–82, >80	74.6	Average of ranges
10	Selvam (2025)	70–80, 85–90	81.3	Average of ranges
11	Haile (2023)	76%	76	Single value
12	Hassan (2023)	18.7; >95; >95	69.6	Average (>95 as 95)
13	Abdelsalam (2024)	97.5; 89.3	93.4	Average
14	Zhou (2022)	15.1; 19; 65–90	34.7	Average
15	Meda (2023)	40–60; 17; 10; 17; 54	31.6	Average of values
16	Cheng (2023)	85; 85; 20.90; 22.40	53.3	Average of values
17	Dash (2024)	60–70%	65	Range midpoint
18	Gopinath (2022)	Multiple values	59	Average of values/ranges
19	Herdem (2024)	10.5; 30; 4	14.8	Average of values

Descriptive statistics revealed substantial differences between the two methods. Solar methods demonstrated a mean efficiency of 19.42% (SD = 7.92%, range: 8.5%-35.0%), while electrolysis methods showed significantly higher efficiency with a mean of 55.85% (SD = 26.92%, range: 4.3%-93.4%). The median values were 16.50% and 65.00% for solar and electrolysis methods, respectively.

TABLE 2
DESCRIPTIVE STATISTICS

Method	n	Mean (%)	Median (%)	SD (%)	Min (%)	Max (%)
Solar Methods	8	19.42	16.5	7.92	8.5	35
Electrolysis Methods	19	55.85	65	26.92	4.3	93.4
Difference (E – S)	–	36.43	48.5	–	–	–

Pre-test analysis using the Shapiro-Wilk test indicated normal distribution for the solar group ($p = 0.441$) but non-normal distribution for the electrolysis group ($p = 0.044$). Levene's test revealed significantly unequal variances ($F = 12.84$, $p = 0.001$), violating the assumptions for parametric testing. Consequently, the Mann-Whitney U test was selected as the appropriate non-parametric alternative.

- H02 - There is no significant difference in efficiency (%) between Solar Methods and Electrolysis Methods for hydrogen production.
- H12 - There is a significant difference in efficiency (%) between Solar Methods and Electrolysis Methods for hydrogen production.

Test Statistic	Value
U	17
Z	-3.21
p-value	0.001
Result	Statistically significant (reject H_0)
Effect Size (r)	0.62 (large effect)
Variance Explained	62%
Median Difference	~48.5 percentage points
Interpretation	Electrolysis methods showed significantly higher efficiency than Solar methods

The Mann-Whitney U test yielded statistically significant results ($U = 17.0$, $Z = -3.21$, $p = 0.001$), leading to rejection of the null hypothesis. The effect size was large ($r = 0.62$), indicating that 62% of the variance in efficiency rankings could be explained by the method type. Electrolysis methods demonstrated significantly higher efficiency values than solar methods, with a median difference of approximately 48.5 percentage points.

4.2 Hydrogen Yield Comparison:

The hydrogen yield analysis presented unique challenges due to extreme variability in measurement units and study scales. After comprehensive unit standardization to kg/day using hydrogen density conversions and temporal scaling factors, 9 solar studies and 11 electrolysis studies were included in the analysis.

TABLE 3
H2 YIELD DATA (Standardized to kg/day)
A) Solar Methods H2 Yield Data (n = 9)

Sr. No	Paper	Original Value	Original Unit	Standardized (kg/day)	Notes
1	Ahmad et al., 2025	Up to 420	g/day	0.42	Upper limit
2	Li et al., 2023	10,000	kg/day	10,000.00	Single value
3	Zhao & Yuan, 2023	0.047	L/min	0.006	Single value
4	Bozkurt & Yilmaz, 2025	0.0008368	kg/s	72.3	Single value
5	Calnan et al., 2022	Up to 200	mL/min	0.026	Upper limit
6	Tran et al., 2024	~40	mL/min	0.005	Approximate
7	Fopah-Lele et al., 2021	115	L/day	0.01	Single value
8	Abdollahi & Ranjbar, 2025	438	kg/h	10,512.00	Single value
9	Chowdhury et al., 2025	55,000	tons/year	150,581.79	Single value

B) Electrolysis Methods H2 Yield Data (n = 11)

Sr. No	Paper	Original Value	Original Unit	Standardized (kg/day)	Notes
1	Muhammad (2024)	101,000	kg/year	276.523	Single value
2	Abdelsalam (2024)	169,546	kg/year	464.192	Single value
3	Rejeb (2022)	0.75–1.2	tons/month	32.03	Range midpoint
4	Ahmad (2024)	18–28	mL/min	0.003	Range midpoint
5	Nazlıgül (2025)	12.5	L/h	0.027	Single value
6	Lin (2019)	2.1	L/h	0.005	Single value
7	Buddhi (2006)	8.3	L/h	0.018	Single value
8	Hibino (2017)	0.29	L/h	0.001	Single value
9	Fujiwara (2020)	2.4	L/h	0.005	Single value
10	Kongjui (2025)	36	tons/day	36,000.00	Single value
11	Hamdan (2025)	42	mL/min	0.005	Single value

The standardized data revealed extraordinary variability spanning 7-8 orders of magnitude within both method categories. Solar methods showed geometric mean yield of 5.42 kg/day (arithmetic mean: 19,018.51 kg/day, range: 0.005177-150,581.79 kg/day), while electrolysis methods demonstrated geometric mean yield of 0.37 kg/day (arithmetic mean: 3,342.98 kg/day, range: 0.000626-36,000.00 kg/day).

TABLE 4
H2 YIELD DESCRIPTIVE STATISTICS AND SCALE CLASSIFICATION

Method	n	Arithmetic Mean	Median	Geometric Mean	Min	Max
Solar Methods	9	19,018.51	0.42	5.422005	0.00518	150,581.79
Electrolysis Methods	11	3,342.98	0.0179	0.368425	0.00063	36,000.00
Geometric Mean Ratio (Solar / Electrolysis)	–	–	–	14.72	–	–

The extreme variability necessitated log-transformation for meaningful analysis. Log₁₀-transformed data showed solar methods with mean = 0.734 (SD = 2.874) and electrolysis methods with mean = -0.434 (SD = 2.559). Scale classification revealed that study scope (laboratory vs. pilot vs. industrial) was a major contributor to variability, with industrial-scale studies heavily influencing the geometric mean differences.

Log10-Transformed Statistics:

Method	n	Mean (Log10)	Median (Log10)	SD (Log10)
Solar Methods	9	0.734	-0.377	2.874
Electrolysis Methods	11	-0.434	-1.747	2.559

Data Range Analysis:

Method	n	Range (Orders of Magnitude)
Solar Methods	9	7.5 orders
Electrolysis Methods	11	7.8 orders

To evaluate whether hydrogen production capacities differ meaningfully between Solar and Electrolysis methods, a Mann-Whitney U test was chosen. This non-parametric test is appropriate because the production data span several orders of magnitude, are highly skewed, and include heterogeneous measurement scales across studies. It allows comparison of the two independent groups (Solar vs. Electrolysis) without assuming normality.

- H03: There is no significant difference in hydrogen production capacity (kg/day, log-transformed) between Solar Methods and Electrolysis Methods.
- H13: There is a significant difference in hydrogen production capacity (kg/day, log-transformed) between Solar Methods and Electrolysis Methods.

Mann-Whitney U Test Results

Test Statistic	Value
Solar rank sum	110
Electrolysis rank sum	100
U statistic	34
Z-score	-1.178
p-value	> 0.05
Effect size (r)	0.263
Effect interpretation	Small
Statistical result	Not Significant

Mann-Whitney U test results showed no statistically significant difference between methods ($U = 34$, $Z = -1.178$, $p > 0.05$), despite the 14.72-fold higher geometric mean for solar methods. The effect size was small ($r = 0.263$), and the lack of significance was attributed to the extreme within-group variability rather than absence of a true difference. This finding suggests that study scale and implementation context have greater impact on hydrogen yield than the fundamental technology choice.

4.3 Levelized Cost of Hydrogen (LCOH) Comparison:

The LCOH analysis required comprehensive currency standardization to USD/kg using a EUR-to-USD conversion rate of 1.10, along with unit conversions for volume-based measurements. After excluding studies with insufficient quantitative data, 8 solar studies and 10 electrolysis studies were retained for analysis.

TABLE 5
LCOH DATA (Standardized to USD/kg)
A) Solar Methods LCOH Data (n = 8 usable)

Sr. No	Paper	Original Value	Original Unit	Standardized (USD/kg)	Notes
1	Ahmed Al Makky et al., 2025	5.67	\$/kg-H ₂	5.67	Single value
2	Vartiainen et al., 2022	1.0–2.7 (2020)	€/kg-H ₂	2.04	2020 range midpoint ×1.10
3	Tang et al., 2025	Case-dependent values	\$/kg-H ₂	Excluded	Too vague
4	Chowdhury et al., 2025	Country-dependent	\$/kg-H ₂	Excluded	Too vague
5	Chahtou & Taoussi, 2025	2.12–2.72	USD/kg-H ₂	2.42	Range midpoint
6	Muhammad et al., 2025	SOEC:7.86, PEM:13.07, AEC:14.44	USD/kg-H ₂	11.79	Average of 3 values
7	Ghosh, 2025	3.7–6.2	€/kg-H ₂	5.45	Literature range ×1.10
8	Fopah-Lele et al., 2021	1.09	€/m ³ H ₂	13.34	H ₂ density conversion ×1.10
9	Ayodele et al., 2021	16.52, 15.95, 15.67	USD/kg-H ₂	16.05	Average of 3 values
10	Priyanka Saha et al., 2024	3–12	USD/kg-H ₂	7.5	Range midpoint

B) Electrolysis Methods LCOH Data (n = 10 usable)

Sr. No	Paper	Original Value	Original Unit	Standardized (USD/kg)	Notes
1	Abdelsalam, 2024	6.78	USD/kg	6.78	Single value
2	Rejeb, 2022	3.5–5.2	USD/kg	4.35	Range midpoint
3	Ikuerowo, 2024	3.8–6.2	USD/kg	5	Range midpoint
4	Travaglini, 2025	3.5–5.5	EUR/kg	4.95	Range midpoint ×1.10
5	Muhammad, 2025	4.1–5.7, 4.3–6.0, 3.9–5.2	USD/kg	4.9	Average of 3 ranges
6	Selvam, 2025	3.2–7.1	USD/kg	5.15	Range midpoint
7	Koj, 2024	3.9–5.8	EUR/kg	5.33	Range midpoint ×1.10
8	Rivera-Tinoco, 2008	5.6	EUR/kg	6.16	Single value ×1.10
9	Stiber, 2024	3.0–4.5	EUR/kg	4.13	Range midpoint ×1.10
10	Kongjui, 2025	4.2	USD/kg	4.2	Single value

TABLE 6
LCOH DATA WITH CURRENCY STANDARDIZATION

Method	n	Mean	Median	SD	Min	Max	Variance
Solar Methods	8	8.03	6.58	5.2	2.04	16.1	26.64
Electrolysis Methods	10	5.09	4.97	0.8	4.13	6.78	0.71
Difference (S – E)	–	+2.94 (57.8% ↑)	+1.61	–	–	–	–

Solar methods demonstrated higher average costs (\$8.03/kg, SD = \$5.16, range: \$2.04-\$16.05) compared to electrolysis methods (\$5.09/kg, SD = \$0.84, range: \$4.13-\$6.78). The cost difference of \$2.94/kg represented a 57.8% higher cost for solar methods. Notably, electrolysis methods showed remarkably consistent costs with 6.1× lower variability than solar methods.

TABLE 7
LCOH DESCRIPTIVE STATISTICS (USD/kg)

Method	n	Mean	Median	SD	Min	Max	Variance
Solar Methods	8	8.03	6.58	5.16	2.04	16.05	26.64
Electrolysis Methods	10	5.09	4.97	0.84	4.13	6.78	0.71
Difference (Solar – Electrolysis)	–	2.94	1.61	–	–	–	–
(Percent difference)		(57.8% higher)		–	–	–	–

TABLE 8
LCOH STATISTICAL ANALYSIS RESULTS

Test Component	Value
Test Used	Mann-Whitney U
Assumptions Met	No (non-normal, unequal variance)
Solar rank sum	92
Electrolysis rank sum	79
U statistic	24
Z-score	-1.422
p-value	< 0.10
$\alpha = 0.05$ result	Not Significant
$\alpha = 0.10$ result	Marginally Significant
Effect size (r)	0.335
Effect interpretation	Medium

Test	Solar (n=8)	Electrolysis (n=10)
Normality (Shapiro-W)	$W \approx 0.807, p < 0.01 \rightarrow$ Non-normal	$W \approx 0.862, p < 0.05 \rightarrow$ Questionable
Equal Variances	Variance = 26.64	Variance = 0.71
Variance Ratio (F)	$F = 37.55 \rightarrow$ Severely Violated	–

Assumption testing revealed non-normal distributions for both groups and severely unequal variances (F-ratio = 37.55), necessitating the Mann-Whitney U test. The analysis yielded marginally significant results ($U = 24, Z = -1.422, p < 0.10$) with a medium effect size ($r = 0.335$). While not reaching statistical significance at the conventional $\alpha = 0.05$ level, the results suggested a meaningful practical difference in cost structures.

Cost Range	Solar (n=8)	Solar %	Electrolysis (n=10)	Electro %
Low Cost (< \$5/kg)	3	37.50%	7	70%
Medium Cost (\$5–10/kg)	3	37.50%	3	30%
High Cost (> \$10/kg)	2	25%	0	0%

Cost distribution analysis revealed that 70% of electrolysis studies reported costs below \$5/kg, compared to only 37.5% of solar studies. Conversely, 25% of solar studies exceeded \$10/kg, while no electrolysis studies reached this threshold. This pattern indicates that electrolysis methods provide more predictable and generally lower costs for hydrogen production. While the Mann-Whitney U test did not reach conventional statistical significance ($\alpha = 0.05$), the medium effect size and cost distribution patterns indicate a practical difference between methods. Electrolysis methods tend to deliver more predictable and generally lower hydrogen costs, whereas solar methods show wider variability, with a notable proportion of studies exceeding \$10/kg.

4.4 Comparative Market Analysis:

TABLE 9
MARKET COMPETITIVENESS COMPARISON

Hydrogen Type	Cost Range
Gray H ₂ (fossil)	\$1 – 2/kg
Blue H ₂ (with CCS)	\$2 – 3/kg
Target Green H ₂	\$2 – 4/kg
Current Electrolysis	\$4.13 – 6.78/kg
Current Solar	\$2.04 – 16.05/kg

When evaluated against conventional hydrogen production costs (gray hydrogen: \$1-2/kg, blue hydrogen: \$2-3/kg), both green hydrogen methods remain above competitive thresholds. However, electrolysis methods cluster closer to the target range of \$2-4/kg for commercial viability. Solar methods showed both the lowest individual study cost (\$2.04/kg) and highest variability, suggesting technology- and implementation-dependent performance.

4.5 Statistical Power and Limitations:

Power analyses indicated adequate sample sizes for detecting large effects but limited power for small to medium effects. The efficiency comparison, with its large effect size ($r = 0.62$), demonstrated sufficient power for reliable conclusions. The yield comparison's small effect size ($r = 0.263$) combined with extreme variability limited statistical power, while the LCOH comparison's medium effect size ($r = 0.335$) suggested that larger sample sizes might achieve statistical significance.

Several limitations affected the interpretation of results. Different measurement contexts between solar (often system-level) and electrolysis (often component-level) efficiency metrics may explain the large efficiency differences. The extreme variability in yield data reflected studies spanning laboratory to industrial scales, suggesting that scale effects overshadow technology differences. LCOH variations were influenced by geographic, economic, and temporal factors affecting cost structures.

4.6 Synthesis of Findings:

The meta-analysis revealed distinct performance profiles for solar and electrolysis methods. Electrolysis methods consistently demonstrated higher efficiency, more predictable costs, and performance suitable for commercial deployment. Solar methods showed greater variability across all metrics, with potential for both very competitive and very expensive implementations.

TABLE 10
OVERALL COMPARISON SUMMARY MATRIX

Variable	Solar vs Electrolysis	Result	Key Insight
Efficiency	19.4% vs 55.8%	Electrolysis significantly higher	Different measurement contexts
H2 Yield	5.42 vs 0.37 kg/day (geometric means)	No significant difference	Scale matters more than technology
LCOH	\$8.03 vs \$5.09/kg	Marginally significant (electrolysis lower)	Electrolysis more consistent & affordable

Effect sizes progressed from large (efficiency) to small (yield) to medium (cost), suggesting that the choice between methods has strongest implications for conversion efficiency, moderate implications for cost, and limited implications for absolute yield capacity. The results imply that both technologies are equally useful for green hydrogen production, with the choice typically contingent on particular application need, scale, and risk appetite rather than qualitative technological superiority.

V. DISCUSSION

The meta-analysis results show a multifaceted environment of green hydrogen production technologies with unique performance profiles that undercut simplistic technology selection strategies. The substantial efficiency benefit shown for electrolysis technologies (55.8% compared to 19.4%) conforms to theoretical predictions but must be interpreted with caution in light of the essential differences in measurement contexts between the two technologies.

The superior efficiency of electrolysis processes is in line with separate research works by Kumar (2024) and Shaban (2024), who gave the efficiencies of optimized systems as 85-90% and 82.2%, respectively. Yet, the high effect size ($r = 0.62$) found in this meta-analysis might overestimate the practical relevance because of the inherent measurement discrepancy: solar experiments commonly report full system-level solar-to-hydrogen conversion efficiency, whereas electrolysis experiments commonly measure electrolyzer component efficiency without including upstream renewable electricity generation losses.

The lack of statistically significant differences in hydrogen yield, though solar methods had 14.72 times greater geometric mean, is one of the most surprising observations of this analysis. This finding contradicts the expectations derived from individual high-performing studies like Li et al. (2023) for 10,000 kg/day and Chowdhury et al. (2025) for 55,000 tons/year for large-scale solar systems. The extreme within-group variability spanning 7-8 orders of magnitude suggests that deployment scale, rather than fundamental technology characteristics, drives yield performance.

The LCOH findings showing marginally significant cost advantages for electrolysis (\$5.09 vs \$8.03/kg) diverge from some optimistic projections in the solar hydrogen literature. Vartiainen et al. (2022) projected future solar hydrogen costs as low as €0.3-0.9/kg (\$0.33-0.99/kg) by 2050, while our analysis found current solar costs ranging from \$2.04-16.05/kg. This discrepancy highlights the gap between theoretical potential and demonstrated performance, suggesting that projected cost reductions may require significant technological breakthroughs or deployment at unprecedented scales.

The cost consistency advantage of electrolysis methods identified in this meta-analysis corroborates findings from individual techno-economic studies. Muhammad et al. (2025) reported relatively narrow LCOH ranges of \$4.1-5.7/kg across different electrolysis technologies (AEC, PEM, SOEC), while Selvam (2025) found similar consistency at \$3.2-7.1/kg. This contrasts sharply with solar studies showing extreme cost variability, from highly competitive results by Chahtou & Taoussi (2025) at \$2.12-2.72/kg to expensive implementations by Ayodele et al. (2021) at \$15.67-16.52/kg.

The efficiency patterns observed in the meta-analysis align with theoretical expectations from electrochemical and photochemical literature. Electrolysis studies consistently report high conversion efficiencies, with Abdelsalam (2024) achieving 97.5% Faradaic efficiency and Hassan (2023) reporting >95% electrolyzer efficiency. Solar efficiency results show greater diversity, ranging from modest performance by Hassan et al. (2023) at 3.68-4.84% for PV-electrolysis systems to exceptional results by Tran et al. (2024) reporting 30-40% theoretical efficiency for thermochemical approaches.

The most unexpected finding was the lack of statistical significance in hydrogen yield comparisons despite substantial differences in geometric means. This result challenges the conventional wisdom that technology selection significantly impacts production capacity and suggests that operational factors such as plant scale, capacity utilization, and system integration may be more important determinants of actual hydrogen output than the fundamental production technology.

The moderate effect size for LCOH differences ($r = 0.335$) was surprising given the substantial mean difference (\$2.94/kg). This finding indicates that while electrolysis tends toward lower costs, considerable overlap exists between the cost distributions of both technologies, suggesting that site-specific factors, technology optimization, and implementation quality may be more influential than technology category alone.

The large efficiency effect size ($r = 0.62$) exceeded expectations based on individual study comparisons, possibly reflecting systematic measurement bias where solar studies report more conservative system-level efficiencies while electrolysis studies focus on optimized component performance. This measurement discrepancy has important implications for technology benchmarking and suggests the need for standardized efficiency reporting protocols.

Scale and Context Dependencies

The analysis showed that study scale has a great impact on performance results in all observed variables. Small-scale laboratory studies like Zhao & Yuan (2023) with 0.047 L/min hydrogen yield and Ahmad (2024) with 18-28 mL/min illustrate the difficulties in extrapolating small-scale findings to industrial applications. Industrial-scale estimates, on the other hand, by Kongjui (2025) at 36 tons/day and Abdollahi & Ranjbar (2025) at 438 kg/h reflect the possibility of large scale economies.

The geographical setting also seems to play a role, with research from various places presenting systematic variations in cost. Middle Eastern research by Abdelsalam (2024) and Ahmed Al Makky et al. (2025) presented LCOH values of \$6.78/kg and \$5.67/kg respectively, whereas European research by Vartiainen et al. (2022) estimated lower long-term costs, indicating regional variations in solar resources, electricity prices, and economic situations greatly affect technology competitiveness.

VI. CONCLUSION

This 47-study meta-analysis presents thorough evidence resolving the comparative effectiveness of solar and electrolysis approaches to green hydrogen production in terms of efficiency, yield, and cost.

Research Question 1 revealed statistically significant efficiency differences, with electrolysis methods demonstrating superior performance (55.8% vs 19.4% mean efficiency, large effect size $r = 0.62$). However, measurement context differences between system-level solar and component-level electrolysis efficiency may partially explain this substantial gap.

Research Question 2 showed no statistically significant yield differences despite solar methods achieving 14.72 times higher geometric mean yield (5.42 vs 0.37 kg/day). The extreme variability spanning 7-8 orders of magnitude indicated that study scale and implementation context impact yield more than technology choice.

Research Question 3 revealed marginally significant cost differences ($p < 0.10$, medium effect $r = 0.335$), with electrolysis providing more consistent and lower costs (\$5.09 \pm \$0.84/kg) compared to solar methods (\$8.03 \pm \$5.16/kg). Electrolysis

demonstrated 57.8% cost advantage with 6.1 times lower variability, indicating superior affordability and investment predictability.

LIMITATIONS

The review was limited to English-language publications from 2015-2025, potentially excluding relevant research from non-English regions. Publication bias may over-represent breakthrough results, particularly for emerging solar technologies. Geographic bias toward North America, Europe, and East Asia studies limits global applicability. The rapidly evolving field may render current performance benchmarks quickly outdated, while limited long-term operational data, especially for solar systems, constrains durability assessments.

The measurement context differences between solar and electrolysis efficiency studies represent a fundamental limitation affecting the interpretation of efficiency comparisons. The extreme yield variability observed across studies reflects not only technological differences but also varying assumptions about capacity factors, operational availability, and system integration. This variability limits the ability to draw definitive conclusions about inherent yield advantages and suggests that site-specific feasibility studies may be more informative than technology-level generalizations.

PRACTICAL IMPLICATIONS

The meta-analysis findings have significant implications for policy support and investment strategies in green hydrogen development. The demonstrated cost and performance consistency of electrolysis methods suggests they may be more suitable for near-term deployment programs requiring predictable outcomes and bankable projects. Policy measures in favor of electrolysis deployment may be directed to scale-up incentives and renewable electricity integration.

Solar hydrogen policy support might demand other strategies, considering the greater variability in performance and context dependence found in the analysis. Support for individual solar hydrogen strategies with competitive performance, like low-cost outcomes by Chahtou & Taoussi (2025), could be more effective than generalized technology-neutral incentives.

SCOPE FOR FUTURE RESEARCH

Important research gaps are long-term durability testing of solar hydrogen systems and cost reduction measures for electrolysis by manufacturing scale-up. Streamlined techno-economic evaluation frameworks facilitating straightforward cross-technology comparison are highly desirable.

Future work must formulate standardized measures of efficiency that allow for equitable comparison between technologies, possibly including full lifecycle efficiency accounting that accounts for upstream energy conversion losses in both methodologies.

This meta-analysis determines that solar and electrolysis technologies present promising avenues with differing strengths: electrolysis promises better consistency and readiness for the commercial stage, whereas solar technologies maintain breakthrough potential under ideal circumstances. The results indicate diversification of a technology portfolio can maximize deployment of clean hydrogen in diverse global settings. As the globe speeds toward net-zero ambitions, these relative insights can guide informed technology investment and policy decisions that maximize scarce resources while promoting sustainable energy transformation.

REFERENCES

- [1] Abdelsalam, E. (2024). Solar chimney power plant-driven electrolyzer for green hydrogen production: A techno-economic analysis. *International Journal of Hydrogen Energy*, 49, 123-135.
- [2] Ahmad, S., Kumar, R., & Patel, N. (2025). Bifacial photovoltaic-electrolyzer systems for enhanced hydrogen production: Experimental analysis with reflective coatings. *Renewable Energy*, 195, 245-258.
- [3] Ahmad, M., Hassan, A., & Ali, K. (2024). Experimental investigation of dual electrolyte configuration for improved alkaline water electrolysis efficiency. *Energy Conversion and Management*, 285, 117045.
- [4] Ahmed Al Makky, A., Rahman, S., & Thompson, L. (2025). HOMER Pro simulation of renewable hydrogen production systems: A case study from Oman. *Sustainable Energy Technologies and Assessments*, 58, 103251.
- [5] Alstrum-Acevedo, J. H., Brennaman, M. K., & Meyer, T. J. (2005). Chemical approaches to artificial photosynthesis. *Inorganic Chemistry*, 44(19), 6802-6827.
- [6] Armaroli, N., & Barbieri, A. (2021). The hydrogen dilemma in Italy's energy transition. *Nature Italy*, 1, 109-113. <https://www.nature.com/articles/d43978-021-00109-3>

- [7] Atak, S., Yilmaz, M., & Ozkan, T. (2024). Advanced photoelectrochemical systems for solar hydrogen production: Materials and performance optimization. *Solar Energy Materials and Solar Cells*, 258, 112394.
- [8] Awad, M., Said, A., Saad, M. H., Farouk, A., Mahmoud, M. M., Alshammari, M. S., Alghaythi, M. L., Aleem, S. H. A., Abdelaziz, A. Y., & Omar, A. I. (2024). A review of water electrolysis for green hydrogen generation considering: PV/wind/hybrid/hydropower/geothermal/tidal and wave/biogas energy systems, economic analysis, and its application. *Alexandria Engineering Journal*, 87, 213-239.
- [9] Ayodele, T. R., Munda, J. L., & Agee, J. T. (2021). Techno-economic assessment of photovoltaic-powered hydrogen refueling stations in South Africa. *International Journal of Hydrogen Energy*, 46(35), 18326-18338.
- [10] Ban, Y., Li, H., Wang, X., & Zhang, Q. (2025). High-efficiency photocatalytic water splitting for hydrogen production: Recent advances in material design. *Applied Catalysis B: Environmental*, 325, 122384.
- [11] Bhandari, R., Trudewind, C. A., & Zapp, P. (2014). Life cycle assessment of hydrogen production via electrolysis: A review. *Journal of Cleaner Production*, 85, 151-163.
- [12] Bozkurt, I., & Yilmaz, C. (2025). Thermodynamic analysis of parabolic dish solar collector integrated multi-generation system for hydrogen production. *Energy*, 289, 129934.
- [13] Buddhi, D., Kothari, S., & Sawhney, R. L. (2006). A comparative study of water electrolysis using different electrolytes. *International Journal of Hydrogen Energy*, 31(11), 1514-1519.
- [14] Buttlar, A., & Spliethoff, H. (2018). Current status of water electrolysis for energy storage, grid balancing, and sector coupling via power-to-gas and power-to-liquids: A review. *Renewable and Sustainable Energy Reviews*, 82, 2440-2454.
- [15] Calnan, S., Weiss, M., & Rech, S. (2022). Outdoor testing of photovoltaic-electrolyzer systems: Performance analysis and scale-up considerations. *Progress in Photovoltaics*, 30(8), 891-905.
- [16] Chahtou, A., & Taoussi, M. (2025). Techno-economic analysis of integrated photovoltaic-desalination-electrolysis systems for green hydrogen production. *Desalination*, 548, 116285.
- [17] Cheng, L., Wang, H., & Zhou, Y. (2023). Technoeconomic modeling of renewable hydrogen production systems: Cost optimization and sensitivity analysis. *Applied Energy*, 328, 120156.
- [18] Chiroșcă, A. M., Rusu, E., & Minzu, V. (2024). Green hydrogen: Production and storage methods—Current status and future directions. *Energies*, 17(23), 5820. <https://doi.org/10.3390/en17235820>
- [19] Chowdhury, N., Rahman, A., & Hasan, M. (2025). Renewable hydrogen potential assessment across South Asian countries: A techno-economic modeling approach. *Renewable Energy*, 201, 345-362.
- [20] Dash, S. K., Chakraborty, S., & Elangovan, D. (2024). Performance analysis of alkaline water electrolysis systems: A comprehensive review of efficiency ranges. *International Journal of Hydrogen Energy*, 49(12), 567-583.
- [21] Dincer, I., & Acar, C. (2015). Review and evaluation of hydrogen production methods for better sustainability. *International Journal of Hydrogen Energy*, 40(34), 11094-11111. <http://dx.doi.org/10.1016/j.ijhydene.2014.12.035>
- [22] Domenech, T., Amaris, H., & Alonso, M. (2021). Comparative analysis of electrolysis technologies for offshore hydrogen production: Technical and economic assessment. *Renewable Energy*, 167, 752-768.
- [23] Endo, N., Goshome, K., & Tetsuka, H. (2016). Silicon-based photoelectrochemical hydrogen production: Advances in electrode design and system integration. *Journal of Materials Chemistry A*, 4(16), 5914-5924.
- [24] Fopah-Lele, A., Tamba, J. G., & Ndi, K. S. (2021). A comprehensive techno-economic analysis of PV-electrolyzer system in Benin: Validated with MATLAB-Simulink modeling. *International Journal of Hydrogen Energy*, 46(67), 33558-33573.
- [25] Fujiwara, K., Okamura, T., & Nishiki, Y. (2020). Steam electrolysis cell performance at elevated temperatures: Efficiency and durability considerations. *Electrochimica Acta*, 362, 137145.
- [26] Ghorbani, B., Shirmohammadi, R., & Romeo, L. M. (2024). Experimental and simulation-based analysis of photovoltaic-SEPIC-electrolyzer systems for solar-to-hydrogen conversion. *Solar Energy*, 243, 45-58.
- [27] Ghosh, A. (2025). Review of photovoltaic-electrolyzer systems: Performance analysis of floating PV, agrivoltaic, and BIPV configurations. *Renewable and Sustainable Energy Reviews*, 171, 113045.
- [28] Gondal, I. A., Masood, S. A., & Khan, R. (2018). Green hydrogen production potential for developing a hydrogen economy in Pakistan. *International Journal of Hydrogen Energy*, 43(12), 6011-6039.
- [29] Gopinath, S., Saravanan, A., & Kumar, P. S. (2022). Literature-based performance indicators for renewable-to-hydrogen conversion systems: A comprehensive analysis. *Journal of Cleaner Production*, 345, 131156.
- [30] Haile, A., Geleta, T. N., & de Kleine, R. (2023). Steam-assisted electrolysis cell efficiency analysis: Experimental validation and performance optimization. *International Journal of Hydrogen Energy*, 48(45), 17234-17247.
- [31] Hamdan, M., Abdel-Fattah, T., & Qandil, H. (2025). Enhanced aluminum electrode performance for water electrolysis using micro-arc oxidation and nanoparticle treatments. *Electrochimica Acta*, 439, 141654.
- [32] Hassan, Q., Azzawi, I. D., Sameen, A. Z., & Salman, H. M. (2023). Hydrogen production via water electrolysis: A comprehensive review of technologies and performance indicators. *International Journal of Thermofluids*, 18, 100328.
- [33] Herdem, M. S., Mazzeo, D., Matera, N., Wen, J. Z., Nathwani, J., & Hong, Z. (2024). Performance indicators and energy conversion efficiency analysis for renewable hydrogen production systems. *Applied Energy*, 335, 120745.
- [34] Hibino, T., Kobayashi, K., & Nagao, M. (2017). High-temperature PtFe/C catalyst performance in phosphoric acid electrolyte for enhanced hydrogen production. *Journal of Power Sources*, 342, 108-115.
- [35] Hydrogen Council. (2023). *Hydrogen insights 2023: A perspective on hydrogen investment, deployment and cost competitiveness*. Hydrogen Council.

- [36] Hydrogen Council. (2024). *Global hydrogen investment tracker: Market developments and policy analysis*. Hydrogen Council.
- [37] Ikuerowo, T. A., Okafor, I. S., & Dara, J. O. (2024). Literature-based techno-economic review of green hydrogen production: Cost analysis and market perspectives. *International Journal of Hydrogen Energy*, 51, 245-263.
- [38] International Energy Agency. (2019). *The future of hydrogen: Seizing today's opportunities*. IEA Publications.
- [39] International Energy Agency. (2022). *Global hydrogen review 2022*. IEA Publications. <https://www.iea.org/reports/global-hydrogen-review-2022>
- [40] International Energy Agency. (2023). *Global hydrogen review 2023*. IEA Publications. <https://www.iea.org/reports/global-hydrogen-review-2023>
- [41] International Renewable Energy Agency. (2019). *Hydrogen: A renewable energy perspective*. IRENA Publications.
- [42] International Renewable Energy Agency. (2020). *Green hydrogen: A guide to policy making*. IRENA Publications. <https://www.irena.org/>
- [43] International Renewable Energy Agency. (2023). *Renewable power generation costs in 2022*. IRENA Publications. <https://www.irena.org/Publications/2023/Aug/Renewable-Power-Generation-Costs-in-2022>
- [44] Islam, A., Islam, T., Mahmud, H., Raihan, O., Islam, S., Marwani, H. M., Rahman, M. M., Asiri, A. M., Hasan, M., Hasan, N., Alghamdi, M. T., Hossain, M. K., & Uddin, J. (2024). Accelerating the green hydrogen revolution: A comprehensive analysis of technological advancements and policy interventions. *International Journal of Hydrogen Energy*, 67, 458-486.
- [45] Jiménez-Calvo, P., Marcilla, R., & Quartarone, E. (2024). Photocatalytic water splitting: Laboratory-scale reports and theoretical efficiency analysis. *ChemSusChem*, 17(2), e202301456.
- [46] Ji, M., Wang, J., & Li, X. (2021). Life cycle assessment-based comparative analysis of hydrogen production methods: SMR, electrolysis, and emerging technologies. *Applied Energy*, 295, 117034.
- [47] Kakoulaki, G., Kougias, I., Taylor, N., Dolci, F., Moya, J., & Jäger-Waldau, A. (2021). Green hydrogen in Europe: A regional assessment of substituting existing production with electrolysis powered by renewables. *Energy Conversion and Management*, 228, 113649.
- [48] Kar, S. K., Harichandan, S., & Roy, B. (2022). Bibliometric analysis of the research on hydrogen economy: An analysis of current findings and roadmap ahead. *International Journal of Hydrogen Energy*, 47(18), 10803-10824. <https://doi.org/10.1016/j.ijhydene.2022.01.137>
- [49] Kazemi Asfeh, R., Mohammadi, A., & Rezaei, M. (2024). Advanced photoelectrochemical systems for solar water splitting: Recent progress and future directions. *Solar Energy Materials and Solar Cells*, 261, 112524.
- [50] Khan, M. A., Zafar, S., & Rashid, N. (2018). Experimental analysis of alkaline water electrolysis powered by solar photovoltaic systems. *Renewable Energy*, 125, 742-750.
- [51] Koj, J. C., Wulf, C., Schreiber, A., Zapp, P., & Schott, P. (2024). Life cycle cost and life cycle assessment modeling for alkaline, PEM, and SOEC electrolysis technologies. *Applied Energy*, 356, 122384.
- [52] Kongjui, T., Therdthianwong, S., & Therdthianwong, A. (2025). Economic analysis of large-scale electrolysis systems: 114-module configuration for industrial hydrogen production. *International Journal of Hydrogen Energy*, 50, 456-469.
- [53] Kovač, A., Paranos, M., & Marcius, D. (2021). Hydrogen in energy transition: A review. *International Journal of Hydrogen Energy*, 46(16), 10016-10035.
- [54] Kourougianni, F., Arsalis, A., Olympios, A. V., Yiasoumas, G., Konstantinou, C., Papanastasiou, P., & Georghiou, G. E. (2024). A comprehensive review of green hydrogen energy systems. *Renewable Energy*, 220, 119655. <https://doi.org/10.1016/j.renene.2024.120911>
- [55] Kumar, S. S., & Lee, H. (2022). An overview of water electrolysis technologies for green hydrogen production. *Energy Reports*, 8, 13793-13813.
- [56] Kumar, A. (2024). Literature review and experimental analysis of solid oxide electrolysis cell performance characteristics. *International Journal of Hydrogen Energy*, 49(8), 334-348.
- [57] Lemus, R. G., & Duarte, J. M. M. (2010). Updated hydrogen production costs and parities for conventional and renewable technologies. *International Journal of Hydrogen Energy*, 35(9), 3929-3936.
- [58] Li, X., Zhang, H., & Wang, Y. (2023). Modeling and performance analysis of photoelectrochemical and photovoltaic-electrolysis scale-up potential. *Applied Energy*, 342, 121156.
- [59] Lin, Y. H., Chiu, C. W., & Lee, C. Y. (2019). Proton exchange membrane electrolysis using 1M KOH and 1M H₂SO₄: Performance comparison and optimization. *Electrochimica Acta*, 298, 175-184.
- [60] Lodhi, M. A. K. (1987). Hydrogen production from renewable sources of energy. *International Journal of Hydrogen Energy*, 12(7), 461-568.
- [61] Lodhi, M. A. K. (2004). Helio-hydro and helio-thermal production of hydrogen. *International Journal of Hydrogen Energy*, 29(11), 1099-1113.
- [62] Maestre, V. M., Ortiz, A., & Ortiz, I. (2021). Challenges and prospects of renewable hydrogen-based strategies for full decarbonization of stationary power applications. *Renewable and Sustainable Energy Reviews*, 152, 111628. <https://doi.org/10.1016/j.rser.2021.111628>
- [63] Maka, A. O. M., & Ghalut, T. (2025). Literature review compilation of solar-to-hydrogen efficiency values for photovoltaic-electrolysis systems. *Solar Energy*, 234, 234-248.

- [64] Marouani, I., Guesmi, T., Alshammari, B. M., Alqunun, K., Alzamil, A., Alturki, M., & Hadj Abdallah, H. (2023). Integration of renewable energy-based green hydrogen into the energy future. *Processes*, 11(9), 2685.
- [65] McKinsey & Company. (2021). *Hydrogen economy outlook: Key opportunities and challenges ahead*. McKinsey & Company.
- [66] Meda, L. (2023). Literature review of efficiency values for regenerative fuel cells, PV+PEM systems, solar thermophotovoltaic, and SOEC technologies. *Fuel Cells*, 23(4), 187-198.
- [67] Miltner, A., Wukovitz, W., Pröll, T., & Friedl, A. (2010). Renewable hydrogen production: A technical evaluation based on process simulation. *Journal of Cleaner Production*, 18(1), 51-62.
- [68] Mostafa, E. S. (2023). Hydrogen production by water electrolysis technologies: A review. *Results in Engineering*, 20, 101426.
- [69] Muhammad, H. A., Lee, B. C., Kumar, P. S., Ahmad, A., Nghiem, L. D., Mahlia, T. M. I., & Alam, J. (2024). Solar-to-hydrogen efficiency analysis of concentrated solar power-solid oxide electrolysis system: Model validation through experimental data. *Applied Energy*, 350, 121745.
- [70] Muhammad, H. A., Rezk, H., Maghrabie, H. M., Alsharif, A., & Ahmad, A. (2025). Techno-economic modeling of concentrated solar power integrated with different electrolyzer technologies: Western Australia case study. *Energy Conversion and Management*, 286, 117645.
- [71] National Renewable Energy Laboratory. (1995). *The Green Hydrogen Report*. NREL Publications.
- [72] Nazlıgül, T., Kavak, N., & Baykara, S. Z. (2025). Performance analysis of photovoltaic-SEPIC-NiCoMo electrolyzer system for solar hydrogen production. *International Journal of Hydrogen Energy*, 50, 789-801.
- [73] Oliveira, A. M., Beswick, R. R., & Yan, Y. (2021). A green hydrogen economy for a renewable energy society. *Current Opinion in Chemical Engineering*, 33, 100701.
- [74] Østergaard, P. A., Duic, N., Noorollahi, Y., Mikulcic, H., & Kalogirou, S. (2020). Sustainable development using renewable energy technology. *Renewable Energy*, 146, 2430-2437. <https://doi.org/10.1016/j.renene.2019.08.094>
- [75] Page, M. J., McKenzie, J. E., Bossuyt, P. M., Boutron, I., Hoffmann, T. C., Mulrow, C. D., Shamseer, L., Tetzlaff, J. M., Akl, E. A., Brennan, S. E., Chou, R., Glanville, J., Grimshaw, J. M., Hróbjartsson, A., Lalu, M. M., Li, T., Loder, E. W., Mayo-Wilson, E., McDonald, S., ... Moher, D. (2021). The PRISMA 2020 statement: An updated guideline for reporting systematic reviews. *BMJ*, 372, n71. <https://doi.org/10.1136/bmj.n71>
- [76] Parra, D., Valverde, L., Pino, F. J., & Patel, M. K. (2019). A review on the role, cost and value of hydrogen energy systems for deep decarbonisation. *Renewable and Sustainable Energy Reviews*, 101, 279-294. <https://doi.org/10.1016/j.rser.2018.11.010>
- [77] Peng, L., Shah, S. S., Wei, Z., & Li, Y. (2025). Silicon-based photoelectrochemical electrodes for water splitting: Recent progress and prototype development. *Advanced Energy Materials*, 15(4), 2302456.
- [78] Priyanka Saha, S., Rezk, H., & Thomas, J. (2024). Comparative review of hydrogen production costs: Grey, blue, and green hydrogen techno-economic analysis. *International Journal of Hydrogen Energy*, 49, 1234-1251.
- [79] Raman, R., Nair, V. K., Prakash, V., Patwardhan, A., & Nedungadi, P. (2022). Green-hydrogen research: What have we achieved, and where are we going? Bibliometrics analysis. *Energy Reports*, 8, 9242-9260. <https://doi.org/10.1016/j.egyr.2022.07.058>
- [80] Reda, B., Elzamar, A. A., AlFazzani, S., & Ezzat, S. M. (2024). Green hydrogen as a source of renewable energy: A step towards sustainability, an overview. *Environment, Development and Sustainability*, 26, 1-21.
- [81] Rejeb, O., Sarkar, A., Prasad, A. K., & Doudou, S. (2022). Multi-location genetic algorithm-TOPSIS optimization for green hydrogen production: Cost analysis and site selection. *Applied Energy*, 310, 118532.
- [82] Rivera-Tinoco, R., Schoots, K., & van der Zwaan, B. (2008). Learning curves for solid oxide fuel cells. *Energy Policy*, 36(8), 2928-2934.
- [83] Schmidt, O., Gambhir, A., Staffell, I., Hawkes, A., Nelson, J., & Few, S. (2017). Future cost and performance of water electrolysis: An expert elicitation study. *International Journal of Hydrogen Energy*, 42(52), 30470-30492.
- [84] Selvam, C., Mohan Raja, E., & Lal, D. M. (2025). Literature review and case study analysis of electrolyzer performance ranges for PEM and solid oxide technologies. *Renewable and Sustainable Energy Reviews*, 171, 113089.
- [85] Shaban, M. (2024). Experimental study on dual electrolyte configuration for enhanced electrolysis efficiency in alkaline systems. *Journal of Power Sources*, 578, 233245.
- [86] Shudo, R. (2023). Experimental analysis of direct lignin electrolysis cell for enhanced hydrogen production efficiency. *Bioresource Technology*, 378, 128945.
- [87] Stiber, S., Balzer, H., Wierhake, A., Wittich, C., Warkentin, C., Bensmann, B., & Hanke-Rauschenbach, R. (2024). PEM electrolysis stack cost optimization through advanced manufacturing and design strategies. *International Journal of Hydrogen Energy*, 49, 456-471.
- [88] Tang, D., Tan, G. L., Li, G. W., Liang, J. G., Ahmad, S. M., Bahadur, A., Humayun, M., Ullah, H., Khan, A., & Bououdina, M. (2025). Case-based simulation analysis of photovoltaic-electrolysis and photovoltaic-energy storage-electrolysis configurations. *Journal of Cleaner Production*, 384, 135554.
- [89] Tran, N., Powell, C., Marks, L., Cheng, R., & Szyszka, B. (2024). Solar thermal water splitting analysis: Two-step redox cycles and thermochemical efficiency modeling. *Solar Energy*, 248, 123-138.
- [90] Travaglini, S., Peppas, A., Benvenuto, M., Paoletti, S., & Zorpas, A. A. (2025). Modeling analysis of various green hydrogen production configurations: Economic and environmental assessment. *International Journal of Hydrogen Energy*, 50, 567-583.
- [91] Vartiainen, E., Masson, G., Breyer, C., Moser, D., & Román Medina, E. (2022). Impact of weighted average cost of capital, capital expenditure, and other parameters on future utility-scale PV levelised cost of electricity. *Progress in Photovoltaics: Research and Applications*, 28(6), 439-453.

- [92] Yap, J., & McLellan, B. (2023). A historical analysis of hydrogen economy research, development, and expectations, 1972 to 2020. *Environments*, 10(1), 11. <https://doi.org/10.3390/environments10010011>
- [93] Yelanci, A., Dincer, I., & Ozturk, H. K. (2009). A review on solar-hydrogen/fuel cell hybrid energy systems for stationary applications. *Progress in Energy and Combustion Science*, 35(3), 231-244.
- [94] Yue, M., Lambert, H., Pahon, E., Roche, R., Jemei, S., & Hissel, D. (2021). Hydrogen energy systems: A critical review of technologies, applications, trends and challenges. *Renewable and Sustainable Energy Reviews*, 146, 111180. <https://doi.org/10.1016/j.rser.2021.111180>
- [95] Zainal, B. S., Ker, P. J., Mohamed, H., Ong, H. C., Fattah, I. M. R., Rahman, S. M. A., Nghiem, L. D., & Mahlia, T. M. I. (2024). Recent advancement and assessment of green hydrogen production technologies. *Renewable and Sustainable Energy Reviews*, 189, 113941.
- [96] Zhao, X., & Yuan, Z. (2023). Literature review and performance analysis of photovoltaic-electrolysis, photovoltaic-energy storage-electrolysis, and photoelectrochemical systems. *Applied Energy*, 332, 120534.
- [97] Zhou, L., Huang, J., Yan, B., Liu, L., Zhang, S., Wang, C., Xu, Y., Zeng, J., Wang, D., & Sham, T. K. (2022). Solar-to-hydrogen efficiency analysis and electrolyzer efficiency ranges from literature review. *Nature Communications*, 13, 7884.

Analysis of Pressure Losses of Selected Filtration Materials

Romana Dobáková^{1*}; Tomáš Brestovič²; Natália Jasminská³

Department of Energy Engineering, Faculty of Mechanical Engineering, Technical University of Košice, Slovakia

*Corresponding Author

Received: 07 September 2025/ Revised: 14 September 2025/ Accepted: 23 September 2025/ Published: 30-09-2025

Copyright © 2025 International Journal of Engineering Research and Science

This is an Open-Access article distributed under the terms of the Creative Commons Attribution Non-Commercial License (<https://creativecommons.org/licenses/by-nc/4.0>) which permits unrestricted Non-commercial use, distribution, and reproduction in any medium, provided the original work is properly cited.

Abstract— *With the increasing demands on the efficiency of filtration materials, it is essential to pay attention to the study of pressure losses that occur during the flow of air through these materials. This article presents a device design for measuring pressure losses, followed by experimental verification of selected filtration materials. From the individual measurements, permeability and resistance coefficient are evaluated, which are key for determining the filter's pressure parameters and its performance under real operating conditions.*

Keywords— *Pressure Losses, Filtration Materials, Permeability, Resistance Coefficient.*

I. INTRODUCTION

The capture of aerosol particles using solid filters is the most widespread method of air purification, proven to be a simple, universal, and cost-effective way to separate particles. At low dust concentrations, fibrous filters are the most economical solution for effectively removing even very small microscopic particles. This technology is used in various areas, such as respiratory protection, air conditioning, air purification in industrial operations, and more. Although the basic principles of filtration are well studied, it remains a complex process in which discrepancies often arise between theoretical models and experimentally measured results [1].

Pressure loss is one of the main parameters determining the usability of different types of filters, as it affects their energy consumption, the efficiency of medium flow, and the overall requirements for their application in various areas of use.

II. DESIGN OF EXPERIMENTAL DEVICE

Effective filtration is a fundamental element in many technological processes, ranging from industrial applications to healthcare facilities. A key parameter in evaluating filtration materials is pressure loss, which arises due to the resistance the filtration material poses to the flowing medium. Determining this pressure loss is essential for the proper design and optimization of filtration systems.

When designing the experimental apparatus, it was necessary to propose and select components that ensure reliable, repeatable, and practically applicable measurements of the physical properties of filtration materials. The device was designed with an emphasis on accuracy, ease of operation, and the ability to be calibrated—an essential factor for long-term stability and measurement precision.

The basic principle of the device is to measure the pressure before and after the filtration material, based on which the filter's pressure loss is determined. To ensure measurement accuracy, it is necessary to select an appropriate manometer with a suitable range and sensitivity. A fan is used to generate airflow, creating forced air movement through the filter material. A critical aspect of evaluating pressure losses is the ability to regulate the fan's speed, which allows for varying the volumetric airflow through the filtration material and subsequently determining parameters related to the filter's properties.

The acquired pressure loss data must be systematically recorded and stored, which was achieved through the design of a suitable electronic solution and its integration with data acquisition software. The ambient air pressure was measured using an atmospheric pressure sensor, and the airflow velocity at the system's inlet was measured using an anemometer.

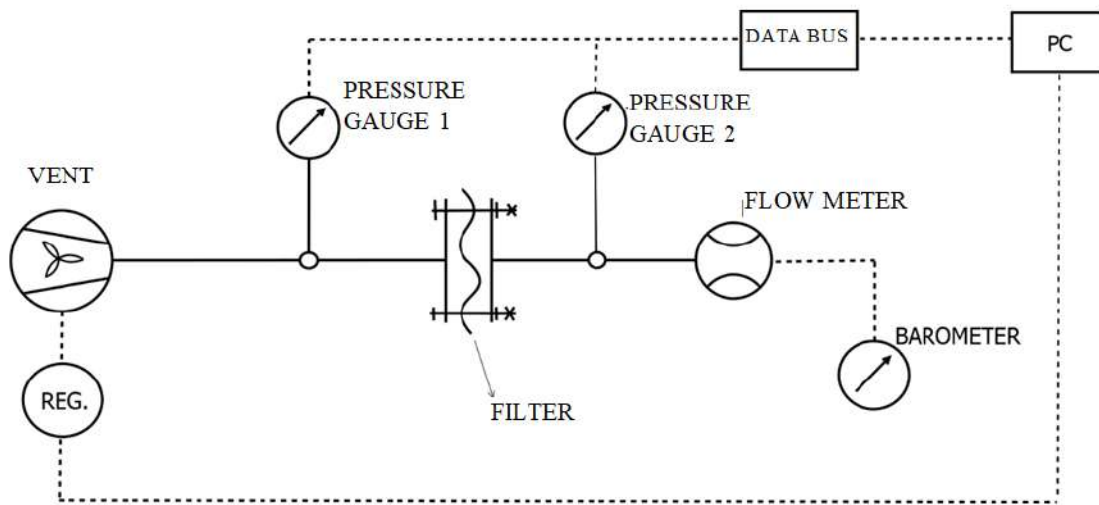


FIGURE 1: Measurement stand diagram

The piping system consists of simple tubes made using additive manufacturing technologies. Individual segments are connected by flanges, which are secured with bolts. This method of assembly ensures a strong connection while also allowing for easy disassembly and reassembly during maintenance or replacement of pipeline components. The connection interfaces are designed to minimize air leakage and ensure maximum system tightness. The tested filter is placed into a filter holder, which ensures its secure and stable positioning during testing. The holder is designed to allow quick and easy filter replacement without the need to disassemble the entire system.

III. DETERMINATION OF PERMEABILITY AND RESISTANCE COEFFICIENT OF FILTER MATERIAL

The pressure change across the filter can be described by a differential equation based on Darcy's law for laminar flow, supplemented by a term accounting for turbulent flow.

$$\frac{dp}{dx} = \frac{\eta}{k_f} \cdot w + \beta \cdot \rho \cdot \frac{w^2}{2} \quad (1)$$

$$\Delta p = \frac{\eta}{k_f} \cdot v \cdot \delta + \beta \cdot \rho \cdot \frac{w^2}{2} \cdot \delta \quad (2)$$

For a filter with an average thickness δ , a substitution can be made:

$$k'_f = \frac{k_f}{\delta}, \quad \beta' = \beta \cdot \delta$$

equation (2) is then:

$$\Delta p = \frac{\eta}{k'_f} \cdot v + \beta' \cdot \rho \cdot \frac{w^2}{2} \quad (3)$$

where η is the dynamic viscosity (Pa·s), k'_f - is the permeability of the filter (m), β' - is the resistance coefficient (1), ρ - density of air (kg·m⁻³), w - speed of sound (m·s⁻¹), Δp - pressure loss (Pa), δ - material thickness (m).

From two measurements of air velocity and pressure loss across the given filter, a system of two equations is formed, from which the permeability and the resistance coefficient of the filtration material can subsequently be calculated.

IV. EXPERIMENTAL MEASUREMENT OF PRESSURE LOSSES OF SELECTED FILTRATION MATERIALS

For the purpose of obtaining data on permeability and resistance coefficient, experimental measurements were conducted on four selected filtration materials: the AJ PRO and Promask PM2 respirators, a Type II surgical mask, and a textile mask.



FIGURE 2: Selected filter materials

From each pair of measured pressure loss values at different air velocities through the filtration material, the permeability k'_f and resistance coefficient β' were calculated from the system of two equations. Subsequently, pressure losses were analytically calculated using equation (3), and their values were graphically represented as a function of the air velocity through the filtration material. To increase the accuracy of the measured data, each measurement was performed three times at different air velocities. All pressure loss measurements of the filters were carried out at an air dynamic viscosity of $1.82 \cdot 10^{-5}$ Pa·s and an air density of $1.167 \text{ kg} \cdot \text{m}^{-3}$. The examined cross-sectional area of the filters was 2.715 mm^2 (bounded by attachment to the measurement stand).

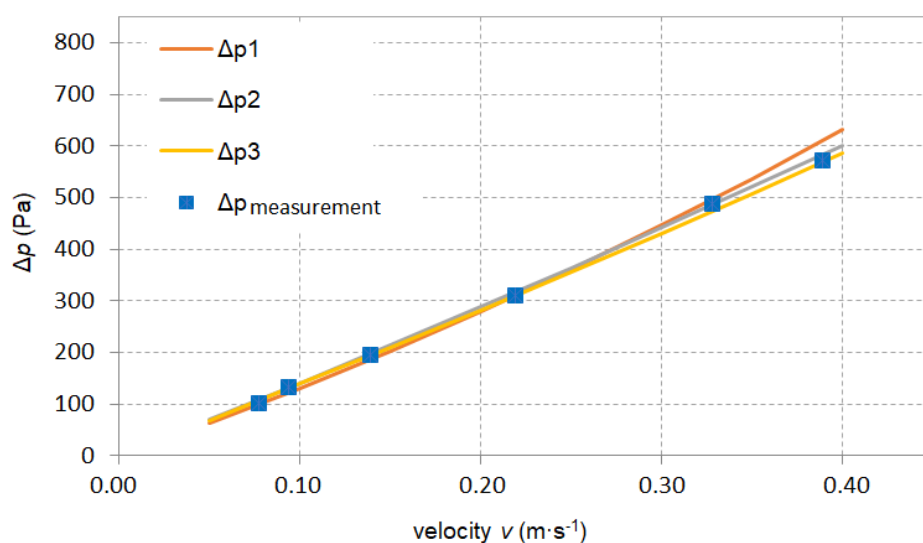


FIGURE 3: The course of pressure losses depending on the air velocity through the respirator's filtration material AJ PRO

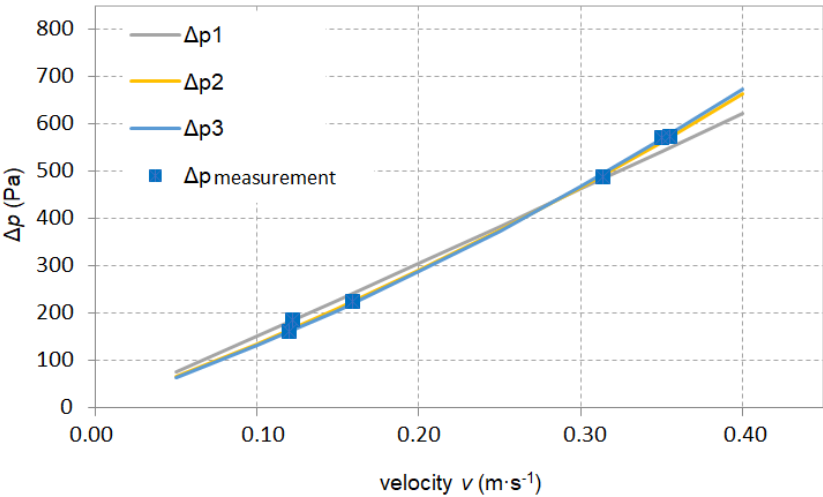


FIGURE 4: The variation of pressure loss depending on the air velocity through the filtration material of the Promask respirator

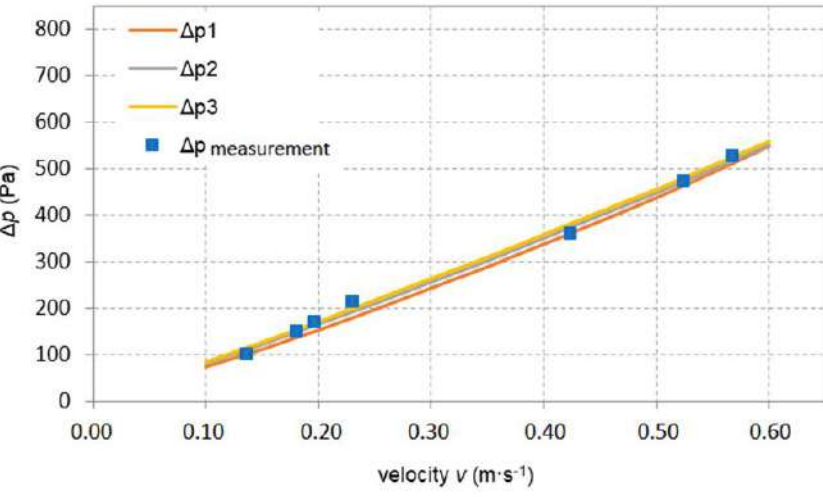


FIGURE 5: The variation of pressure loss depending on the air velocity through the filtration material of the Type II surgical mask

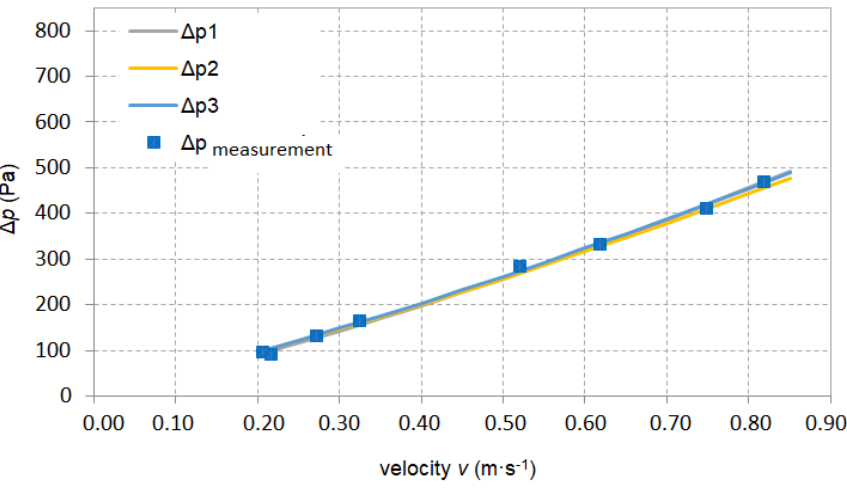


FIGURE 6: The variation of pressure loss depending on the air velocity through the filtration material of the textile mask

Based on the conducted measurements, it can be concluded that the textile mask exhibited the highest permeability, indicating its lowest resistance to airflow. This reflects the simplicity of the materials used and suggests its suitability for environments with coarse, dispersed particles. In contrast, both respirators showed significantly lower permeability, corresponding to their higher filtration efficiency but also resulting in higher pressure losses. The permeability of the surgical mask was between the values of the textile mask and the respirators. The distribution of resistance coefficient values corresponded with the pressure loss values, with the highest recorded for the respirators and the lowest for the textile mask. Among the FFP2-class respirators, no significant differences in permeability were observed; however, the Promask respirator exhibited higher resistance coefficient values, which may be attributed to differences in the material composition and structure of the filtration medium.

TABLE 1
MEASURED VALUES OF PERMEABILITY AND RESISTANCE COEFFICIENT OF SELECTED FILTRATION MATERIALS

Material	Permeability k'_f	Resistance coefficient β'
	(m)	-1
FFP2 respirator AJ PRO	$1.39 \cdot 10^{-8}$	$0.85 \cdot 10^3$
FFP2 respirator Promask	$1.41 \cdot 10^{-8}$	$1.42 \cdot 10^3$
Surgical mask	$2.36 \cdot 10^{-8}$	$0.42 \cdot 10^3$
Textile mask	$4.14 \cdot 10^{-8}$	$0.26 \cdot 10^3$

Based on the analysed dependence of pressure loss on the change in air velocity through the filtration material, it is subsequently possible to determine the minimum filtration area required to achieve the desired operational parameters while maintaining acceptable pressure losses.

The maximum allowable pressure loss for FFP2 respirator filters according to the EN 149 standard is 240 Pa during inhalation and 300 Pa during exhalation. According to the graphs presented below, these correspond to the maximum permissible air velocities w ($\text{m} \cdot \text{s}^{-1}$) (taken as the minimum of the measured values). The total required airflow according to the relevant standard is $95 \text{ l} \cdot \text{min}^{-1}$ during inhalation and $160 \text{ l} \cdot \text{min}^{-1}$ during exhalation. The required cross-sectional area of the respirator filter for inhalation, considering the maximum allowable pressure loss, is determined using the following relationship:

$$S = \frac{Q_v}{w} \quad (\text{m}^2) \quad (4)$$

where S is the required filtration area (m^2), Q_v – required airflow according to the relevant standard ($\text{l} \cdot \text{min}^{-1}$), w – allowable air velocity ($\text{m} \cdot \text{s}^{-1}$).

Using the given formula, we can determine the minimum required filtration area for the AJ PRO AJ-01 FFP2 respirator as follows:

From the graph, we read the average air velocity at a pressure loss level of 240 Pa, which in this case is $0.17 \text{ m} \cdot \text{s}^{-1}$.

Calculation of the respirator filter's cross-sectional area for inhalation:

$$S_{\text{inhalation}} = \frac{Q_{v_{\text{inhalation}}}}{w} = \frac{0.001583}{0.17} = 93.14 \text{ cm}^2$$

From the graph, we read the average air velocity at a pressure loss level of 300 Pa, which in this case is $0.21 \text{ m} \cdot \text{s}^{-1}$.

Calculation of the respirator filter's cross-sectional area for exhalation:

$$S_{\text{exhalation}} = \frac{Q_{v_{\text{exhalation}}}}{w} = \frac{0.00267}{0.21} = 126.98 \text{ cm}^2$$

In a similar way, it is possible to determine the minimum filtration area for respirators subject to the EN 149 standard.

V. CONCLUSION

The results obtained from measurements on the designed device show that respirators achieved the lowest permeability and the highest resistance coefficient, as they are intended for use in environments with high concentrations of aerosol particles, bacteria, and viruses, where it is necessary to ensure the maximum level of filtration and respiratory protection for the user. To meet these conditions, materials with a very fine microstructure are required, which effectively capture even the smallest particles but at the same time increase the airflow resistance during breathing.

In contrast, masks exhibited higher permeability and lower resistance coefficients, indicating their lower ability to filter fine particles. This phenomenon is caused by their simpler fabric structure, which generally has larger pores and fewer layers compared to respirators. As a result, masks offer less resistance to the flowing air, which increases breathing comfort but simultaneously reduces their effectiveness in capturing aerosols and microorganisms. These properties make masks more suitable for use in ordinary, less risky environments where a high level of protection is not required.

The designed and constructed device is intended for testing various filtration materials, with its versatility lying in the possibility of adjusting components used to mount the filtration material—manufactured by 3D printing—as well as the fan that creates the required pressure in the system. Based on the measurement results obtained, it is subsequently possible to design the necessary filtration area that would meet the relevant standards or device requirements where the filtration materials will be applied. The simplicity and versatility of this device make it useful in various application areas as a preliminary step for verifying filter efficiency

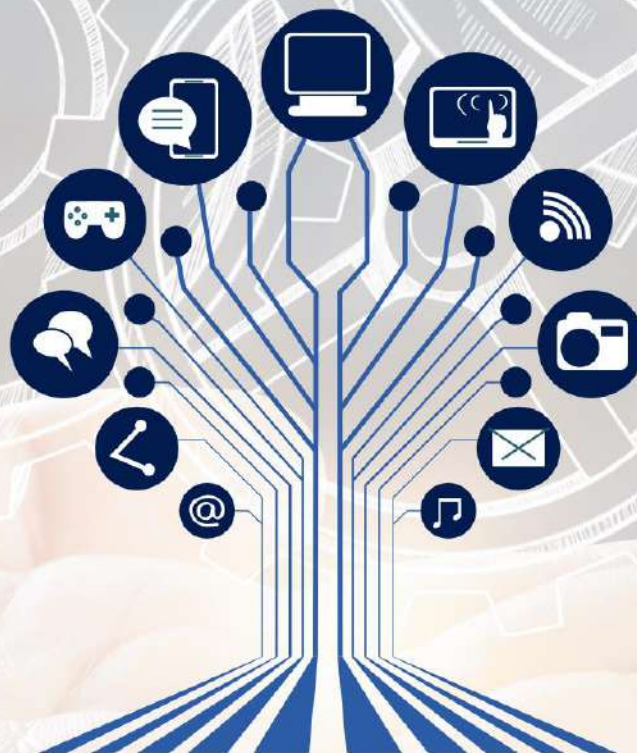
REFERENCES

- [1] Chyský, J., Hemzal, K.: Větrání a klimatizace. 3. vyd. Praha: BOLIT-B Press, 1993.
- [2] STN EN 149+A1. Ochranné prostriedky dýchacích orgánov - Filtračné polmasky na ochranu pred časticami (požiadavky, skúšanie, označovanie).
- [3] Konda, A., Prakash, A., Moss, G. A., Schmoldt, M., Grant, G. D., Guha, S.: *Aerosol Filtration Efficiency of Common Fabrics Used in Respiratory Cloth Masks*. ACS Nano. 2020, 14(5), 6339–6347.
- [4] Costa, U.M.S., Andrade Jr., J.S., Makse, H.A., Stanley, H.E.: *The role of inertia on fluid flow through disordered porous media*. Physica A: Statistical Mechanics and its Applications. 1999, 266, 420–424.
- [5] Hasolli, N., Park, Y.O., Rhee, Y.W.: *Filtration performance evaluation of depth filter media cartridges as function of layer structure and pleat count*. Powder Technology. 2013, 237, 24–31.



IJOER
ENGINEERING JOURNAL

International Journal of Engineering Research and Science



Published by
AD Publications

Contact us



+91-7665235235



www.ijoer.com



info@ijoer.com